Supplement of Atmos. Chem. Phys., 26, 12793–12811, 2026
https://doi.org/10.5194/acp-26-12793-2026-supplement

Atmospheric Chemistry and Physics
Open Access
EGU

Supplement of

Unravelling gas-particle partitioning dynamics in cooking aerosol oxidation through FIGAERO-CIMS analysis

Ruizhe Shen et al.

Correspondence to: Song Guo (songguo@pku.edu.cn)

S1. Basic flow and oxidation characteristics of Go:PAM flow tube

Experiment applies OFR254 mode of Go:PAM flow tube under low NO_x conditions, where OH radical serve as the predominant oxidant. The OFR 254 mode generate OH radical from reaction of $O(^1D)$ radical and water vapor. $O(^1D)$ radicals are generated by photolysis of ozone(Peng and Jimenez, 2020).The reactions are listed in RS1-RS3:

$$O_3 \xrightarrow{h\nu\ 254nm} O(^1D) + O_2 \quad \text{RS1}$$

$$O(^1D) + H_2O \rightarrow 2OH \quad \text{RS2}$$

$$OH + precursors \rightarrow products \quad \text{RS3}$$

We estimate OH exposure in the flow tube using semi-empirical equation recommended by Peng et al(Peng et al., 2016) as shown in the main text. EqS1 represents the equation.

$$\log_{10} OH\ exposure(\# \cdot cm^{-3} \cdot s) = 15.514 + 0.79292 * \log_{10}[H_2O] + 0.023076 * (\log_{10}[H_2O])^2 - 1.0238 * \log_{10}[\Phi_{254}] + 0.060786 * (\log_{10}[\Phi_{254}])^2 - \log_{10}\{exp[-0.42602 - \log_{10}([O_3]/OHR)/0.39479]\} + \log_{10}(t_R/180) \quad \text{Eq. S1}$$

In Equation S1, $[H_2O]$ stand for dimensionless water vapor mixing ratio in the flow tube, converted from relative humidity. Φ_{254} means total UV photon flux at 254nm in the Go:PAM flow tube, determined to be 6.05×10^{15} photons cm^{-2} s^{-1} by photometer measurement and ozone loss in ozone blank experiment estimation under OFR 254 mode. $[O_3]$ is ozone concentration in ppbv monitored by ozone analyzer. t_R is retention time of the OFR, determined to be 55s in current study. OHR stands for total OH reactivity of organic precursors in the flow tube, estimated based on VOCUS-PTR quantification of gas-phase primary organic compounds. For compounds with certain elemental composition detected by VOCUS, we search organic species in the National Cancer Institute (NCI) database to find molecules with same elemental composition, and summarize OH reaction rate constants provided by EPI SUITE™. We choose geometric mean of OH reaction rates provided by EPI SUITE™ as the rate coefficient corresponding to molecules with same elemental composition detected by VOCUS(Sitzmann et al., 2013; Epa., 2012). Validation on applicability and representability of equation S1 to oxidation experiments utilizing the Go:PAM OFR adopted in this study is tested by sulfur dioxide-oxidation calibration experiment. We adopt a simple radical chemistry box model representing OH generation,

transformation and decay in flow tubes. The box model based on the atmospheric chemical mechanism generation system (MechGen) originally developed for SAPRC mechanisms to validate the estimation method(Ono et al., 2014; Carter et al., 2025). Reactions and rate coefficients used in the box model are shown in Table S1. Comparison of OH exposure estimated from measured SO_2 decay, box model and semi-empirical equation Eq.S1 in SO_2 oxidation calibration experiments are characterized in Figure S1. The results indicate that Eq. S1 is suitable for estimating OH exposure in the Go:PAM flow tube and thus representing the OH oxidation strength during the experiment. Aerosol wall loss through the Go:PAM reactor is determined by comparison between primary size distributions, that are recorded by SMPS systems deployed before and after Go:PAM. Wall loss of primary aerosols is shown in Figure S2(Zhang et al., 2020; Yu et al., 2022). It should be noted that oxidation conditions in Go:PAM differ from real atmosphere, can cause OH suppression, altered RO_2 chemistry, enhanced secondary photolysis and fragmentation(Peng and Jimenez, 2020). Thus, uncertainties of Go:PAM usage should be more carefully considered in following studies.

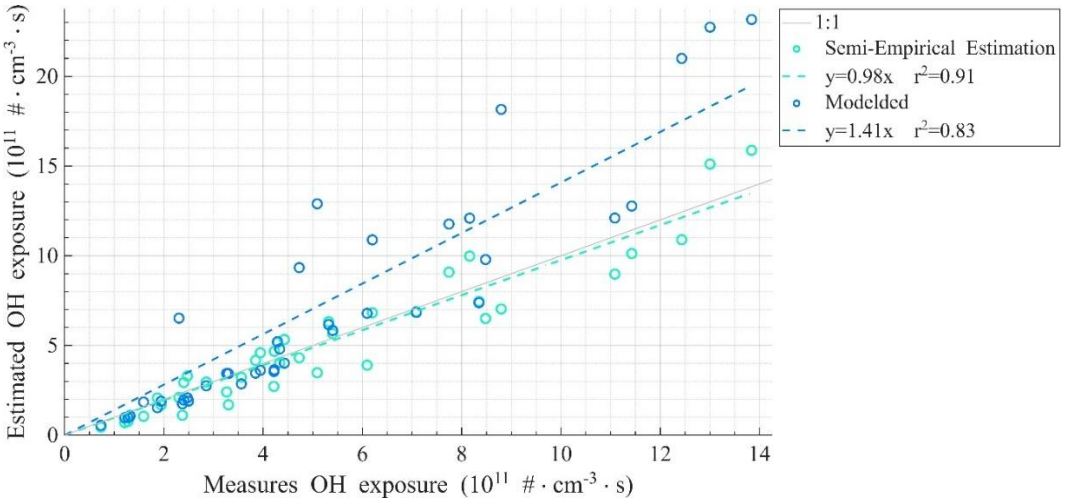

Figure S1 Correlation between OH exposure estimated by SO_2 depletion, chemistry model equation S1 in the Go:PAM reactor used in this experiment

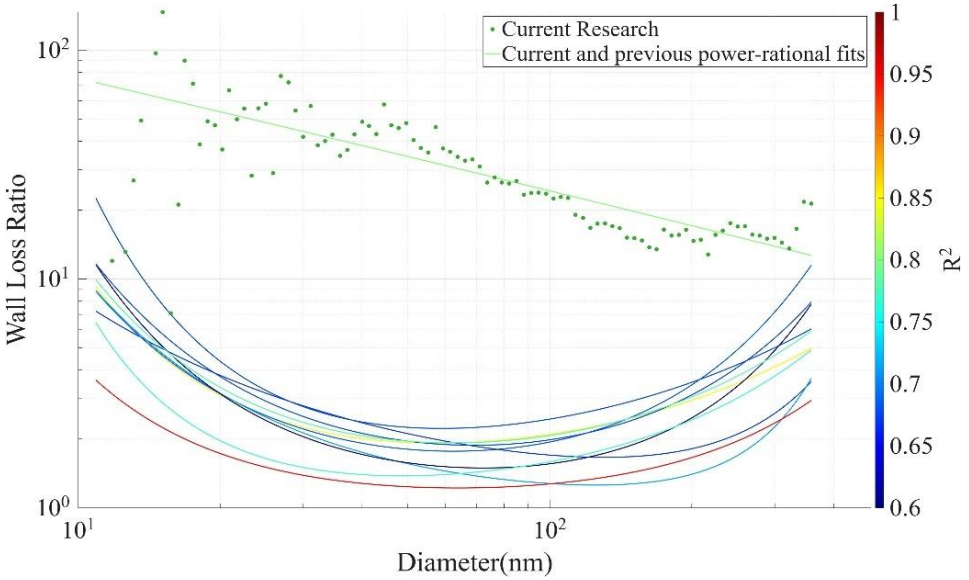

Figure S2 Size dependence of particle wall loss ratio in Go:PAM during experiment

Table S1 Reactions and rate constant used in box model representing OH formation and SO_2 calibration in Go:PAM

Reaction	k(molecule cm^{-3} s^{-1}) **
(1) $O_3 = O(^1D) + O_2(^1\Delta_g)$	$6.15\times10^{-2}(s^{-1})$ *
(2) $O_3 = O(^3P) + O_2$	$6.81\times10^{-3}(s^{-1})$ *
(3) $O(^3P) + O_2 = O_3$	1.39×10^{-14}
(4) $O(^3P) + O_3 = 2O_2$	8.0×10^{-15}
(5) $O(^1D) + N_2 = O(^3P) + N_2$	2.6×10^{-11}
(6) $O(^1D) + O_2 = O(^3P) + 0.15O_2 + 0.05O_2(^1\Delta_g) + 0.8O2(^1\Sigma_g)$	4.0×10^{-12}
(7) $O(^1D) + O_3 = 1.5O_2 + O(^3P)$	2.4×10^{-10}
(8) $O_2(^1\Delta_g) + O_2 = 2O_2$	1.6×10^{-18}
(9) $O_2(^1\Delta_g) + O_3 = 2O_2 + O(^3P)$	3.8×10^{-15}
(10) $O_2(^1\Delta_g) + H_2O = O_2 + H_2O$	5.0×10^{-18}
(11) $O_2(^1\Delta_g) + O_2(^1\Delta_g) = 1.1O_2 + 0.9O_2(^1\Sigma_g)$	2.8×10^{-17}
(12) $O_2(^1\Sigma_g) + N_2 = 0.1O_2 + 0.9O_2(^1\Delta_g) + N_2$	2.1×10^{-15}
(13) $O_2(^1\Sigma_g) + H_2O = 0.1O_2 + 0.9O_2(^1\Delta_g) + N_2$	4.6×10^{-12}
(14) $O_2(^1\Sigma_g) + O_3 = 1.43O_2 + 0.3O_3 + 0.27O_2(^1\Delta_g) + 0.7*O(^3P)$	2.2×10^{-11}
(15) $O(^1D) + H_2O = 2OH$	2.2×10^{-10}
(16) $O(^3P) + OH = H + O_2$	3.5×10^{-11}
(17) $H + O_2 = HO_2$	1.19×10^{-12}
(18) $HO_2 + O(^3P) = OH + O_2$	5.8×10^{-11}
(19) $HO_2 + OH = H_2O + O_2$	1.1×10^{-10}
(20) $H + O_3 = OH + O_2$	2.9×10^{-11}
(21)$H + HO_2 = 1.8OH + 0.07H_2 + 0.07O_2 + 0.03H_2O + 0.03O(^3P)$	8.0×10^{-11}

(22) $H + OH = H_2O$	1.89×10^{-11}
(23) $OH + OH = H_2O_2$	5.2×10^{-12}
(24) $OH + OH = H_2O + O(^3P)$	1.5×10^{-12}
(25) $OH + H_2O_2 = H_2O+HO_2$	1.7×10^{-12}
(26) $OH + O_3 = HO_2 + O_2$	7.3×10^{-14}
(27) $HO_2 + HO_2 = H_2O_2 +O_2$	2.9×10^{-12}
(28) $HO_2 + O_3 = OH + 2O_2$	2.0×10^{-15}
(29) $H_2O_2 + O(^3P) = OH + HO_2$	1.7×10^{-15}
(30) $H_2O_2 = 2OH$	$4.78\times10^{-4}(s^{-1})$ *
(31) $OH + SO_2 = HSO_3$	8.04×10^{-13}
(32) $HSO_3 + O_2 = SO_3 + HO_2$	4.30×10^{-13}
(33) $O(^3P) + SO_2 = SO_3$	3.10×10^{-14}
(34) $SO_3 + H_2O = H_2SO_4$	3.14×10^{-15}
(35) $O(^1D) + H_2 = OH + H$	1.1×10^{-10}

*Estimated from UV spectra data in the Go:PAM

**Rate constant data source(Atkinson et al., 2004)

S2. Vocus-PTR and FIGAERO-I-CIMS sensitivity calibration and volatility quantification

Vocus-PTR data are utilized to determine OH exposure(Yu et al., 2022).For Vocus data quantification, we utilize authentication standard gas mixture to calibrate the response of 25 VOCs in Vocus with different composition and structure. Calibrations were performed every day after the experiments finished. The authentication standard gas includes 7 aromatic hydrocarbons (benzene, toluene, m-xylene, styrene, 1,2,3-trimethylbenzene, 1,3,5-trimethylbenzene, naphthalene), 5 terpenes and terpenoids (isoprene, α-pinene, β-pinene, β-caryophyllene, nopinone), 5 carbonyl compounds (acetaldehyde, acrolein, acetone, methyl vinyl ketone, 3-pentanone, ethyl acetate), 3 alcohols (methanol, 2-propanol, 1-butanol), 2 nitriles (acrylonitrile, acetonitrile), and 2 halocarbons (chlorobenzene, 1,3-dichlorobenzene). Calibration standard-gas concentration levels are 1, 10, 20 50, and 100ppbv. Transfer-function calibrations and fragmentation assignments have been proceeded after every experiments(Yu et al., 2022).

Sensitivity of species without authentication standards is estimated based on molecular composition of species. For detected compounds having same elemental composition with any species in the standard gas, we choose the sensitivity of the compound in the standard as their sensitivity. For species detected with elemental composition other than species in the standard gas, we utilize the Vocus-PTR sensitivity parametrization method developed by Sekimoto et

al.(Sekimoto et al., 2017). Briefly, linear relation between proton transfer rate k and sensitivity has been discovered in Vocus-PTR calibrations(Krechmer et al., 2018; Sekimoto et al., 2017). This linear relation is quantified based on calibration results and account for transmission efficiency. Proton transfer rate k of species without authentication standards are determined by parameterization methods based on molecular polarizability and dipole moment, while polarizability and dipole moment are derived from elemental composition. Detailed processes are shown in Figure S3 and has been thoroughly discussed by Sekimoto et al.(Sekimoto et al., 2017; Jensen et al., 2023). It should be noticed that fragmentation of species without calibration standards are not considered quantitatively, which may lead to measurement uncertainty.

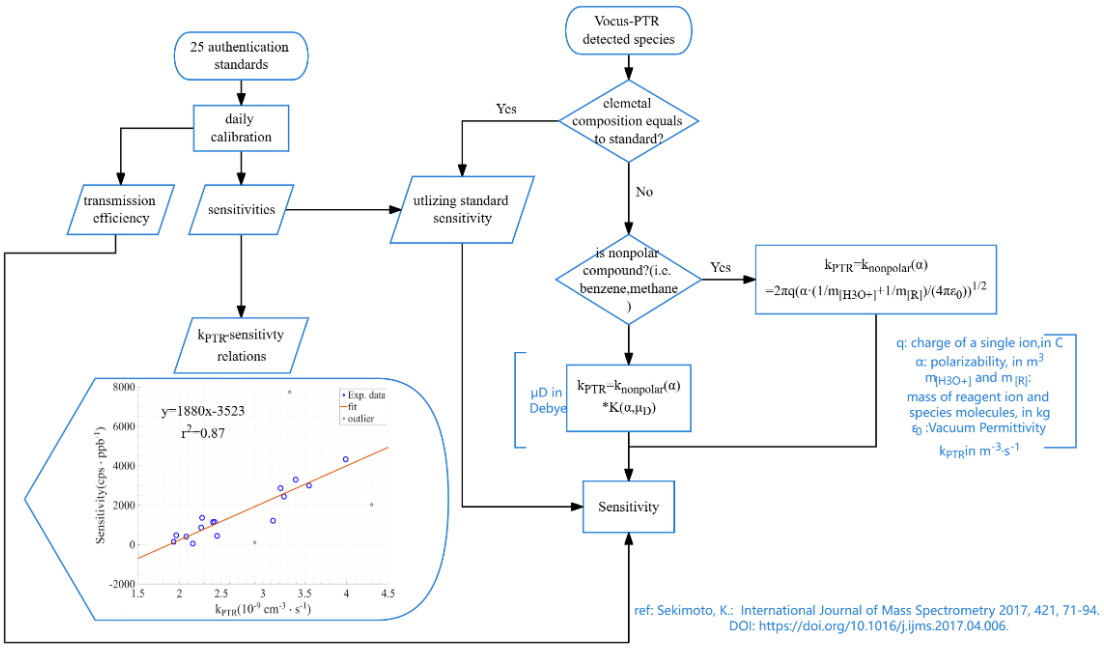

Figure S3 Calibration and sensitivity parameterization procedure of Vocus-PTR detected species in this study

Quantification and volatility determination using FIGAERO-CIMS are completed utilizing calibration methods employed by Ylisirniö(Ylisirniö et al., 2021). Schematic view of calibration process is shown in Fig. S4 a). Sensitivity of certain compound is determined by depositing certain volume of authentication standard solution onto PTFE filter inside FIGAERO inlet utilizing syringe, and process one operation cycle with thermal desorption phase only. We choose acetonitrile as the solvent for better solvation ability of standard compounds and wetting ability on the filter. During sensitivity calibrations, standard solution concentration ~1μg/mL are firstly generated. Then, 3-5 different volume within the volume range 1μL -20μL of standard solution are deposited onto the collection filter, and the thermal desorption cycle are proceeded. Sensitivity of

selected compound in CIMS is determined by Equation S2:

$$\overline{([RI^-]/[I^-])} = S_i(ncps \cdot ppb^{-1}) \times V \times c \times \frac{RT}{pQ_{TD}\Delta t_{TD}} + \overline{([RI^-]/[I^-])}_{blank} \quad \text{Eq. S2}$$

In Equation S2, [RI-]/[I-] stands for average normalized signal of selected compound during the thermal desorption process whose normalization based on reagent ion (iodide ion) signal, $([RI\text{-}]/[I\text{-}])_{blank}$ for normalized signal during blank samples, V for total volume of standard solution deposited in μL, c for standard solution concentration in μg/mL, T for room temperature in Kelvin, p for atmospheric pressure in Pa, Q_{TD} for carrier gas flow rate during thermal desorption in m^3/min, Δt_{TD} for thermal desorption duration in minutes. In calibration process of this study, Q_{TD} is 0.002 m^3/min, and Δt_{TD} is 50min, longer than 45min in experiment setup to ensure desorption completeness of authentication standards. Sensitivities are given by linear regression between normalized signal [RI-]/[I-] and solution deposition volume V. For volatile compounds such as formic acid and acetic acid, calibration is completed by generating standard gas from permeation tube, then process linear fit between normalized ion counts detected by I-CIMS and standard gas concentration.

For compounds without corresponding authentication standard and thus lack direct sensitivity calibration, compositional sensitivity parameterizations are adopted based on 2-D VBS proxy. Briefly, we put compounds detected by CIMS into 2-D VBS space using parameterization recommended by Li et al., shown in Section S3(Li et al., 2016). We proceed k-means clustering algorithm built in MATLAB® on compounds in the 2-D VBS space, divide these compounds into several compound groups as shown in Fig. S5(Arthur and Vassilvitskii, 2007). Then, standard compounds with known sensitivity are distributed into 2-D VBS space, to find out each group's corresponding standard compound adapting KNN classification model from clustering results(Albanie, 2019). Finally, we set the sensitivity of compounds having molecular formula different from standards to geometry mean sensitivity of standard compounds in the same group. These parametrization results could help improve characterization and quantification of species detected by CIMS. Iodide adduct ionization is selective toward polar and oxygenated compounds and may under-represent weakly oxygenated or nonpolar species. The reported molecular-composition and 2-D VBS distributions, and resulting sensitivity estimation methods adopted here therefore characterize the detectable iodide-CIMS ion ensemble, rather than complete representation of cooking emissions(Iyer et al., 2016; Lopez-Hilfiker et al., 2016). Trace nitrate-

and sulfur-containing species are not used for mechanistic source interpretation because the corn-oil-only experiment included no sulfur-rich food ingredients(Zhang et al., 2020; Song et al., 2022; Zhu et al., 2021). The low-abundance signals may reflect background, contamination, or molecular-formula assignment uncertainty.

Once sensitivities are determined, gas-phase and aerosol phase concentration of measured species can be solved utilizing determined sensitivities shown in Equations. Background has been assigned as Eqs.S3-4. In Eqs.S3-4, the background term $\overline{([RI^-]/[I^-])}_{blank}$ is determined from average intensity of the last 40 second during thermal desorption phase in FIGAERO measurement cycle(Buchholz et al., 2020). p_{amb} and T_{amb} are ambient temperature on filter in Pa and K, MR_i are molecular mass of species i in g/mol, Q_{TD} and Q_{samp} are flow rate of thermal desorption and particle collection in L/min, Δt_{TD} and Δt_{samp} are duration of thermal desorption and particle collection. Excluding data in first 50 seconds corresponding to instrument-switching interval and subtracting the final-40-s background would reduce switching and baseline artifacts. However, these steps do not independently demonstrate complete desorption of the experimental aerosol loadings. Possible incomplete desorption and carryover are therefore retained as uncertainties when interpreting FIGAERO-derived volatility and PMF factors(Liu et al., 2025b).

$$c_{g,i}(\mu g \cdot m^{-3}) = \frac{([RI^-]/[I^-])_{g,measured} - \overline{([RI^-]/[I^-])}_{blank}}{S_i(ncps \cdot ppb^{-1})} \cdot \frac{p_{amb} MR_i}{RT_{amb}} \cdot 10^3 \quad \text{Eq. S3}$$

$$c_{p,i}(\mu g \cdot m^{-3}) = \frac{\overline{([RI^-]/[I^-])}_{g,measured} - \overline{([RI^-]/[I^-])}_{blank}}{S_i(ncps \cdot ppb^{-1})} \cdot \frac{p_{amb} MR_i}{RT_{amb}} \cdot \frac{Q_{TD}\Delta t_{TD}}{Q_{samp}\Delta t_{samp}} \cdot 10^3 \quad \text{Eq. S4}$$

Volatility determination by FIGAERO is based on log-linear correlation between effective saturation vapor pressure and peak temperature of thermograms(Lopez-Hilfiker et al., 2014; Ylisirniö et al., 2025; Zhang et al., 2026). Volatility calibrations is proceeded choosing polyethylene glycol (PEGs) as standard compound. Calibrations are proceeded following experiment setup in Fig. S4 (b). Standard solution of PEGs is generated by dissolve PEG standard in acetonitrile, then atomized and deposited onto the filter. For other standard solution, we used same method as sensitivity calibration to achieve relation between desorption peak temperature. The empirical log-linear relation between peak temperature T_{max} and saturation vapor pressure p_0 at room temperature derived from PEG calibration standards are shown in Equation S5. Comparison to vapor pressure of atmospheric relevant species standard measured by FIGAERO are shown in Fig. S7.

$$\log_{10} p_{0,298\mathrm{K}}\,(\mathrm{Pa}) = 21.9 - 0.072\mathrm{T}_{max}(\mathrm{K})\; R^2 = 0.94 \qquad \text{Eq. S5}$$

Measured T_{max} of species detected in aerosols by FIGAERO would link to effective saturation vapor pressure p^* rather than pure-component vapor pressure(Sun et al., 2025; Wang et al., 2025; Tikkanen et al., 2020) ,thus will be used in comparison to effective saturation vapor pressures estimated by other methods. T_{max} measured by FIGAERO-CIMS are obtained from local-maxima refinement methods, excluding unreasonable peaks based on measurement uncertainties based on data pre-treat methods in Section S4 (Prager et al., 2020; Cai et al., 2026).

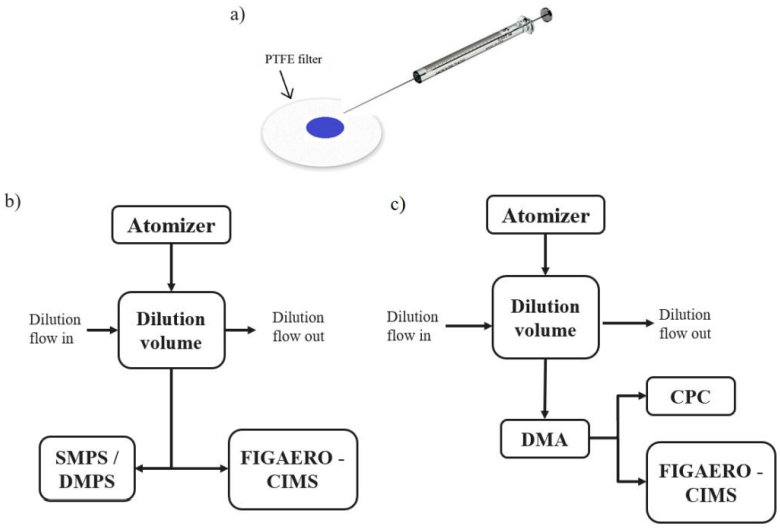

Figure S4 FIGAERO-CIMS volatility and sensitivity calibration method introduced by Ylisirniö, A., et al. (2021) that is used in this article. a) Illustration of the syringe deposition method. b) & c) Illustration of the polydisperse & monodisperse deposition method

Table S2 Sensitivity of calibrates used in CIMS sensitivity calibration and 1σ confidence interval

Species	Molecular composition	Sensitivity (ncps ppb^{-1}) **
PEG-7	$C_{14}H_{30}O_8$	$9.3^{11.2}_{9.0} \times 10^{-2}$
PEG-8	$C_{16}H_{34}O_9$	$10.8^{18.4}_{4.43} \times 10^{-3}$
Malonic acid	$C_3H_4O_4$	Decomposition
Succinic acid	$C_4H_6O_4$	$7.6^{9.5}_{5.8} \times 10^{-3}$
Glutaric acid	$C_5H_8O_4$	$7.3^{10.3}_{4.8} \times 10^{-3}$
Adipic acid	$C_6H_{10}O_4$	$8.2^{11.6}_{5.3} \times 10^{-3}$
Pimelic acid	$C_7H_{12}O_4$	$8.7^{11.5}_{6.2} \times 10^{-3}$
Suberic acid	$C_8H_{14}O_4$	$1.7^{1.9}_{1.5} \times 10^{-2}$
Azelaic acid	$C_9H_{16}O_4$	$7.7^{11.1}_{4.8} \times 10^{-3}$
Sebacic acid	$C_{10}H_{18}O_4$	$7.4^{9.4}_{5.5} \times 10^{-3}$
Dodecanedioic acid	$C_{12}H_{22}O_4$	$3.6^{5.1}_{2.3} \times 10^{-3}$
D-Camphoric acid	$C_{10}H_{16}O_4$	$7.8^{8.5}_{0.84} \times 10^{-3}$
Pinonic acid	$C_{10}H_{16}O_3$	$1.1^{1.7}_{0.66} \times 10^{-2}$
Citric acid	$C_6H_8O_7$	not detected

1,2,4-Tricarboxylic acid	$C_7H_{10}O_6$	not detected
1,3,5-Pentanetricarboxylic acid	$C_8H_{12}O_6$	not detected
2-Hydroxy-1-cyclohexanone	$C_6H_{10}O_2$	not detected
Hydroxyacetone	$C_3H_6O_2$	not detected
DL-Lactic acid	$C_3H_6O_3$	$4.6^{7.6}_{2.3} \times 10^{-2}$
DL-Glyceric acid	$C_3H_6O_4$	$6.3^{32}_{0.0} \times 10^{-4}$
Erythritol	$C_4H_{10}O_4$	$1.2^{1.5}_{1.0} \times 10^{-2}$
2-D-Deoxyribose	$C_5H_{10}O_4$	$1.5^{1.9}_{1.1} \times 10^{-2}$
Xylitol	$C_5H_{12}O_5$	$1.1^{1.3}_{0.96} \times 10^{-2}$
Levoglucosan	$C_6H_{10}O_5$	$3.8^{5.2}_{2.5} \times 10^{-2}$
Isosorbide mononitrate	$C_6H_9NO_6$	$3.5^{5.6}_{1.7} \times 10^{-2}$
2-Nitrophenol	$C_6H_5NO_3$	$1.2^{2.6}_{0} \times 10^{-4}$
4-Nitrophenol	$C_6H_5NO_3$	$1.6^{1.9}_{1.4} \times 10^{-1}$
4-Nitrocatechol	$C_6H_5NO_4$	$7.7^{9.2}_{6.5} \times 10^{-3}$
Benzoic acid	$C_7H_6O_2$	not detected
Salicylic acid	$C_7H_6O_3$	$1.9^{2.6}_{1.3} \times 10^{-3}$
Formic acid*	CH_2O_2	$7.5^{17.0}_{4.4} \times 10^{-3}$
Acetic acid*	$C_2H_4O_2$	$4.4^{17.0}_{2.4} \times 10^{-4}$

* Standard gas calibration generated by standard penetration tube

** Main text stands for sensitivity, superscript and subscripts stands for upper and lower bound of 1σ confidence interval

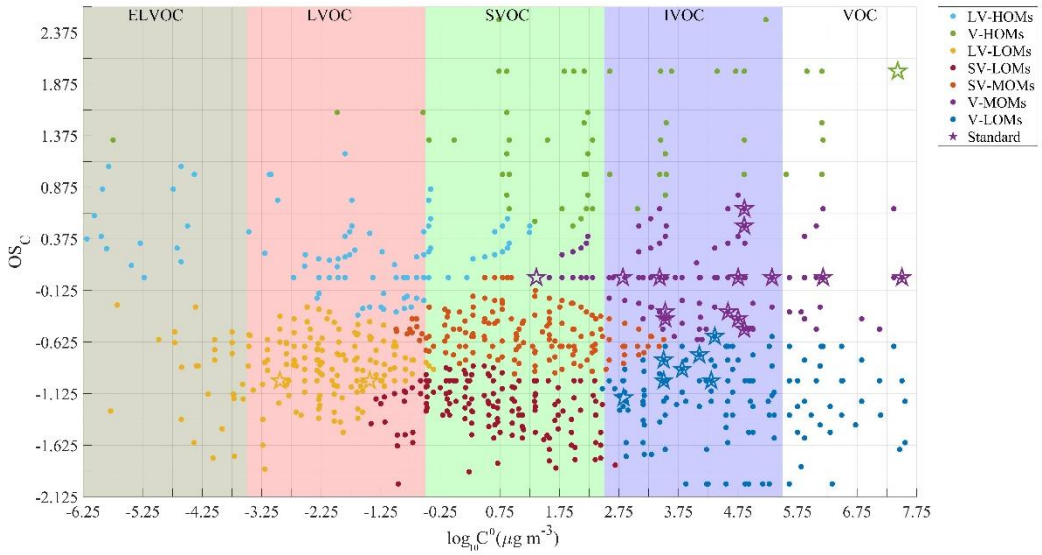

Figure S5 Distribution of species detected in cooking experiment in 2-D-VBS space by I-CIMS (colored dots) and standard compound with known sensitivity(stars). Color of makers shows the category of I-CIMS detected ions classified by k-means algorithms

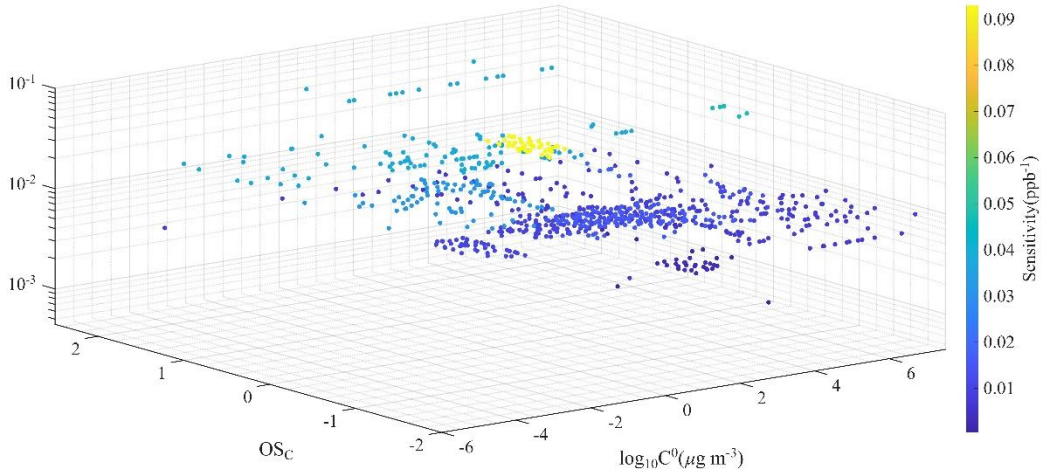

Figure S6 Distribution of species' sensitivity in 2-D-VBS space detected in cooking experiment detected by I-CIMS

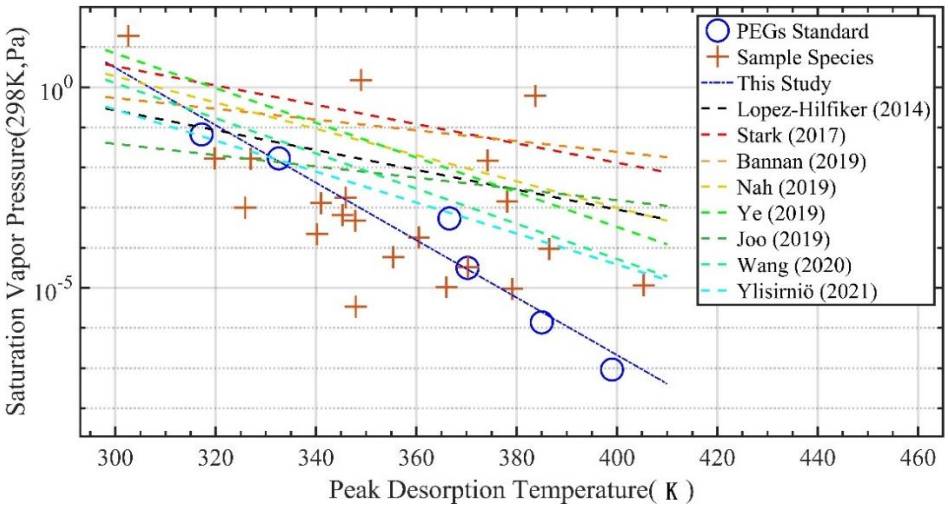

Figure S7 Correlation between FIGAERO thermal desorption peak temperature and satuartion vapor pressure of PEGs and atmospheric-relevant species in previous and current studies(Lopez-Hilfiker et al., 2014; Stark et al., 2017; Bannan et al., 2019; Nah et al., 2019; Joo et al., 2019; Ye et al., 2019; Wang et al., 2020; Ylisirniö et al., 2021)

S3. 2-D VBS spacing scheme for composition and volatility representation

2-D VBS framework is firstly developed by Donahue in 2011 based on VBS approach(Donahue et al., 2011; Donahue et al., 2006; Donahue et al., 2012). 2-D-VBS spacing methods combined composition and volatility distribution screening of gas-phase and aerosol-phase organic compounds, thus giving a more comprehensive representation on detailed derived from molecular compositions detected by high-resolution mass spectrometry such as ToF-CIMS measurements in this study. 2-D-VBS Parameterization used in this article is recommended by Li et al., 2016, as shown in Equation S6(Li et al., 2016):

$$\log_{10} C_0 = (n_C^0 - n_C)b_C - n_O b_O - 2\frac{n_C n_O}{n_C + n_O} b_{CO} - n_N b_N - n_S b_S \qquad \text{Eq. S6}$$

In Eq. S6, empirical saturation vapor concentration C_0 is determined by elemental composition and semi-empirical parameters. n_C, n_O, n_N, n_S are number of most abundant elements atmospheric in

organic aerosols, n_C^0 stand for reference carbon number, b_C means influence of molecular size on volatility, b_O, b_N, b_S shows effect of functional group containing O, N, and S atom, b_{CO} means influence of polar- nonpolar interaction on volatility. Moreover, effective saturation concentration C^* within each 2-D-VBS spaces can be derived from 2-D-VBS parameterizations, based on thermodynamic assumptions that activity coefficient γ_i are related the nonlinear term b_{CO} which represents non-ideality of aerosol bulk, as shown in Equation S37(Donahue et al., 2011).

$$\log_{10}\gamma_{i,300K} = -2b_{CO}(n_M)(f_C^i - f_C^{bulk}) \quad \text{Eq. S7}$$

In Eq. S7, $n_M = n_C+n_O+n_N+n_S$ means sum of C, O, N, S number in compound i that influence compound volatility in 2-D-VBS parameterization scheme, $f_C = n_C/n_M$ means carbon fraction in compound i and bulk aerosol. Parameters used for compounds with different molecular composition categories given by Li et al. are shown in Table S3. Temperature dependency of saturation vapor concentrations can be derived from Clapeyron-Clausius equation as shown in Equation S8, while activity coefficients showing log-reverse-proportional relations toward temperature, shown in Equation S9, thus can be derived from activity at 300K in Equation S10. The vaporization enthalpy is estimated from empirical parametrization recommended by Epstein et al.,2010(Epstein et al., 2010).

$$C_{0,T} = C_{0,300K} \cdot \frac{300K}{T} \exp\left(\frac{\Delta H}{R}\left(\frac{1}{300K} - \frac{1}{T}\right)\right) \quad \text{Eq. S8}$$

$$\log_{10}\gamma_{i,T} = -\delta_{non-ideal}/T \quad \text{Eq. S9}$$

$$\log_{10}\gamma_{i,T} = \log_{10}\gamma_{i,300K} * \frac{300K}{T} \quad \text{Eq. S10}$$

Table S3 Elemental composition class and corresponding 2-D-VBS parameterization in Eq. S6

Elemental Composition Class	n_C^0	b_C	b_O	b_{CO}	b_N	b_S
CH	23.8	0.4861	--	--	--	--
CHO	22.66	0.4481	1.656	−0.7790	--	--
CHN	24.59	0.4066	--	-	0.9619	--
CHON	24.13	0.3667	0.7732	−0.07790	1.114	--
CHOS	24.06	0.3637	1.327	−0.3988	0	0.7579

CHONS	28.5	0.3848	1.011	0.2921	1.053	1.316

S4. Matrix factorization analysis, qualification and diagnostics

For complex mass spectrometry data, non-targeted analysis is introduced to achieve characteristics quantities of detected species without reliable direct prior compound and structure information. Matrix Factorization approaches has been introduced as crucial methods in non-targeted analysis. Briefly, Matrix Factorization is a dimension reduction approach that approximately divide a target m×n data matrix **X** containing hundreds to thousands of variables(n) and change through thousands of time points(m) into p(unknown) different constant sources that varies with time, as shown in Equation S11. The source composition profile are shown in a n×p matrix **F**, while the time series of the source are in the m×p matrix **G**. Factorization target is to cover the difference between data matrix **X** and fitted matrix **R**, minimizing the error matrix **E** with lesser and more interpretable factors.

$$\mathbf{X} = \mathbf{GF} + \mathbf{E} = \mathbf{R} + \mathbf{E} \qquad \text{Eq. S11}$$

For a better factorization result, we compared two widely used factorization approaches for high-resolution mass spectrometry factor analysis processes: Multilinear Engine-2 Positive Matrix Factorization (ME-2 PMF) and Non-Negative Matrix Factorization (NNMF)(Paatero, 1999; Xu et al., 2024; Berry et al., 2007). ME-2 PMF introduce uncertainties of detected variables based on measurement uncertainties as reference, while NNMF minimize error matrix E without additional reference information(Xu et al., 2024). ME-2 PMF is proceeded by utilizing Igor Pro® program SoFi® developed by Canonaco et al. (Canonaco et al., 2013). NNMF is proceeded by built-in algorithm in MATLAB® (Berry et al., 2007). To achieve better deconvolution result and avoid possible background signal interference or physical unreasonable factorization results, we proceed three different data pre-treatment methods on input matrixes. Before data pre-treat methods are adopted, first 50s in aerosol phase measurements are excluded to avoid potential interference caused by switching detection mode in FIGAERO measurements(Buchholz et al., 2020). Basic factorization method input full time series data developed by Buchholz et al. without further selection and pre-treatment; other methods include normalize time series data to maximum for trend analysis, and particle-phase only data for aerosol volatility and composition analysis(Buchholz et al., 2020;

Tikkanen et al., 2020). Goodness of PMF and NNMF results are evaluated by global and local evaluation parameters. Global evaluation parameters include Q/Q_{exp}, root mean square error (RMSE), explained absolute variance $Ratio_{var}$, focusing on performance on the whole data set. Local parameters include time series of summed absolute relative residual and unexplained variation (UEV) among all ions(Canonaco et al., 2013; Buchholz et al., 2020). These parameters are defined in Eqs.12-17:

$$Q = \sum_{j=1}^{m}\sum_{i=1}^{n}\left(\frac{E_{ij}}{\sigma_{ij}}\right)^2 \qquad Q_{exp} = n \times m - p \times (p+m) \quad \text{Eq. S12}$$

$$\mathrm{RMSE} = \sqrt{\frac{\sum_{j=1}^{m}\sum_{i=1}^{n}(E_{ij})^2}{n \times m}} \quad \text{Eq. S13}$$

$$Ratio_{var} = \frac{\sum_{ij}|R_{ij} - \overline{X_i}|}{\sum_{ij}|R_{ij} - \overline{X_i}|} \quad \text{Eq. S14}$$

$$\text{Sum relative residual}_i = \frac{\sum_j R_{ij} - X_{ij}}{\sum_j |X_{ij}|} \quad \text{Eq. S15}$$

$$\text{absolute relative residual}_i = \frac{\sum_j |R_{ij} - X_{ij}|}{\sum_j |X_{ij}|} \quad \text{Eq. S16}$$

$$\mathrm{UEV}_i = \frac{\sum_j |e_{ij}/\sigma_{ij}|}{\sum_j |X_{ij}/\sigma_{ij}|} \quad \text{Eq. S17}$$

Reasonable results require UEV lower than 25% and Q/Q_{exp} reduced to near 1. To classify best factor number, we first plot the relation between factor number and global goodness parameters including Q/Q_{exp}, RMSE and $Ratio_{var}$, choose the "turning points" where goodness indicators reach basic qualification mentioned above and decrease significantly slower after the point than before, indicating the most efficient factor number. Then, we examine changes in time series of local goodness parameters while factor number just across "turning points", to investigate if adding factor number at the turning point leading to significant development on goodness of factorization results. Next, we look at factor thermograms, and finally choose reasonable and interpretable factorization results. Global and local parameters are also used for determining effect of pre-treating method on goodness of PMF and NNMF, to choose suitable factorization method and data pre-treat methods for CIMS data processes. Spectra contrast angle θ are used to assign the similarity of factors, treating spectra of each factor as vectors in linear space make up by species concentration(Pun et al., 2002; Buchholz et al., 2020). Determination of contrast angle are shown

in Equation S18:

$$cos\theta = \frac{\sum_i a_i b_i}{\sqrt{\sum_i a_i^2 \sum_i b_i^2}} \quad \text{Eq. S18}$$

In Equation S18, a_i and b_i stands for spectra intensity of different factors in PMF results. Within a single PMF solution, pairwise angles above 30 °indicate acceptably distinct factor profiles. For matched factors from alternative input matrices corresponding to various data pre-treat methods, a contrast angle below 30 °was treated as crucial indicator on factor similarity. A reasonable PMF result should be consist of factors with contrast angle θ>30 °between every two factors(Buchholz et al., 2020; Bougiatioti et al., 2014).

Figures S8-S10 show changes of the global goodness parameters of ME-2 PMF and MATLAB® NNMF with adding factors. MATLAB® NNMF exhibits better goodness performance on global goodness parameters without considering measurement uncertainty such as lower RMSE and higher $Ratio_{Var}$, especially at factor numbers below 10, while ME-2 PMF shows significant better performance considering measurement uncertainty using Q/Q_{exp}. Figures S11-S13 depicted time series of local goodness parameters such as absolute relative residual. We concluded from Figs. S11-13, that ME-2 PMF shows better performance than MATLAB® NNMF, considering interpreting evolution of composition in oxidation of cooking emission. Only when data pre-treat method are trend analysis methods that normalize speculated time series of detected ions to maximum value, ME-2 PMF and MATLAB® NNMF have comparable performance. Among data pre-treat processes, while utilizing ME-2 PMF as the factorization algorithm, as Figures S17-S19 show, full time-series data shows slightly better performance than particle-phase only data and obvious advantage over time series normalized to maximum point of each detected compound. On the contrary, MATLAB® NNMF method favors data process adopting normalized full time series than particle-phase only and full time series, especially at duration corresponding to measurement of primary cooking emissions, shown in Figures S14-S16.

In conclusion, we would prefer choosing ME-2 PMF as factorization algorithm, select full time series data as main data pre-treat method for PMF in this article, while treat results of particle-phase only data to volatility and partitioning results as reference. To strengthen the confidence in utilizing full time series data as input of ME-2 PMF, we compared composition characteristics of results from different data selection methods with best factor number shown in Table S4. We

estimate the similarity between data from each pre-treat methods by calculating contrast angle between intensity distributions of factors decomposed from input data. The results are shown in Figures S20-S21. Figure S20 shows that composition characteristic extracted from normalized time series has similar characteristics to full time-series data, with contrast angle of nearest factors between these two methods are 30~40 °. Figure S21 indicate that factors extracted from particle phase only data are corresponding to factors extracted from full time-series data, where contrast angle of nearest factors between these two methods are less than 10 °. A gas-phase-only solution was not included because it excludes the particle thermograms required to classify and evaluate the particle-dominated SV/LV factors that are central to the volatility and partitioning analysis. Comparison result indicate the best applicability of utilizing full time-series data as ME-2 input, thus strengthen our confidence on full time-series methods. Based on chosen ME-2 PMF methods and basic data pre-treat methods, we would select the result with 13 factors as the most interpretable PMF results. The reason is, adding factor into PMF will not lead to significant improvements on global goodness and local goodness on both time series and compound axes, shown in Figure S8, S20 and Table S4. Figure S22 shows contrast angle θ between factors of ME-2 PMF best results. The contrast angles are between every two factors are larger than 30 ° (minimum 35 °), showing acceptable low co-linearity resulting in reasonable results of ME-2 PMF.

The factors obtained from PMF are classified with oxidative state and volatility. First, the 13th factor named Background is considered contaminant factor because of its unreasonable Thermogram characteristic. The contamination factor consists of 3 separated peaks at totally separate desorption temperatures, implying that it may consist of three parts related to different interference. Low-desorption-temperature portion may contain interference from FIGAERO inlet model shifting that may mix gas-phase components with aerosol-phase, which can be observed at the first couple of seconds of particle phase data. Medium- and higher-desorption-temperature portions may originate from semi-volatile and low-volatile residuals. 12 interpretable factors are classified as 3 categories, considering its volatility represented by peak temperatures of factor thermograms and FIGAERO-CIMS measured gas-particle partitioning coefficient K_p, shown in Figure S23. Factors mainly or even almost present in gas phase are named volatile factors “V-x”. Factors abundant in both gas phase and aerosol phase factors are called semi-volatile factors “SV-x”. Mostly particle phase factors are classified low-volatile factors “LV-x”. Factors among each

volatility categories are further distinguished and named by oxidative state, molecular composition and possible origin. The evolution of intensity with enhancement of OH exposure is shown in Figures S24-26. Based on intensity evolution shown in Figures S4.17-4.19, factors with sub-name "Pri" including V-Pri and SV-Pri are related to components from primary cooking emissions (e.g. long-chain fatty acids, glycerol, formic acid, acetic acid), with highest abundance in primary emissions and lower abundance at higher OH exposure. Medium-oxidative-state factors, namely V/SV/LV-OxiGen^{1st}-X, are corresponding to intermediate oxidative states, consist of first-generation oxidation products of long-chain fatty acid(e.g. $C_{>5}$monocarboxylic acids, $C_{>3}$ carbonyl acids), reach their peak intensity at medium OH exposure; high oxidative state compounds, namely V/SV/LV-MultiGen-X represent highly oxidated products that relate to multi-generation oxidation(e.g. dicarboxylic acids, peroxides, auto-oxidation products, functionalized long-chain fatty acids), enhance with OH exposure increase. For example, factor V-OxiGen^{1st}-Gly are glycerol-related-compounds-rich factors, whose most abundant compounds have similar structure with glycerol or originate from intermediate oxidation products of glycerol, including hydroperoxyl-acetic acid, malonic acid, pyruvic acid and acetic acid; factor SV-Oxigen^{1st} includes first-generation oxidation products such as C_{3-6} dicarboxylic acids and hydroxy- or carbonyl-carboxylic acids, while abundance of peroxides are relative insignificant; factor LV-Multigen-HMW includes multi-generation oxidation products obtaining long-chain fatty acid structure and there thermal desorption products, having Thermogram T_{max} at ~130℃. Detailed factor molecular composition is shown in Tables S7-19 at Section S6. Detailed discussion about factor composition and origination has been shown in Section 3.3 in the main text.

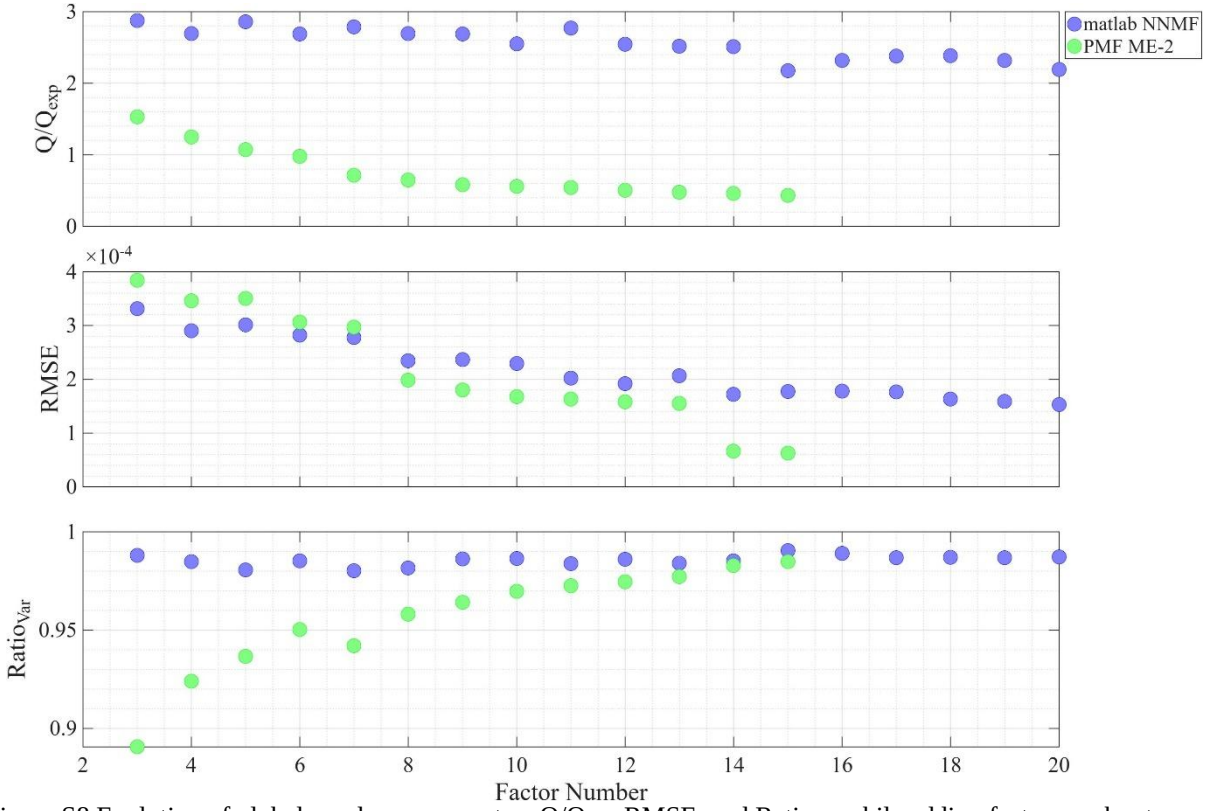

Figure S8 Evolution of global goodness parameters Q/Q_{exp}, RMSE, and $Ratio_{Var}$ while adding factor number to ME-2 PMF & MATLAB® NNMF results using full FIGAERO-CIMS data time series as factorization input.

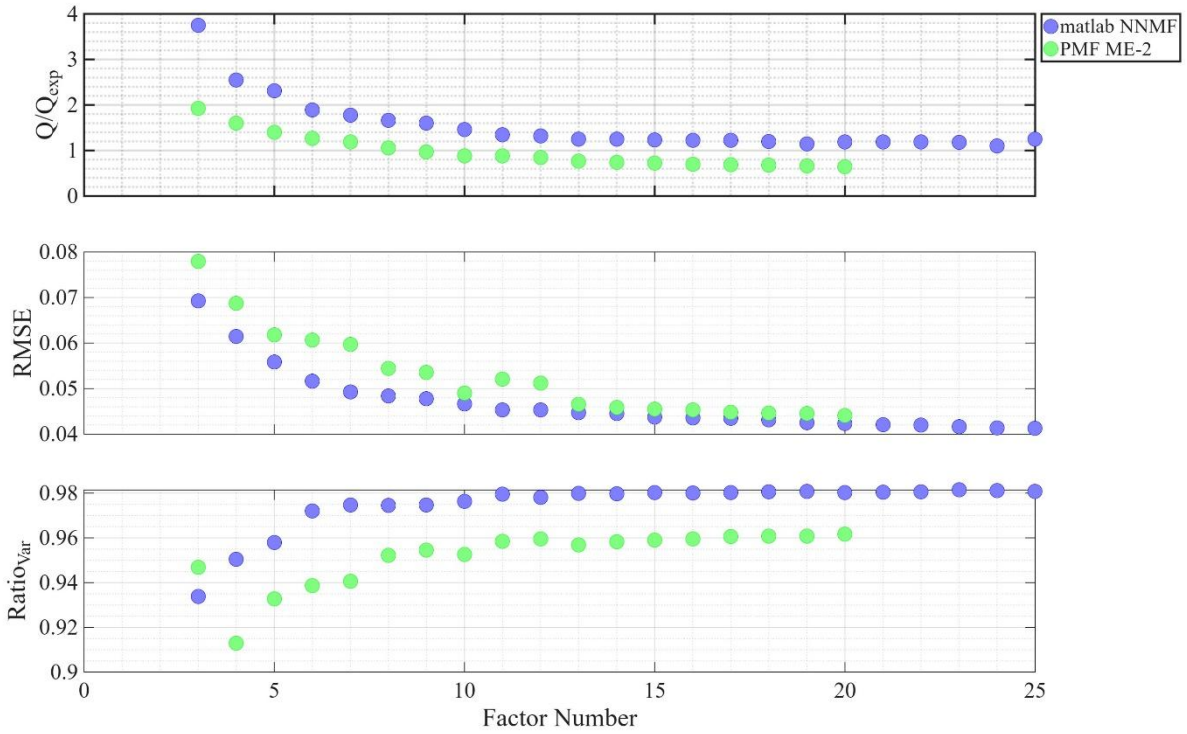

Figure S9 Evolution of global goodness parameters Q/Q_{exp}, RMSE, and $Ratio_{Var}$ while adding factor number to ME-2 PMF & MATLAB® NNMF results using normalized FIGAERO-CIMS data time series as factorization input

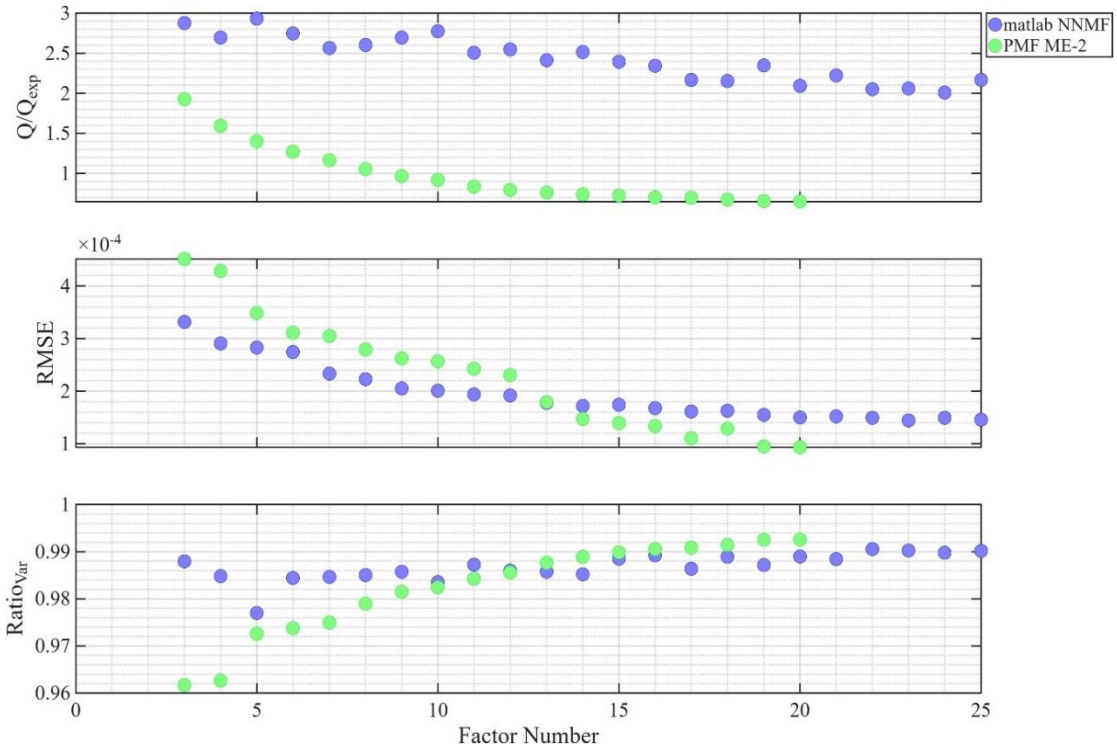

Figure S10 Evolution of global goodness parameters Q/Q_{exp}, RMSE, and $Ratio_{Var}$ while adding factor number to ME-2 PMF & MATLAB® NNMF results using particle-phase only FIGAERO-CIMS data time series as factorization input

Table S4 Possible best factor number list of factorization algorithms with various data pre-treat methods. Red bold number shows the chosen best factor number among results in certain factorization and pre-treat method

Possible best factor number	Full time series	Normalized full time series	Particle-phase only
ME-2 PMF	6,10,11,**13**,15	8,11,**13**,15	**8**,9,12,14
MATLAB® NNMF	6,**10**,15	7,**11**,15	**6**,9,12

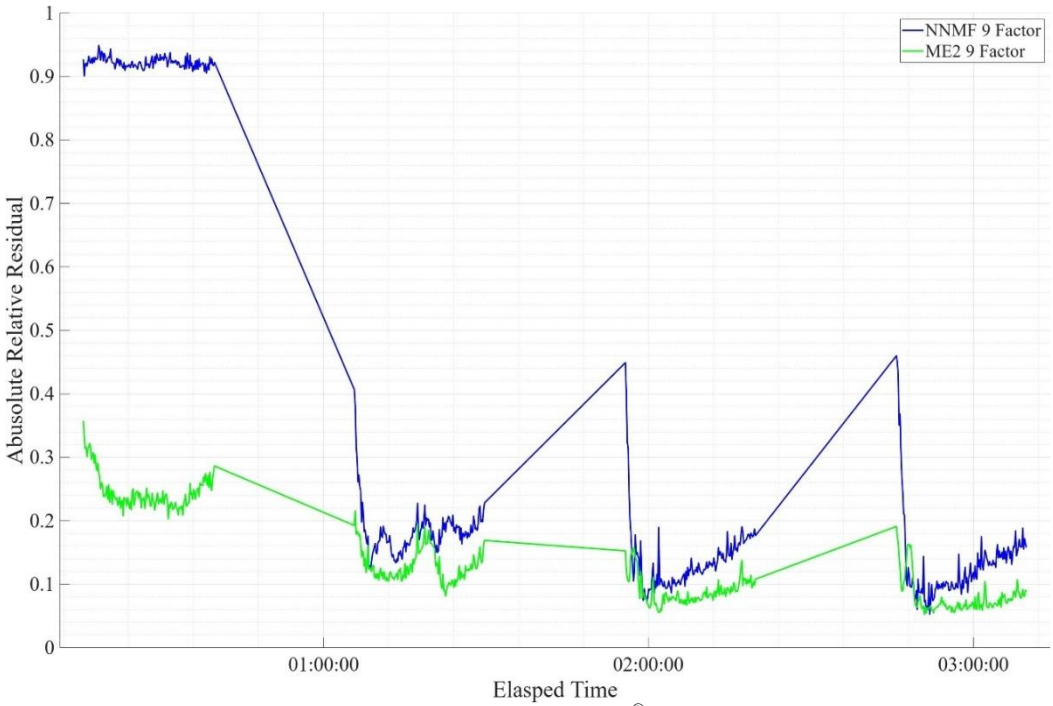

Figure S11 Time series of absolute relative residual for MATLAB® NNMF results (blue line) and ME2 results (green line) of particle-phase only FIGAERO-CIMS datasets at selected 'best' factor numbers

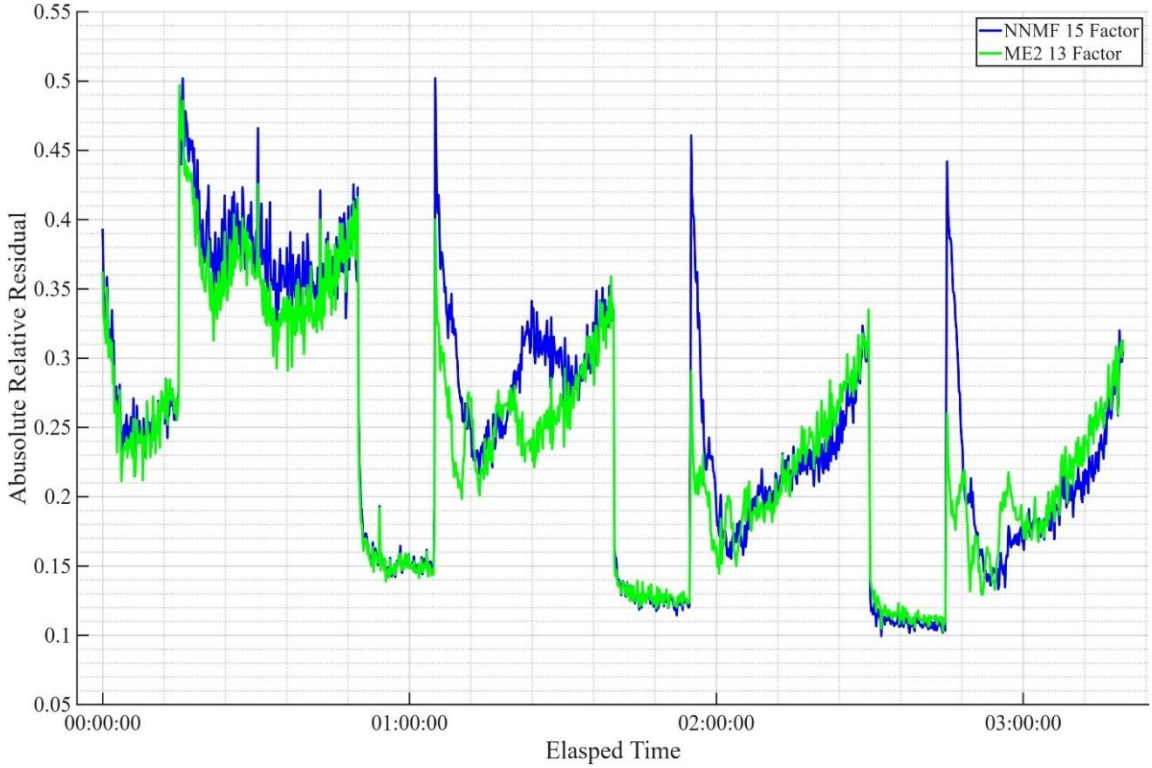

Figure S12 Time series of absolute relative residual for MATLAB® NNMF results (blue line) and ME2 results (green line) of FIGAERO-CIMS datasets normalized to maximum value in the time series at selected 'best' factor numbers

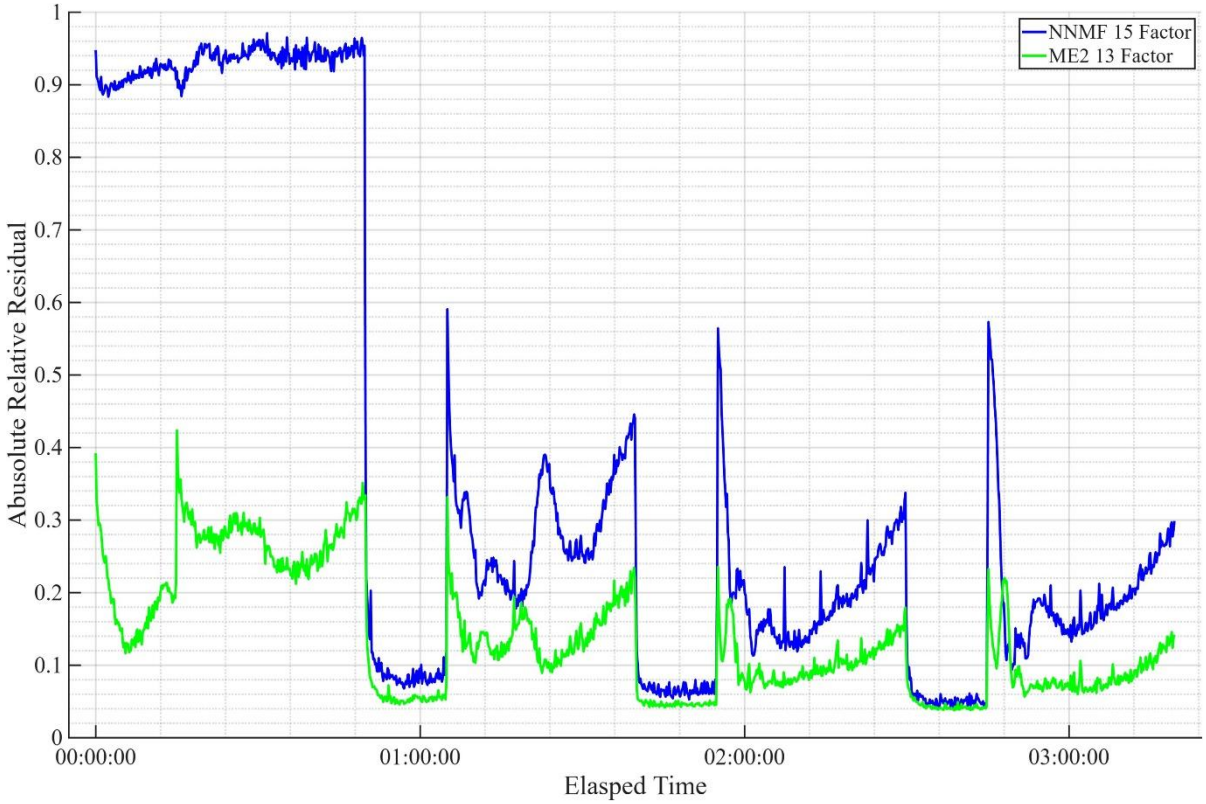

Figure S13 Time series of absolute relative residual for MATLAB® NNMF results (blue line) and ME2 results (green line) of FIGAERO-CIMS normal datasets at selected 'best' factor numbers

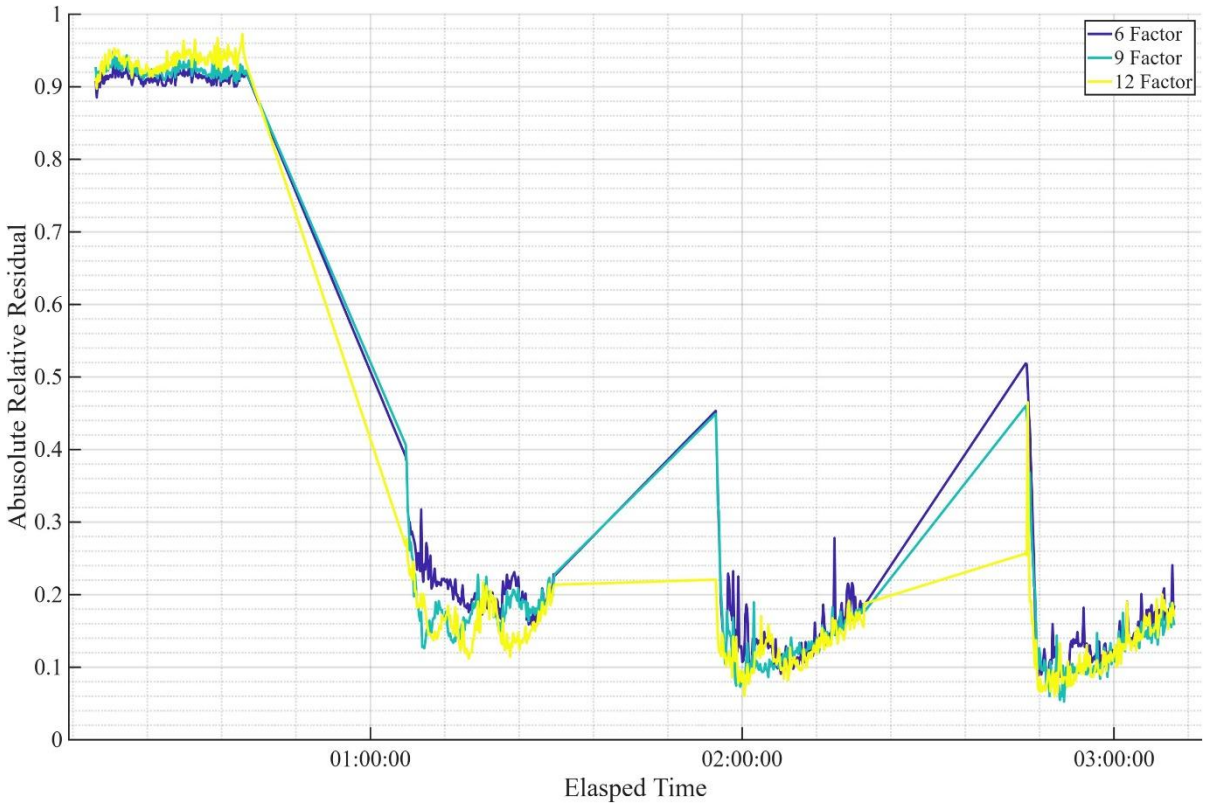

Figure S14 Detailed absolute relative residual time series of factorization results of particle-phase only data utilizing MATLAB NNMF at factor number 6, 9 and 12 which are selected to be right at “turning points”

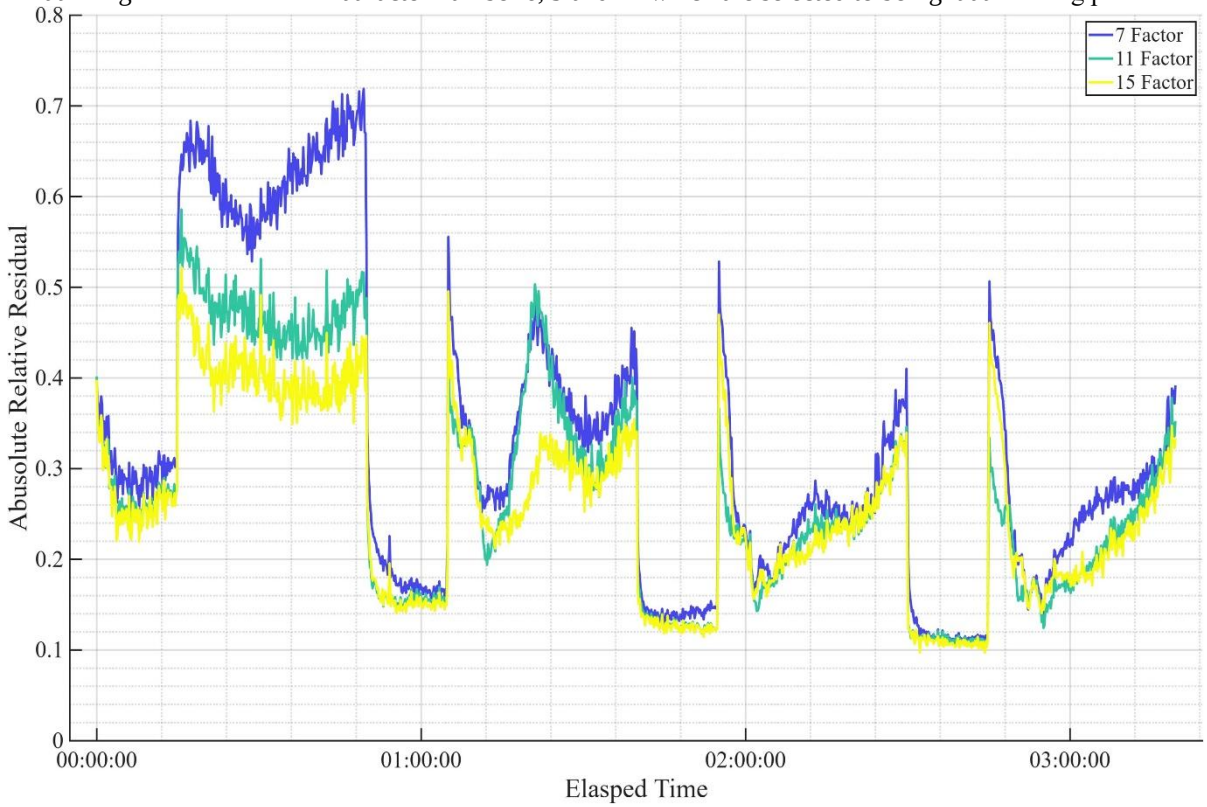

Figure S15 Detailed absolute relative residual time series of factorization results of normalized full time-series data utilizing MATLAB NNMF at factor number 7,11 and 15 which are selected to be right at “turning points”

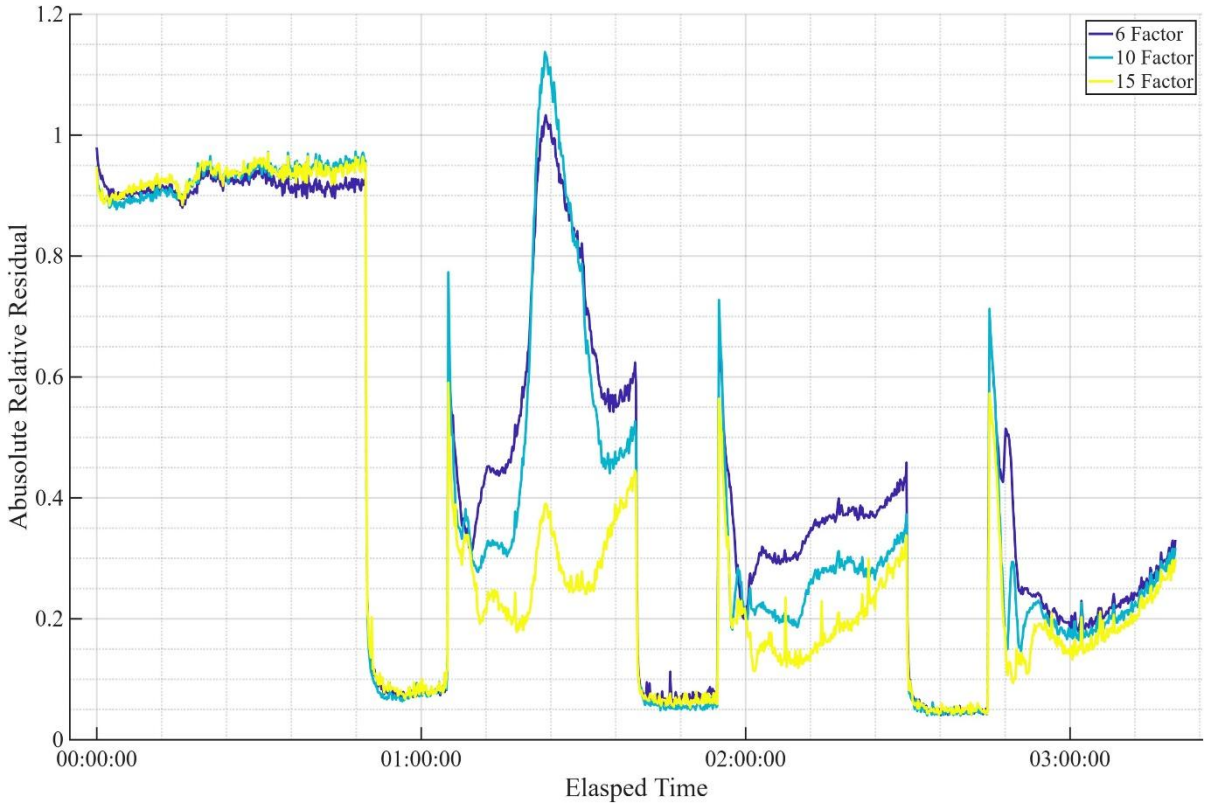

Figure S16 Detailed absolute relative residual time series of factorization results of full time-series data utilizing MATLAB NNMF at factor number 6,10 and 15 which are selected to be right at “turning points”

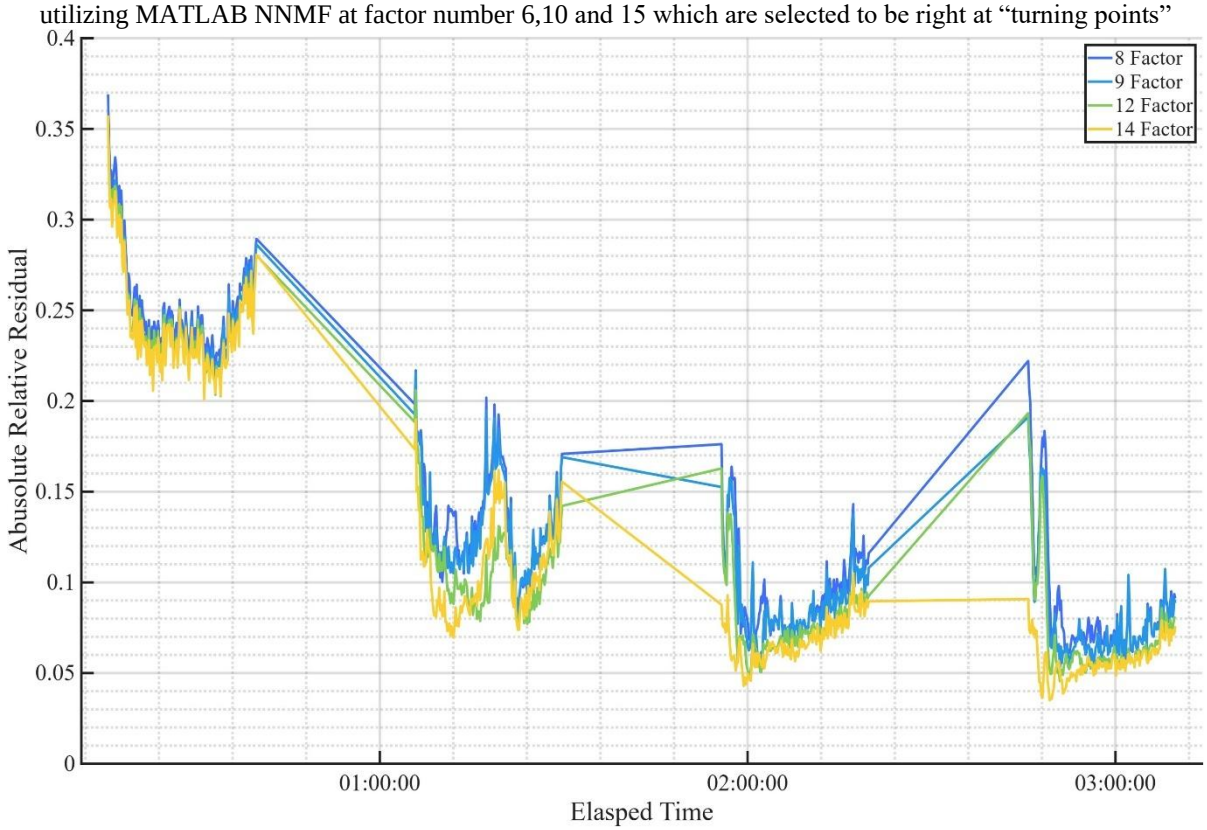

Figure S17 Detailed absolute relative residual time series of factorization results of particle-phase only data utilizing ME-2 PMF with 8,9,12 and 14 factors which are selected to be right at “turning points”

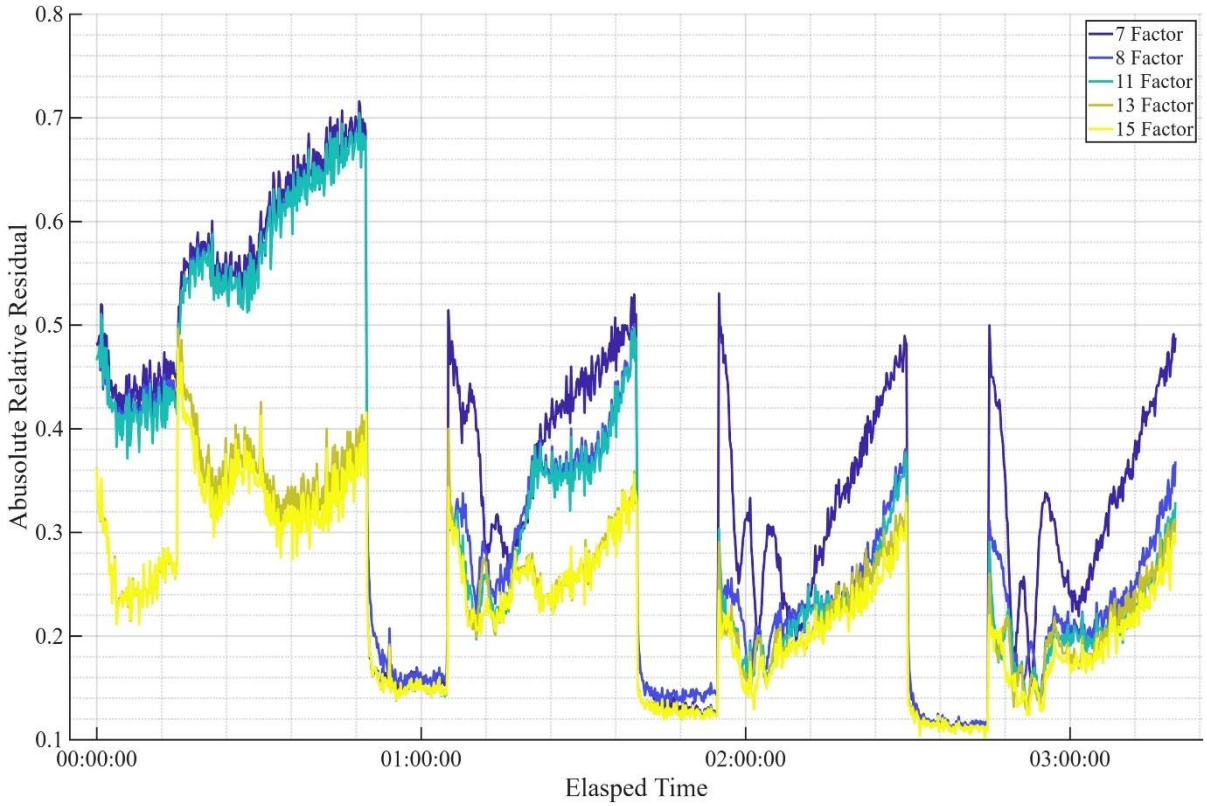

Figure S18 Detailed absolute relative residual time series of factorization results of normalized full time-series data utilizing ME-2 PMF with 7,8,11,13 and 15 factors which are selected to be right at "turning points"

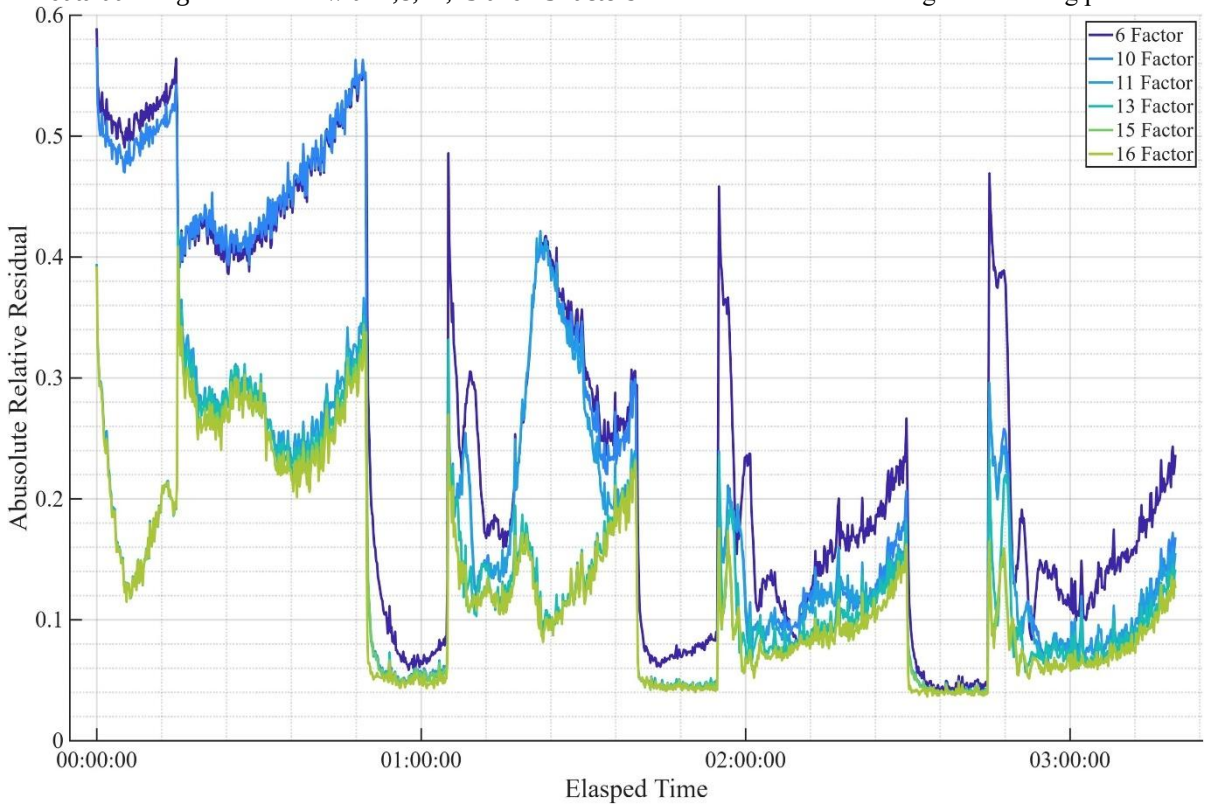

Figure S19 Detailed absolute relative residual time series of factorization results of full time series data utilizing ME-2 PMF with 6,10,11,13,15 and 16 factors which are selected to be right at "turning points"

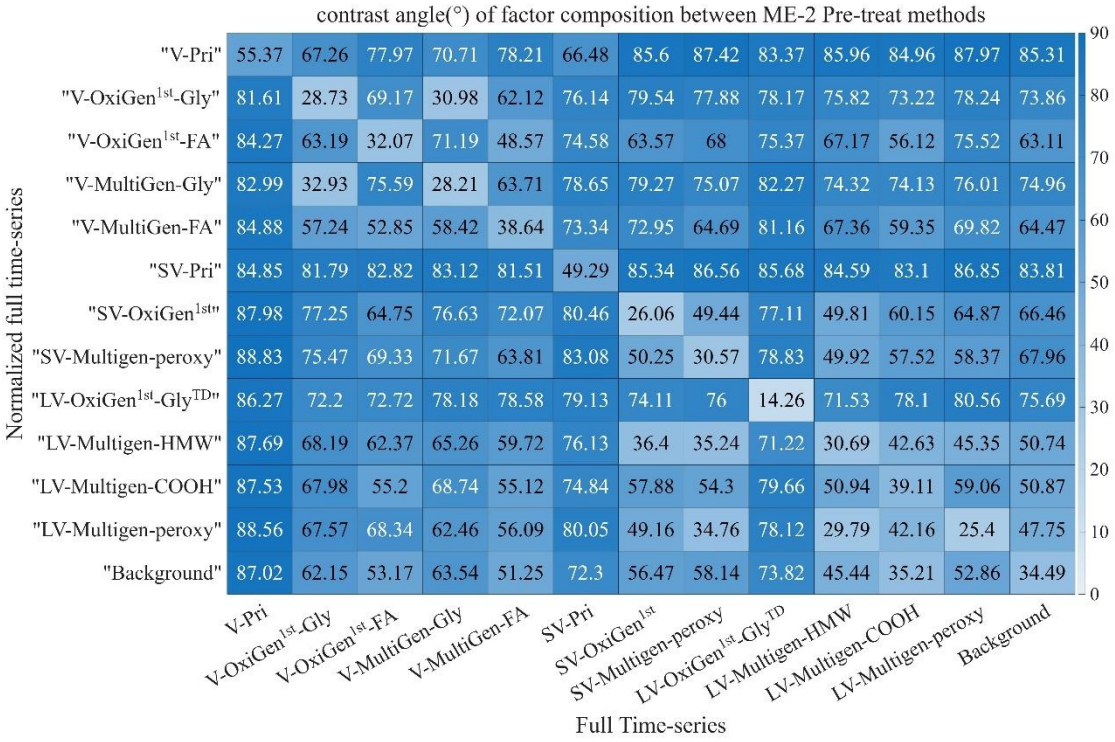

Figure S20 Contrast angle in degree between factors resolved by ME-2 PMF utilizing full time series and normalized time series as database selection method

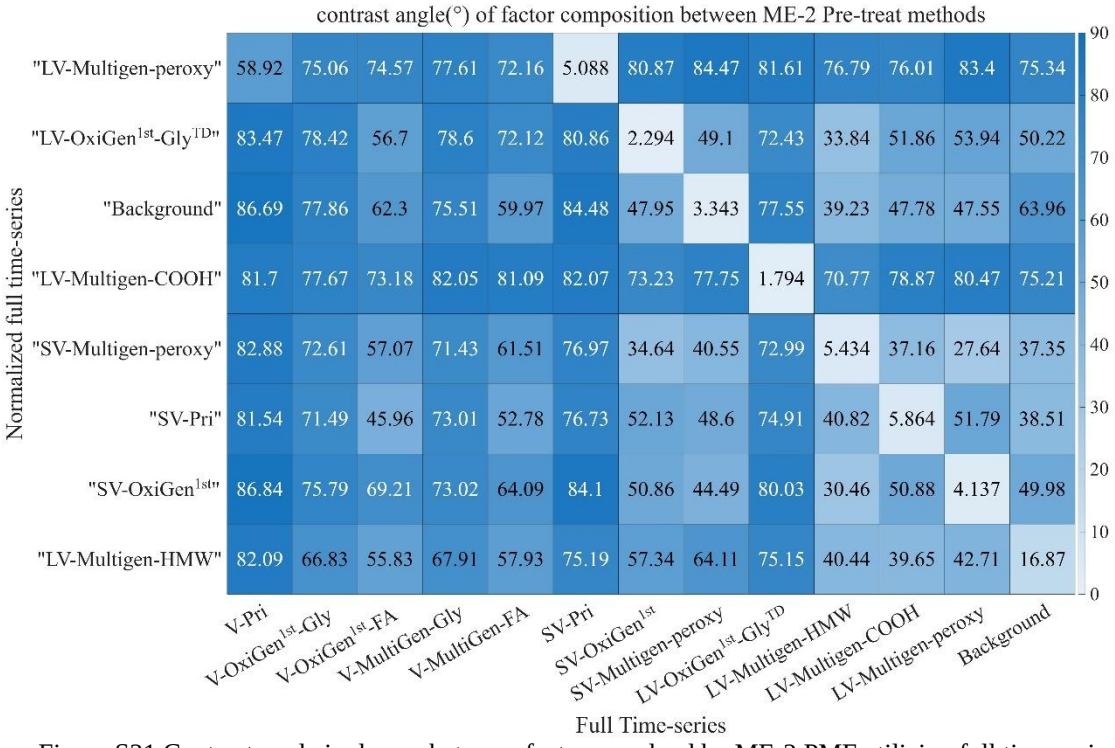

Figure S21 Contrast angle in degree between factors resolved by ME-2 PMF utilizing full time series and particle phase only time series as database selection method

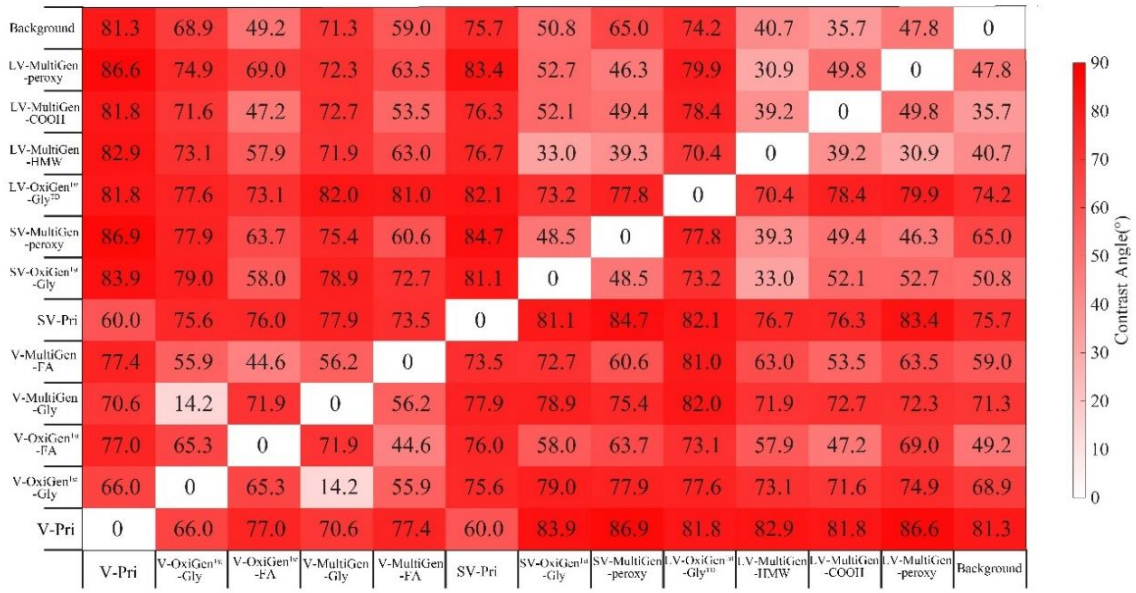

Figure S22 Contrast angle in degree between factors resolved by ME-2 PMF

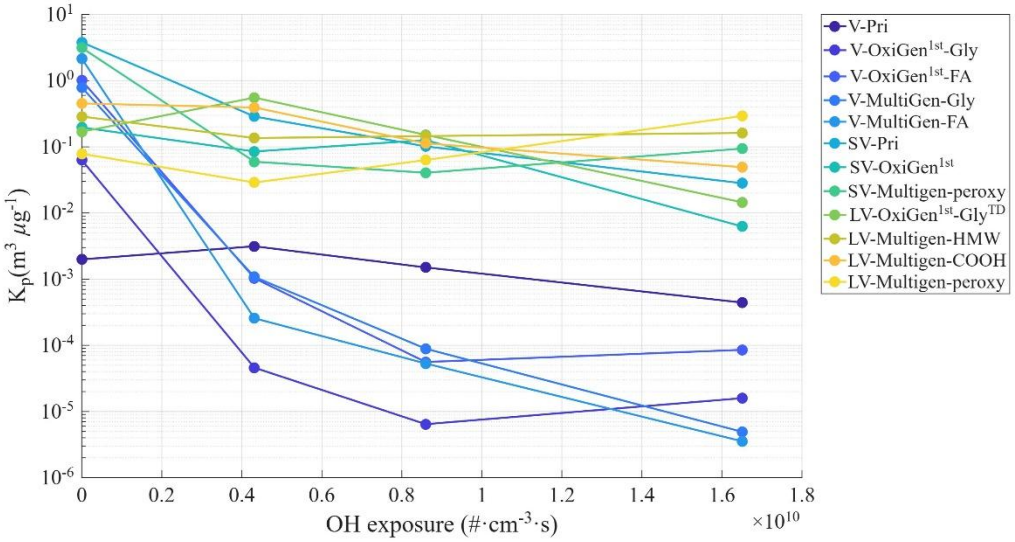

Figure S23 Evolution of factors' gas-particle partitioning coefficient K_p with enhancement of OH exposure during oxidation process and classification by its volatility

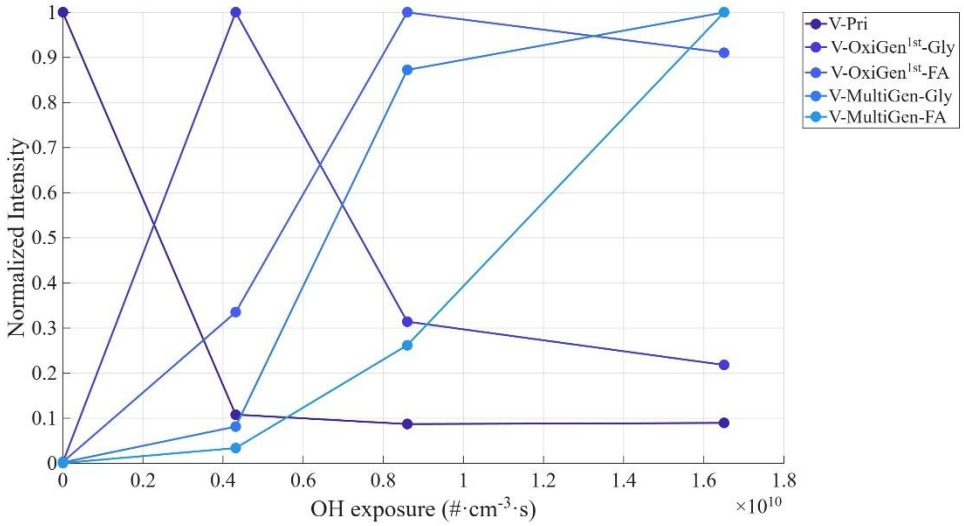

Figure S24 Evolution of factors' average relative intensity classified as volatile factor (only abundant in gas

phase) with enhancement of OH exposure during oxidation process

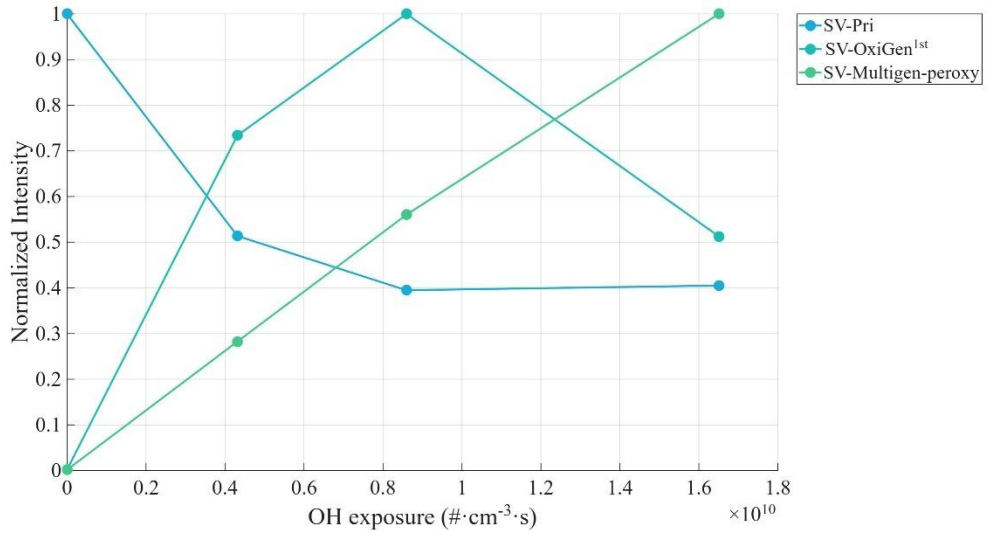

Figure S25 Evolution of factors' average relative intensity classified as semi-volatile factor (both abundant in gas phase and aerosol phase) with enhancement of OH exposure during oxidation process

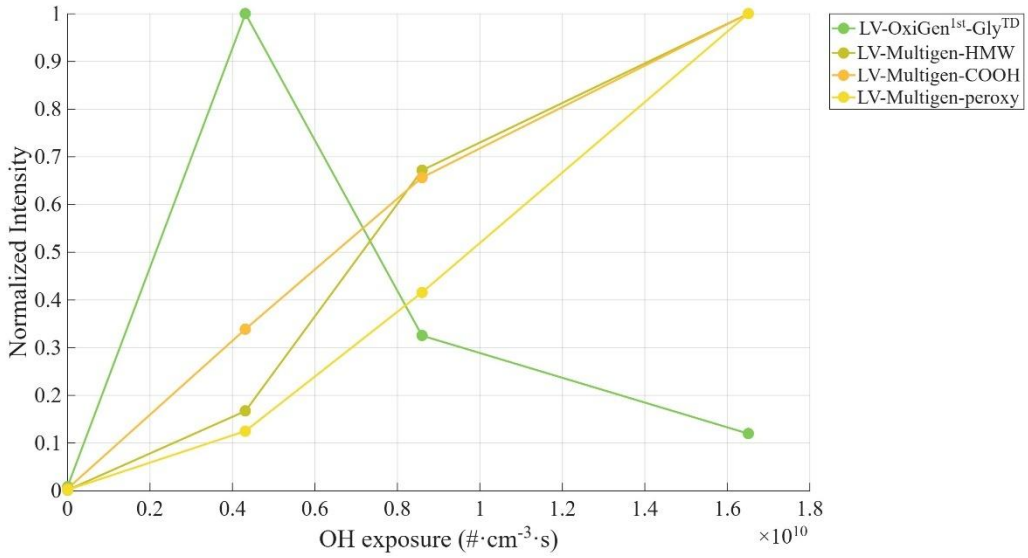

Figure S26 Evolution of factors' average relative intensity classified as low-volatile factor (only abundant in aerosol phase) with enhancement of OH exposure during oxidation process

S5. Gas-particle partitioning kinetics and thermodynamics

Analysis of volatility and gas-particle partitioning thermodynamics of organic compounds detected by FIGAERO-CIMS are processed by gas-phase and aerosol-phase concentration. Direct gas-particle partitioning characteristics are shown by particle-phase fraction F_p, shown in Equation S19:

$$F_{p,i} = \frac{c_{p,i}}{c_{g,i}+c_{p,i}} \quad \text{Eq. S19}$$

In Equation S19, $c_{p,i}$ stands for particle phase concentration of substance i, $c_{g,i}$ means gas phase concentration. Partitioning coefficient K_p, considering influence organic aerosol as substrate of compound i, is defined in Equation S20：

$$K_{p,i} = \frac{c_{p,i}/c_p}{c_{g,i}} \quad \text{Eq. S20}$$

In Equation S20, c_p means total particle concentration. F_p and $K_{p,i}$ can be directly derived from FIGAERO-CIMS gas-particle simultaneous detection of certain compound (including iodide-adduct ion $[RI^-]$ or proton-extraction ion $[R\text{-}H]^-$ corresponding to species R), and aerosol mass concentration, shown in Equation S21-22:

$$(F_{p,i})_{exp} = \frac{\overline{([RI^-]/[I^-])}_{aero} \cdot Q_{TD} \cdot \Delta t_{TD}}{[\overline{([RI^-]/[I^-])}_{gas} \cdot Q_{col} \cdot \Delta t_{col} + \overline{([RI^-]/[I^-])}_{aero} \cdot Q_{TD} \cdot \Delta t_{TD}]} \quad \text{Eq. S21}$$

$$(K_{p,i})_{exp} = \frac{\overline{([RI^-]/[I^-])}_{aero} \cdot Q_{TD} \cdot \Delta t_{TD}}{[\overline{([RI^-]/[I^-])}_{gas} \cdot Q_{col} \cdot \Delta t_{col}] \cdot \overline{c_{p,SMPS}}} \quad \text{Eq. S22}$$

In Eqs. S21-22, Δt_{TD} and Q_{TD} means, particle-phase thermal desorption duration and flow rate, Δt_{col} and Q_{col} stand for collection duration and flow rate, $c_{p,SMPS}$ means average SMPS-measure particle concentration during particle collection period of FIGAERO-CIMS measurements. Eq. S21-22 can be used to classify PMF factor from volatility angle by substituting intensity of certain compound ($[RI^-]/[I^-]$) with the intensity of PMF-extracted factors.

Absorptive partitioning mechanisms are adopted in gas-particle partitioning thermodynamic characteristics in cooking POA and SOA(Pankow, 1994; Odum et al., 1994), as organic compounds existing in aerosol phase composite of an liquid-organic-solution-like or semi-solid-like phase state(May et al., 2012; Hou et al., 2025; Liu et al., 2025a; Reyes-Villegas et al., 2018; Masoud et al., 2022). Considering the mechanism of absorptive partitioning, F_p is related to mass of total particle phase organics c_{OM}, shown in Equation S5.5(Odum et al., 1996), while K_p only depends on properties of compound i and particle phase composition. Assuming gas-particle partitioning of component i reaches equilibrium, partitioning coefficient $K_{p,i}$ is determined by its volatility and composition of aerosol matrix, as shown in Equations S23-24:

$$(F_{p,i})_{theo} = \left(1 + \frac{c^*}{c_{OM}}\right)^{-1} \quad \text{Eq. S23}$$

$$(K_{p,i})_{theo} = \frac{RTf_{OM}}{\overline{MW_{OM}} p^0_{L,i} \xi_i} \quad \text{Eq. S24}$$

In Eqs. S23-24, f_{OM} means mass fraction of organic compounds in aerosols, which equals to 1 in this study as inorganic aerosols are rarely formed in cooking aerosols(Rogge et al., 1991; Mcdonald et al., 2003; Abdullahi et al., 2013; Zhang et al., 2020). MW_{OM} stands for average molecular weight among all species in organic aerosol. $p^0_{L,i}$ means saturated vapor pressure of component i over liquid pure component surface. ξ_i means activity coefficient in particle phase. Assuming ξ_i close to unity, the volatility of component i can be determined from gas-particle partitioning of component. If we are able to classify the exact structure from possible reaction pathways during oxidation of utilize estimation method

of volatility from corresponding compound detected by CIMS such as SIMPOL(Pankow and Asher, 2008; Compernolle et al., 2011) .We could also adopt 2-D VBS approach shown in Section S3 to calculate volatility, activity coefficients and K_p of certain species, which may lead to larger bias due to its simple parameterization. Volatility of species i can be also determined by thermogram from thermal desorption measurements of particle phase according to methods mentioned in Section S2(Ren et al., 2022; Chen et al., 2024), which may be more accurate than partitioning method due to possible interference of FIAGERO collection such as thermal decomposition and matrix effect of the PTFE filter(Caudillo et al., 2023; Ylisirniö et al., 2021; Ylisirniö et al., 2025). Activity coefficient ξ_i can be determined by utilizing 2-D-VBS parametrization or using group-contribution model. In this study, we utilized AIOMFAC-web(https://aiomfac.lab.mcgill.ca/)(Zuend and Seinfeld, 2012), choosing concentration of 50 most abundant compounds in aerosol at each oxidative exposure, treat residual compounds as same molecule with composition equal to average composition of these compounds, to resolve the activity coefficients of most abundant compounds. We also determine the activity of these most abundant compounds to ensure whether liquid-liquid separation occurs in cooking aerosols.

Kelvin effects and influence on gas-particle partitioning are also estimated as it would be essential in particles with diameter ~10nm. Influence of kelvin effect on partitioning are shown in Equation S25. Kelvin effect on gas-particle partitioning is linked to diameter d_p and surface tension σ_i (set to 0.05N s^{-2})(Schmedding et al., 2025; Bain, 2024).

$$p_i^* = \xi_i x_i p_{L,i}^0 / Ke_i = \xi_i x_i p_{L,i}^0 exp(\frac{4V_{m,i}\sigma_i}{RTd_p}) \quad \text{Eq. S25}$$

Gas-particle partitioning of organic species may not reach equilibrium due to kinetic limitations in transportations of molecules in gas phase, at surface or in aerosol phase. Gas-particle partitioning kinetics consist of gas phase diffusion, surface accommodation and particle-phase diffusion processes. Kinetics are characterized by gas-phase diffusion coefficient $D_{g,i}$, surface accommodation coefficient α, particle-phase diffusion coefficient $D_{p,i}$, and corresponding characteristic time scales τ_g, τ_{surf} and τ_p. Gas phase diffusion coefficient of species i in real atmosphere are calculated based on elemental composition of selected species from Fuller's method(Fuller et al., 1966; Tang et al., 2015):

$$D_{g,i} = \frac{1.0868 \times T^{1.75}}{p \cdot \sqrt[3]{m(i,A)} \cdot (\sqrt[3]{V_A} + \sqrt[3]{V_i})^2} \quad \text{Eq. S26}$$

In equation S26, $D_{g,i}$ is in $cm^2\ s^{-1}$, T and p stand for atmospheric temperature and pressure in Kelvin and Torr, m(i,A) means reduced molar mass of species i and ambient air in g/mol, V_i and V_A are molecular diffusion volume of ambient air and selected species i that are directly derived from elemental

composition of molecules(Reid et al., 1987; Tang et al., 2015). Most organic species involved in gas-particle partitioning have diffusion coefficient within 10^{-2} to 10^{-1} $cm^2\ s^{-1}$ level utilizing Eq.S5.8(Tang et al., 2015). Diffusion time scale corresponding to gas-phase diffusion τ_g are inverse proportional to the gas-phase diffusion rate constant $k_{gp,i}$, determined by Equations S27-30(Shiraiwa and Pöschl, 2021; Shiraiwa et al., 2011; Seinfeld, 2016):

$$\tau_{g,i} = 1/k_{gp,i} \quad \text{Eq. S27}$$

$$k_{gp,i} = \sum_p 2\pi D_{g,i} d_p N_p \beta \quad \text{Eq. S28}$$

$$\beta = \frac{0.75\alpha_s(1+Kn)}{Kn^2+Kn+0.283Kn\alpha+0.75\alpha_s} \quad \text{Eq. S29}$$

$$Kn = \frac{3D_{g,i}}{\omega r_p} \quad \text{Eq. S30}$$

In Equations S27-30, d_p is particle diameter, and N_p is particle number concentration at certain diameter range, both measured by SMPS; β is Fuchs-Sutugin correction factor in transition regime of gas-phase diffusion that is related to Knudsen number Kn and surface mass accommodation coefficient α_s (Fuchs and Sutugin, 1971), ω is mean thermal velocity of species i. In Eqs. 27-30, the ability of species i to adsorb onto particle surface has been accounted by factor β. Till now, surface mass accommodation coefficient α has been measured by well-designed thermodynamic experiments, and has been quantified to be usually in the range of 0.1-1 in the atmosphere(Li and Bourg, 2023; Davidovits et al., 2006; Davidovits et al., 1991; Julin et al., 2014; Kolb et al., 2010; Liu et al., 2019), while could reach 10^{-5} in highly-oxygenated and highly-viscous aerosols(Vaden et al., 2011; Saleh et al., 2013). In this study, we choose two parameterization method based on transition-state-theory to estimate α_s values on liquid-like aerosol surface.

Parameterization Method 1 developed by Davidovits et al. is based on the assumption that transition state of adsorption process onto liquid is a critical molecule cluster containing N^* molecules. In this assumption, the critical molecule cluster reaches its local energy maxima at size of N^* molecules, consisting of one adsorbing molecule and several surface molecules. Thus, α_s depends on the formation free energy of critical cluster at the surface ΔG_{N^*}, corresponding to the activation energy of adsorption. α_s are calculated based on Eqs. S31-32(Davidovits et al., 1991)

$$\Delta G_{N^*} = -(N^*-1)\frac{2\sigma\overline{MW_{OM}}/\rho}{\sqrt[3]{(N^*-1)\frac{3V_m}{4\pi N_A}+r_i^3}} + \left(N^{*2/3}-1\right)4\pi\sigma\sqrt[3]{\frac{3V_m}{4\pi N_A}} \quad \text{Eq. S31}$$

$$\frac{\alpha_s}{1-\alpha_s} = \exp\left(-\frac{\Delta G_{N^*}}{RT}\right) \quad \text{Eq. S32}$$

In Eqs.S31-32, $N^*$is the molecular number of the critical cluster. The actual behavior of molecules on the surface would result in a non-integer N^* known as "effective molecular size"; σ means surface tension of aerosols, V_m=$\overline{MW_{OM}}/\rho$ means molar volume of aerosol phase, r_i means size of condensing molecules, set to hydrodynamic radius a of condensing molecule.

α_s parametrization method 2 are based on molecular dynamics near the surface. This method derives α_s from its definition "probability of a molecule that reach surface to adsorb onto", and this probability are connected to obstacle of surface on thermal motion. Thermal motion of molecules is connected to the free volume and thus the molar volume V_m in gas phase and aerosol phase, thus pre-exponential factor and activity coefficient of the Arrhenius-type function and be determined. The parametrization method yields the parameterization shown in Eq. S33,where α_s is determined by molar volume of gas phase and aerosol phase(Nagayama and Tsuruta, 2003):

$$\alpha_s = (1 - \sqrt[3]{V_{m,l}/V_{m,g}})\exp(-\frac{1}{2\cdot\sqrt[3]{V_{m,g}/V_{m,l}}}) \quad \text{Eq. S33}$$

We note that parameterization methods shown in Eqs. S31-33 and are based on assumption that the aerosol phase is liquid aerosol phase. Method 1 shown in Eq. S33 only account for thermal motion obstacle on surface adsorption, thus serve an upper bound of α_s. Method 2 shown in Eqs. S31-32 account for surface tension and intermolecular interaction; thus, we prefer method 2 as the estimated α_s, and to use α_s=1 in cooking POA and α_s=0.03 in cooking SOA determined by Takhar et al. in thermodynamic property analysis as alternative upper boundary and lower boundary(Takhar et al., 2019; Takhar et al., 2021). The variation of α_s derived from estimation methods and preferred values are shown in Fig. S64.

An effective mass accommodation coefficient $\alpha_{eff}(x)$ as function of penetration depth x into aerosol phase, thus accounting for near-surface-bulk diffusion based on kinetic modeling of cross-surface mass-transfer processes are shown in Equation S34(Shiraiwa and Pöschl, 2021), where x is set to be $d_p/10$:

$$\alpha_{eff} = \alpha_s \frac{1}{1+\frac{\alpha\omega C^0}{4D_{p,i}\rho_p}x} \quad \text{Eq. S34}$$

Diffusion coefficient of species i, $D_{p,i}$, are refined by particle phase viscosity ν. The Stokes-Einstein relation of deriving $D_{p,i}$ from particle phase viscosity are shown in Equation S35(Shiraiwa et al., 2011):

$$D_{p,i} = \frac{kT}{6\pi a\nu} \quad \text{Eq. S35}$$

In Eq. S35, k is Boltzmann constant, T is particle-phase temperature, a means effective molecular diameter in molecular diffusion, or so-called 'hydrodynamic radius/radii', which are derived based on estimation utilizing molecular weight(Fleming and Fleming, 2018)(https://www.fidabio.com/molecular-

weight-to-size-protein-radius-calculator). The effective molecular diameter of organic compounds in atmospheric organic aerosols are at the level of several Å(Miyamoto and Shimono, 2020; Zwanzig and Harrison, 1985).

Parametrization of particle-phase viscosity ν are estimated by several methods. Viscosity generated from AIOMFAC-web output utilizing AIOMFAC-VISC model are selected as one of the reference viscosities(Lilek and Zuend, 2022). Modified Vogel–Tammann–Fulcher method links glass transition temperature T_g of particle bulk to viscosity at certain temperature, as shown in Equation S36(Derieux et al., 2018):

$$\log_{10} \nu = \log_{10} \nu_\infty + 0.434 \frac{T_0 D}{T - T_0} \quad \text{Eq. S36}$$

In Eq. S36, ν_∞=10^{-5} Pa s means viscosity limits when temperature tends to infinity, T stands for ambient temperature, T_0 means Vogel temperature that derived from glass-transition temperature, D=10 means sensitivity of viscosity to temperature changes(Angell, 1991, 2002; Shiraiwa et al., 2017; Derieux et al., 2018). Vogel temperature can be determined in Equation S5.19 assuming viscosity to be 10^{12} Pa when temperature reaches $T_{g(\text{Derieux et al., 2018})}$:

$$T_0 = \frac{39.17 T_g}{D + 39.17} \quad \text{Eq. S37}$$

For T_g parameterization, several methods are utilized and compared in this study. A simple 2-D-VBS-space based parametrization method introduced by Derieux et al. are adopted to acquire a comparable result to 2-D-VBS-based thermodynamics, where T_g (K)can be directly derived from elemental composition, shown in Equation S5.16. Parameters used in Eq. S38 are shown in Table S5(Li et al., 2020; Derieux et al., 2018)

$$T_g(K) = b_C \cdot (n_C^0 + ln(n_C)) + b_H \cdot ln(n_H) + b_{CH} \cdot ln(n_C) \cdot ln(n_H) + b_O \cdot ln(n_O) + b_{CO} \cdot ln(n_C) \cdot ln(n_O) \quad \text{Eq. S38}$$

Table S5 Parameters used in glass transition temperature parametrization method developed by Derieux et al., 2018

Parameters	Molecular composition			
	CH	CHO	CHON	CHOS
n_C^0	1.96	12.13	5.34	1.12
b_C	61.99	10.95	31.53	68.41
b_H	-113.33	-41.82	-	-
b_O	-	118.96	-7.06	64.95
b_N	-	-	134.96	-
b_S	-	-	-	35.77

b_{CH}	28.74	21.61	-	-
b_{CO}	-	-24.38	6.54	-12.32
b_{CN}	-	-	-34.36	-
b_{CS}	-	-	-	-9.85
b_{ON}	-	-	-15.35	-
b_{OS}	-	-	-	13.8

A machine learning method tgBoost for retrieving glass transition temperature from molecular structure represented by SMILES string are utilized in this study as reference. Over 130000 compounds containing CHONS elements are chosen from NCI database (https://cactus.nci.nih.gov/ncidb2.2/)(Sitzmann et al., 2013) and entered the tgBoost website to achieve their glass-transition temperatures of the full database(https://azoth-frontend-lb-9735005.us-west-2.elb.amazonaws.com/)(Galeazzo and Shiraiwa, 2022). The estimated T_g of species detected by CIMS are set to mean T_g of compounds from tgBoost with same elemental compositions. tgBoost result in a lower T_g than other parameterization methods in estimating multifunctional compounds such as dicarboxylic acids and peroxides.

Another simple T_g estimation method is empirical linear estimation between T_g and melting point T_m. The relation is shown in equation S39: (Derieux et al., 2018; Berkemeier et al., 2014)

$$T_g = 0.70085 \cdot T_m \quad \text{Eq. S39}$$

T_g of bulk organic aerosols are determined utilizing Gordon-Taylor equation. Assuming the Gordon-Taylor constant to be equals to 1, resulting in a mass-fraction(w_i)-weighted average of single compounds, shown in Equation S5.22. $T_{g,bulk}$ would be used in Eqs. S39-40 to determine diffusion coefficient of species in bulk aerosols (Derieux et al., 2018; Li et al., 2020; Shiraiwa et al., 2017; Gordon and Taylor, 1952)

$$T_{g,bulk} = \sum_i T_{g,i} w_i \quad \text{Eq. S40}$$

In real-world diffusion processes within organic aerosols, viscosity would lead to bias away from standard Stokes-Einstein relations, especially for small molecules in viscous matrices, because composition and molecular structure heterogeneity within semi-solid and glassy aerosols lead to internal stress and thus confine transportation of particle compounds (Becker and Poole, 2006; Price et al., 2016; Shiraiwa et al., 2011; Marshall et al., 2016; Mutneja and Karmakar, 2025; Ingram et al., 2021; Pastore et al., 2021). Fractional Stokes-Einstein relations are introduced to close the gap, where $D_{p,i}$ is inversely proportional to ξth power of viscosity rather than viscosity itself(Evoy et al., 2019; Maclean et al., 2021), shown in Equation S41:

$$D_{p,i} = D_c \left(\frac{\nu}{\nu_c}\right)^{\xi}$$ Eq. S41

In Eq. S41, ξ are the fractional power index, set to be 0.93 recommended by Evoy et al.; D_c and ν_c means crossover diffusion coefficients, while ν_c is set to 10^{-3} Pa s. Deborah number De, defined as the ratio of characteristic relaxation time τ_v to the characteristic diffusion time τ_D, are also introduced to ensure whether diffusion in particle phase bias from Stokes-Einstein significantly as shown in Equation S5.21(Preston, 2022; Ferreira et al., 2015):

$$De = \frac{D_{p,i} \nu M_i}{\rho_i^0 r^2 RT}$$ Eq. S42

In Equation S5.21, M_i means molecular weight of species i, ρ_i^0 means density of pure species i, r means diameter of the particle. Deborah number De<<1 indicates diffusion mechanism close to Stokes-Einstein equation, while De>>1 showing diffusion characteristic bias significantly from Stokes-Einstein equation. Maxwell-Stefan diffusion theory is used characterize diffusion in presence of internal stress. The diffusion coefficient between S-E diffusion and M-S diffusion is related to partial deviate of activity coefficients shown in Equation S5.22(Preston, 2022):

$$D_{p,i}(MS) = D_{p,i}(SE) \cdot \left(1 + \frac{1}{x_i \frac{\partial \ln \xi_i}{\partial x_i}_{T,p}}\right)$$ Eq. S43

Gas-particle partitioning kinetic can thus be estimated by time scale of gas-phase diffusion and particle-phase diffusion. Particle-phase diffusion characteristic time scale $\tau_{p,i}$ are shown in Equation S44:

$$\tau_{p,i} = \frac{d_p^2}{4\pi^2 D_{p,i}}$$ Eq. S44

For surface processes, adsorption processes of gas-phase molecules are characterized by mass accommodation coefficient α as shown previously in Eqs. S28-30, while desorption processes are determined by desorption energies. Rate constant of desorption processes $k_{des,i}$ are estimated based on conventional transition state (TS) theory that depends on desorption energy $E^0_{des,i}$ (Knopf and Ammann, 2021; Knopf et al., 2024), as shown in Equation S45:

$$k_{des,i} = A_{des} \cdot \exp\left(-\frac{E^0_{des}}{T}\right)$$ Eq. S45

In Equation S45, A_{des} is pre-exponential factor depends on surface transition kinetics, which is set to 10^{13} s^{-1}; $E^0_{des,i}$ are estimated utilizing 2-D-VBS-based parameterization recommended in their articles as shown in Equations S46-47(Knopf et al., 2024). In Eqs. S46-47, $E^0_{des,i}$ depends on O:C ratio and polarizability α_{polar} . Desorption time scale $\tau_{des,i}$ are thus determined to be inverse number of $k_{des,i}$.

$$E_{des}^{0}(kJ \cdot mol^{-1}) = 25.895 + 2.330\alpha_{polar}(10^{-24}cm^{3}) + 12.367(O:C) \quad \text{Eq. S46}$$

$$\alpha_{polar}(10^{-24}cm^{3}) = 1.51n_C + 0.17n_H + 0.57n_N + 1.05n_O + 2.99n_S \quad \text{Eq. S47}$$

Comparison between characteristic time scales in kinetic processes including $\tau_{g,i}$, $\tau_{p,i}$ and $\tau_{des,i}$, and reference times gives insight into gas-particle partitioning dynamics in the experiment. Reference time includes retention time in Go:PAM t_R(55s), e-folding oxidation-consumption time of oleic acid τ_{oleic}, and characteristic coagulation time τ_{coag}. Characteristic time of oleic acid oxidation are adapted from EPI SUITE(Epa., 2012), while characteristic time of coagulation are generated from SMPS-measured particle size distributions, shown in Equation S48(Nguyen et al., 2026). Coagulation coefficients $K_{i,j}$ are determined by aerodynamic properties discussed in detail in article presented by Nguyen et al. and Chapter 13.3 of Seinfeld et al., assuming coagulation efficiency equals to 1 (Seinfeld, 2016; Nguyen et al., 2026):

$$\tau_{coag,i} = \frac{1}{\sum_j K_{i,j} N_i} \quad \text{Eq. S48}$$

To account for potential effect on underestimation on long-chain-fatty acid related species, we performed a sensitivity test by adding oleic acid and $C_{18}H_{32}O_{4\text{-}8}$ oxidation product to the measured composition. The concentration is set as corresponding to 1/10 of the total ion intensity. The comparison of thermodynamics and kinetics between experimental result as base case and are shown in Figures S66-67.

S6. Additional results

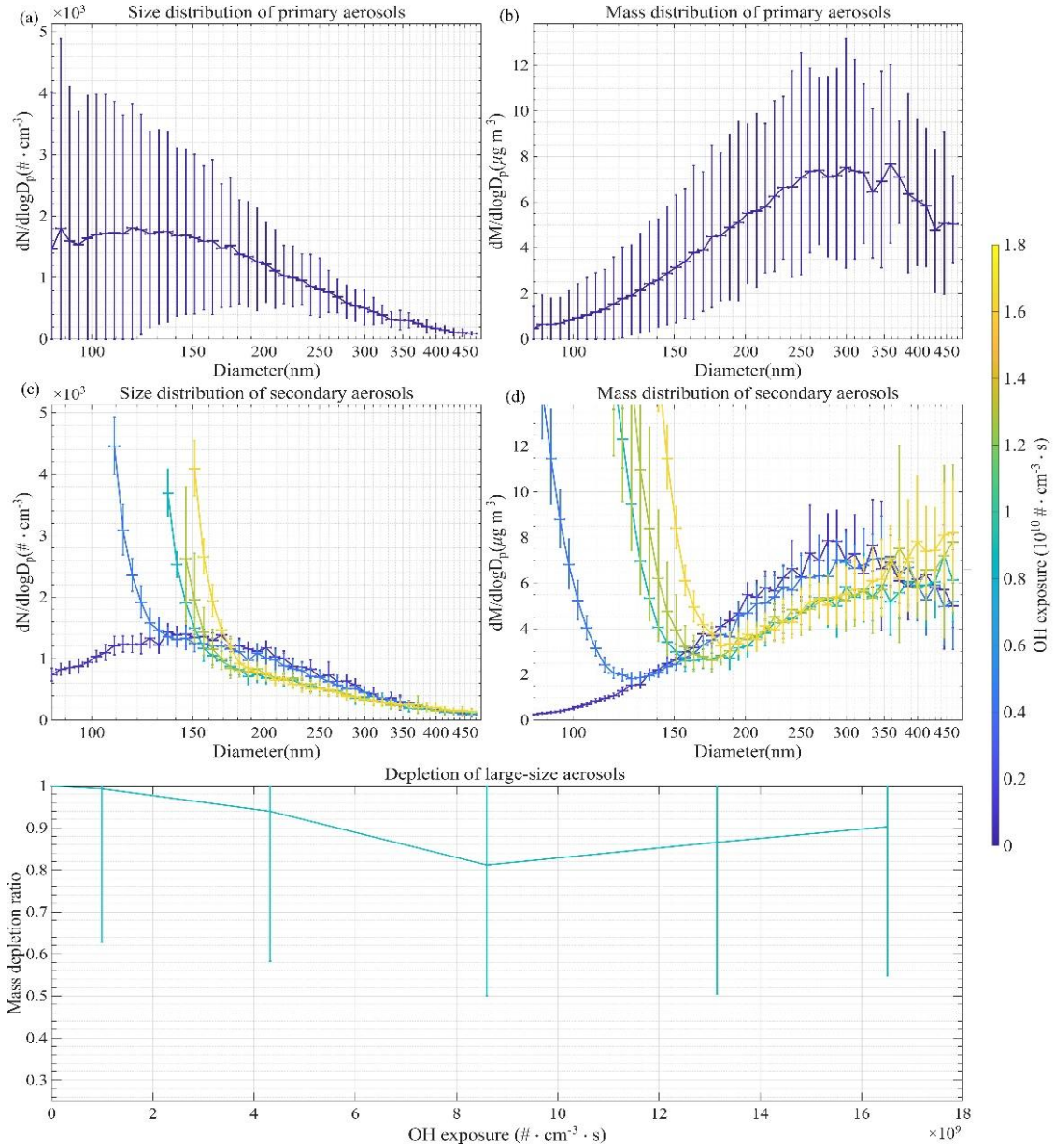

Figure S19 Primary and secondary aerosol size & mass distribution evolution at diameter >90nm with OH exposure growth from 0.1~1.8×10^{10} # cm^{-3} s during oxidation experiments. (a) number distribution, (b) mass distribution of primary aerosols; (c) (d) size and mass distribution of secondary aerosols, (e) total mass shrinking ratio of aerosols after oxidation in Go:PAM flow tube.

Table S6 Size and mass distribution characteristics of primary and secondary cooking aerosol

OH exposure (10^{10} # cm^{-3} s)	OA Mass concentration (μg·m^{-3})	Size distribution mode diameter(nm)	Mass distribution mode diameter(nm)	Density (g cm^{-3})	Number conc. (# cm^{-3})
Primary	3.36	-* 113.4**	-* 289**	1.00* 1.05**	- 1.21×10^{3}
0.099	10.5	14.1* 151.2**	27.9* 279**	1.02* 1.09**	5.64×10^{2} 1.37×10^{6}
0.432	42.8	21.7* -**	46.1* -**	1.03* 1.09**	8.59×10^{2} 2.45×10^{6}
0.860	87.0	27.9*	53.3*	1.02*	3.89×10^{3}

		-**	-**	1.10**	3.07×10^{6}
1.31	107	28.9* -**	55.2* -**	1.06* 1.11**	5.64×10^{3} 3.39×10^{6}
1.65	144	31.1* -**	61.5* -**	1.08* 1.13**	1.18×10^{4} 3.42×10^{6}

* Particle size below 100nm, related to secondary organic aerosols originated from primary vapor oxidation and then OM vapor nucleation and growth

**Particle size over 100nm, related to primary aerosols and condensation

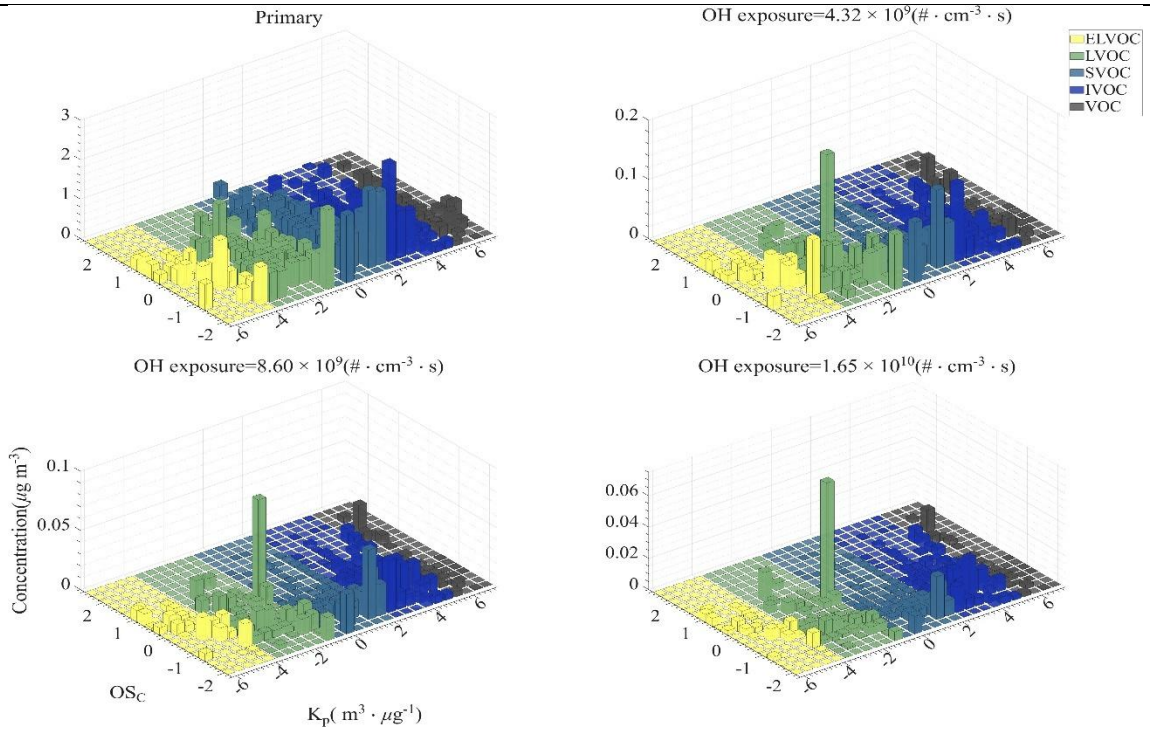

Figure S20 Distribution of primary& secondary cooking aerosols' Gas-particle partitioning coefficient K_p in 2-D VBS space

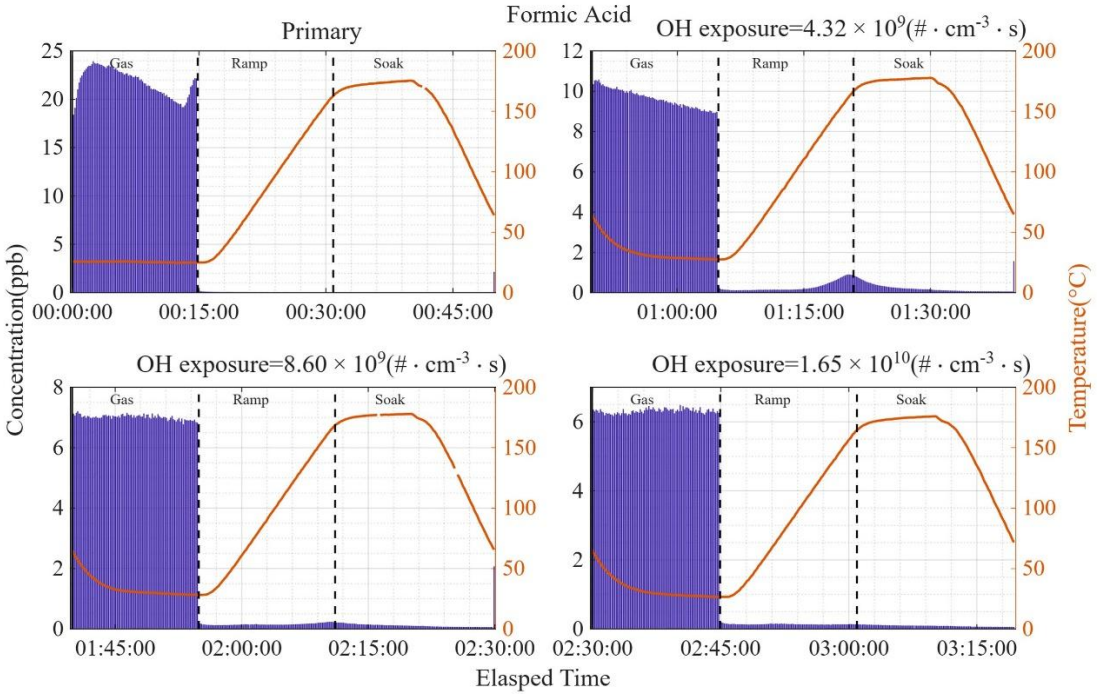

Figure S21 Time series of formic acid concentration at different oxidative state during FIGAERO measurement of flow tube experiment. Concentration of **formic acid and following species** is converted from signal intensity utilizing methods in section S2.

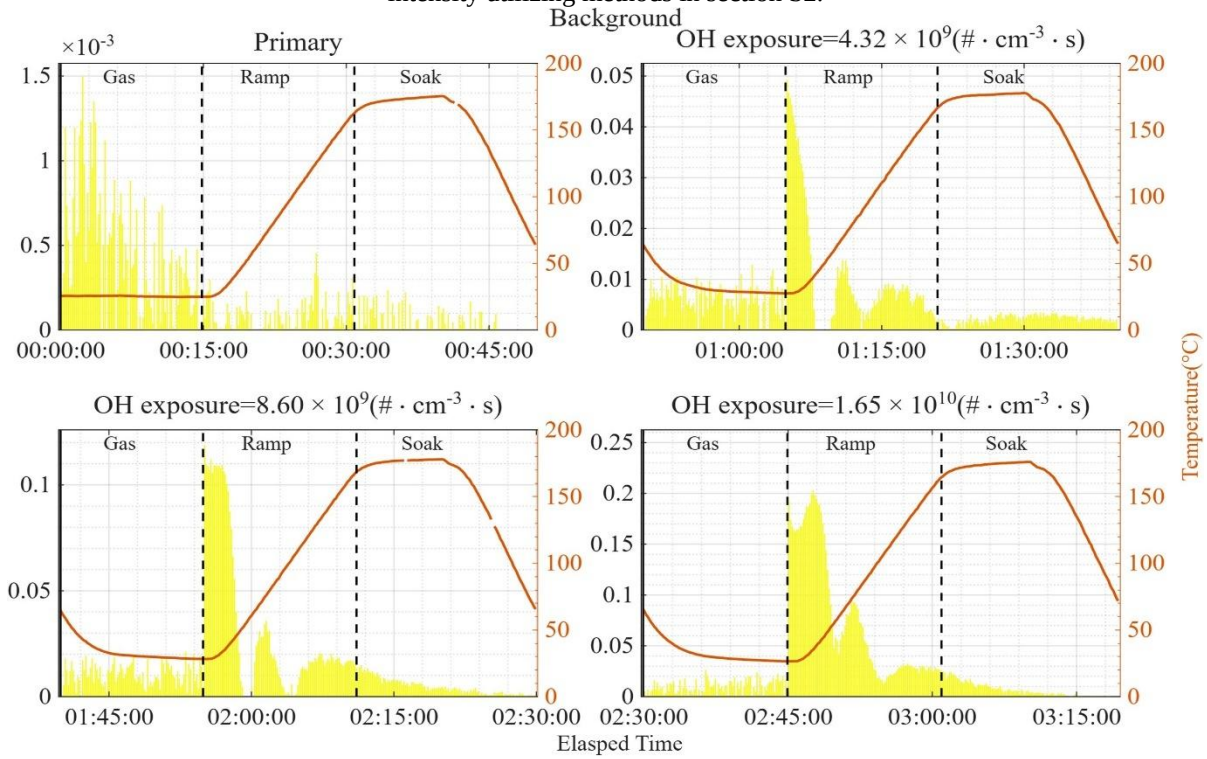

Figure S22 Intensity time series FIGAERO measurement circles of contamination factor Background from ME-2 PMF results at different OH exposure during FIGAERO measurement circles.

Table S7 Average composition and top-20 most abundant species in Factor Background from ME-2 PMF results

Factor Name: Background
Average elemental composition: $C_{5.93}H_{10.15}O_{3.81}N_{0.00}S_{0.00}$ MW=142.37 OS_C=-0.129
Molecular composition:

Molecules	MW(g·mol^{-1})	Relative Intensity	Possible species
$C_3H_4O_4$	104.01	0.68	Malonic acid
$C_6H_{10}O_4$	146.06	0.44	Adipic acid
$C_7H_{12}O_4$	160.07	0.28	Pimelic acid
$C_7H_{14}O_4$	162.09	0.22	Hydroperoxyl heptanoic acid
$C_6H_{12}O_4$	148.07	0.21	Dihydroxy hexanoic acid
$C_9H_{16}O_4$	188.10	0.21	Azelaic acid
$C_6H_{12}O_3$	132.08	0.20	Hydroxy hexanoic acid
$C_6H_{10}O_3$	130.06	0.11	Oxo hexanoic acid
$C_3H_6O_4$	106.03	0.10	Glyceric acid
$C_{10}H_{16}O_3$	184.11	0.10	Oxo-decanoic acid
$C_4H_6O_4$	118.03	0.089	Succinic acid
$C_7H_{12}O_5$	176.07	0.079	Hydroxy pimelic acid
$C_9H_{14}O_4$	186.09	0.076	Nonendioic acid
$C_3H_4O_3$	88.02	0.076	Pyruvic acid
$C_2H_2O_4$	90.00	0.062	Oxalic acid
$C_8H_{14}O_4$	174.09	0.049	Suberic acid
$C_7H_{14}O_3$	146.09	0.048	Hydroxy heptanoic acid
$C_5H_8O_4$	132.04	0.041	Glutaric acid
$C_8H_{16}O_4$	176.10	0.039	Hydroperoxyl octanoic acid
$C_7H_{12}O_3$	144.08	0.039	Hydroxy heptanoic acid

Table S8 Average composition and top-20 most abundant species in factor V-Pri from ME-2 PMF results

Factor Name: V-Pri			
Average elemental composition: $C_{3.20}H_{5.23}O_{2.71}N_{0.01}S_{0.01}$ MW=87.27 OS_c=0.148			
20 most abundant compounds in molecular composition:			
Molecules	Intensity	MW(g·mol^{-1})	Possible species
$C_2H_4O_2$	0.79	60.02	Acetic acid
$C_3H_4O_2$	0.58	72.02	Acrylic acid
$C_5H_4O_4$	0.094	128.01	Hydroxy furoic acid
$C_5H_{10}O_6$	0.089	166.04	Arabic acid
$C_3H_6O_4$	0.083	106.03	Glyceric acid
$C_2H_4O_4$	0.081	92.01	Hydroperoxy acetic acid
$C_3H_4O_3$	0.044	88.02	Pyruvic acid
$C_6H_{12}O_2$	0.037	116.08	Hexanoic acid
$C_3H_6O_3$	0.029	90.03	Lactic acid
$C_6H_{10}O_3$	0.028	130.06	Oxo-hexanoic Acid
$C_4H_6O_4$	0.023	118.03	Succinic acid
$C_2H_4O_3$	0.022	76.02	Glycolic acid
$C_5H_8O_3$	0.020	116.04	Oxopentanoic acid
$C_6H_{12}O_3$	0.020	132.07	Hydroxy hexanoic acid
$C_3H_4O_4$	0.016	104.01	Malonic acid
$C_2H_2O_4$	0.016	89.99	Oxalic acid
$C_3H_8O_3$	0.016	92.05	glycerol
$C_4H_4O_3$	0.014	100.02	Oxo-butenoic acid
$C_4H_4O_4$	0.0085	116.01	Fumaric acid
$C_5H_{10}O_3$	0.0082	118.06	2-Oxo-Pentanoic acid

Table S9 Average composition and top-20 most abundant species in factor SV-Pri from ME-2 PMF results

Factor Name: SV-Pri			
Average elemental composition: $C_{5.00}H_{7.12}O_{3.80}N_{0.01}S_{0.01}$ MW=128.25 OS_C=0.402			
Molecular composition:			
Molecules	Intensity	MW($g \cdot mol^{-1}$)	Possible species
$C_5H_4O_4$	0.84	128.01	Hydroxy furoic acid
$C_2H_2O_4$	0.28	90.00	Oxalic acid
$C_3H_6O_3$	0.23	90.03	Lactic acid
$C_2H_4O_3$	0.14	76.02	Glycolic acid
$C_6H_{10}O_3$	0.14	130.06	Oxo-hexanoic Acid
$C_2H_4O_2$	0.14	60.02	Acetic acid
$C_3H_4O_4$	0.14	104.01	Malonic acid
$C_5H_8O_3$	0.13	116.05	Oxo-pentatonic acid
$C_3H_4O_3$	0.11	88.02	Pyruvic acid
$C_5H_8O_6$	0.088	164.03	Dihydroxy glutaric acid
$C_6H_{10}O_5$	0.085	162.05	Hydroxy adipic acid
$C_6H_{12}O_3$	0.084	132.08	Hydroxy hexanoic acid
$C_4H_6O_4$	0.081	118.03	Succinic acid
$C_6H_{10}O_4$	0.062	146.06	Adipic acid
$C_5H_8O_4$	0.060	132.04	Glutaric acid
$C_3H_8O_3$	0.051	92.05	Glycerol
$C_3H_6O_4$	0.043	106.03	Glyceric acid
$C_5H_{10}O_3$	0.036	118.06	Hydroxy valeric acid
$C_5H_6O_5$	0.036	146.02	Ketoglutaric acid
$C_9H_{16}O_4$	0.035	188.10	Azelaic acid

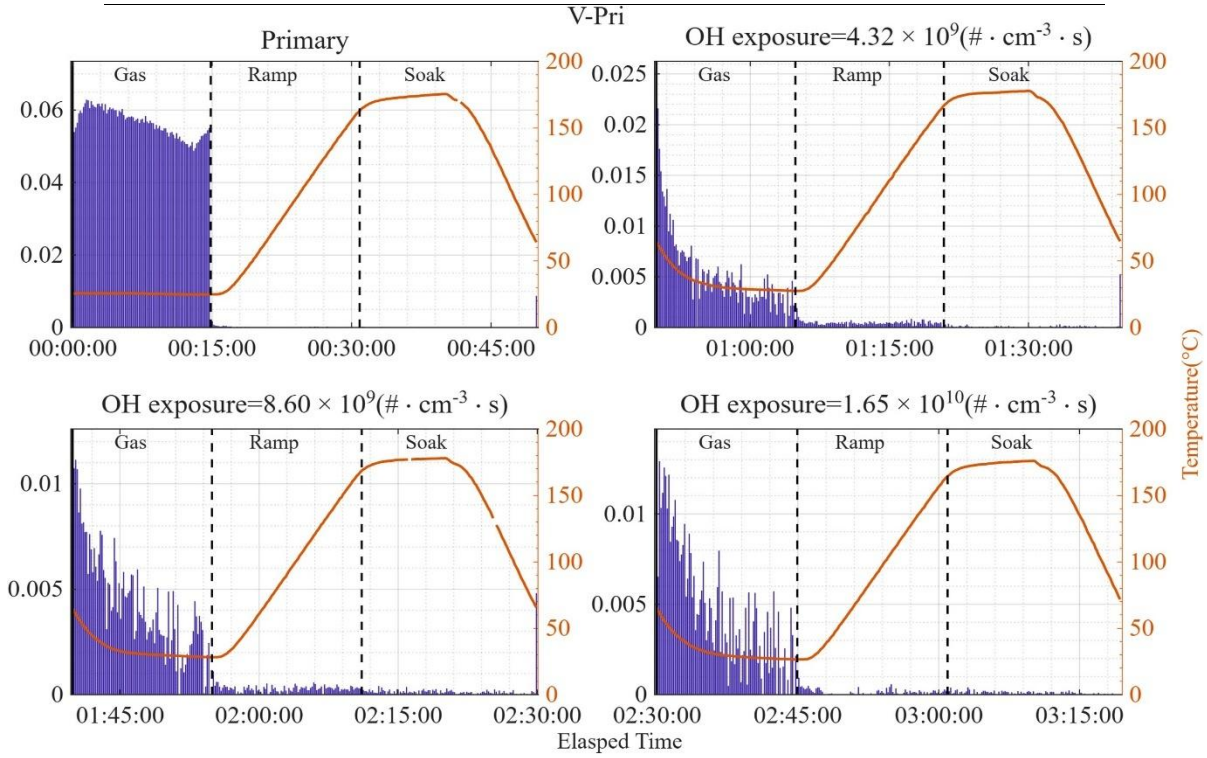

Figure S23 Intensity time series of volatile primary emission factor V-Pri (presented remarkably only in gas phase) in PMF results at different OH exposure during FIGAERO measurement circles.

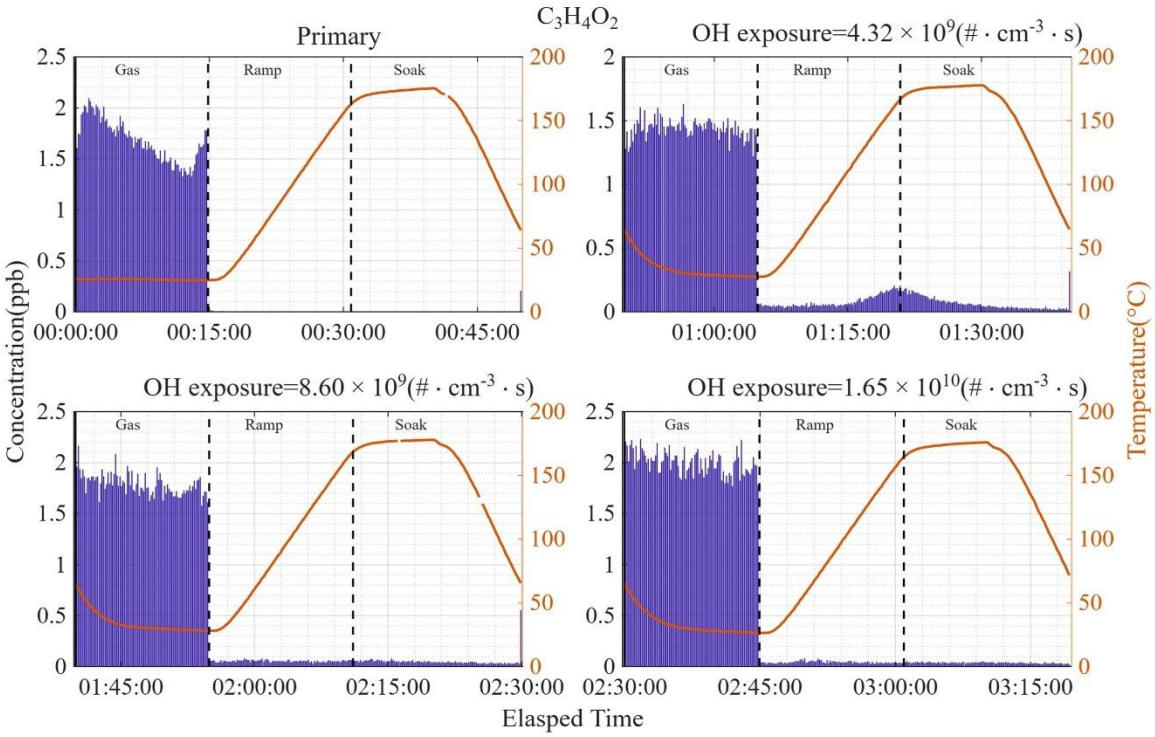

Figure S24 Concentration time series of compound with elemental composition of $C_3H_4O_2$ (probably acrylic acid, representing volatile primary organics from thermal decomposition of glycerol) at different OH exposure during FIGAERO measurement of flow tube experiment.

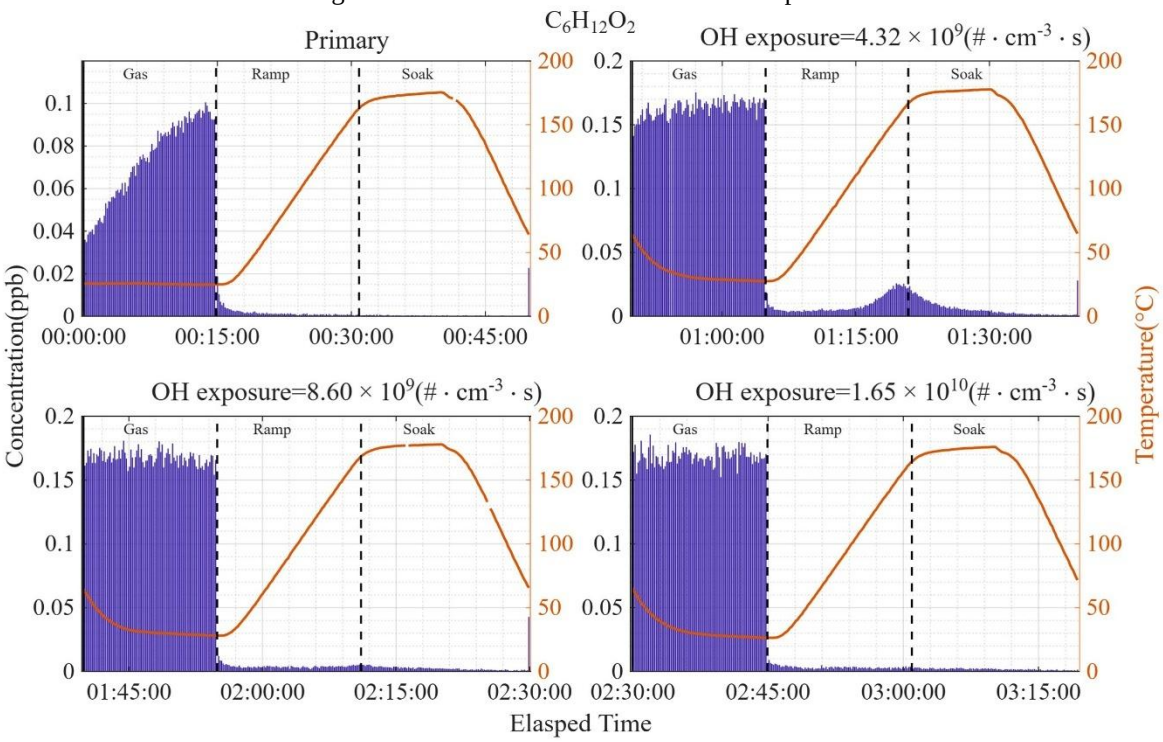

Figure S25 Concentration time series of compound with elemental composition of $C_6H_{12}O_2$ (probably hexanoic acid, representing volatile primary organics majority from thermal oxidation of primary long-chain aliphatic acids, minority from photo-oxidation) at different OH exposure during FIGAERO measurement of flow tube experiment.

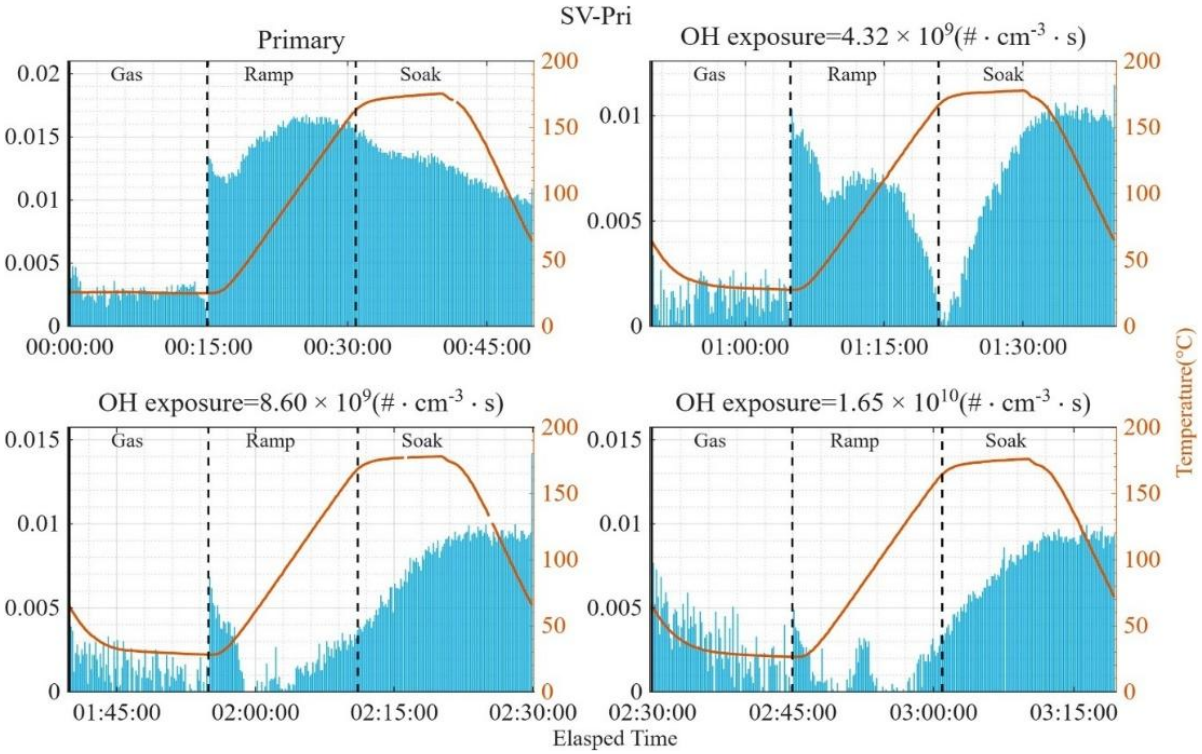

Figure S26 Intensity time series of semi-volatile primary emission factor SV-Pri (presented remarkably in both gas phase and aerosol phase) in PMF results at different OH exposure during FIGAERO measurement circles.

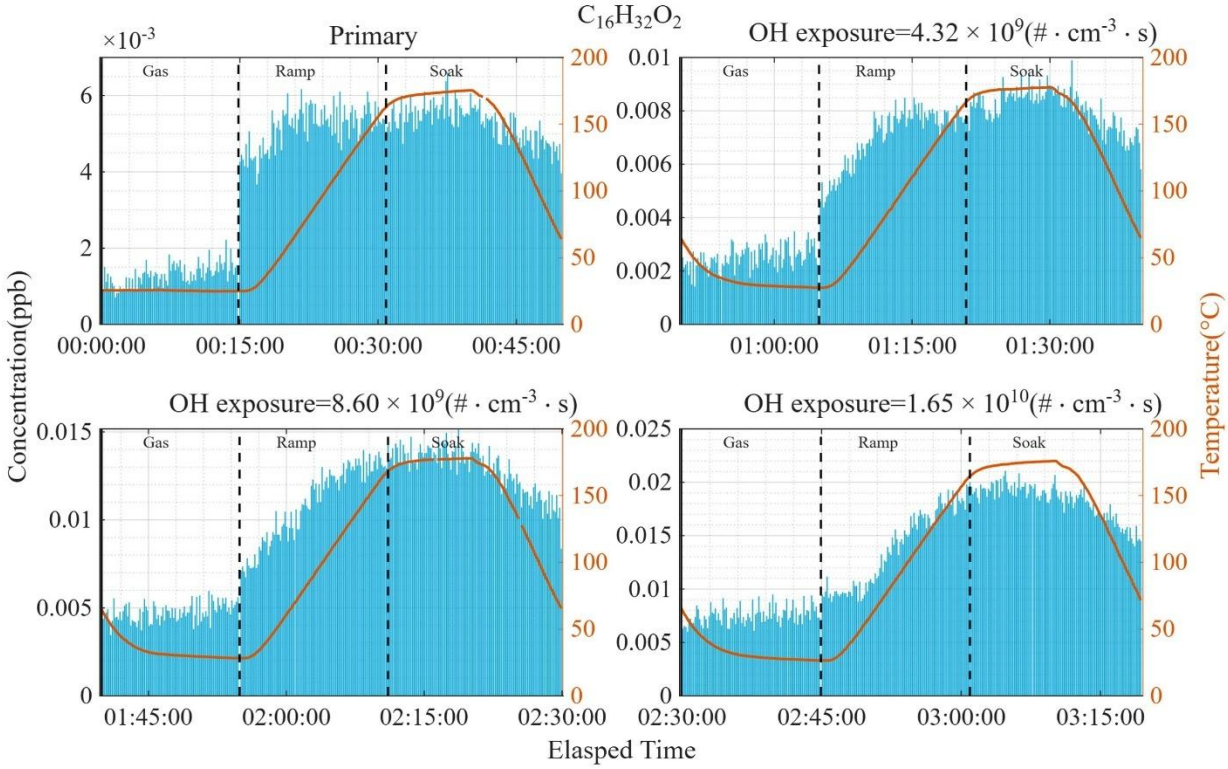

Figure S27 Concentration time series of compound with elemental composition of $C_{16}H_{32}O_2$ (probably Palmitic acid, representing long-chain saturated carboxylic acids as semi-volatile primary markers of cooking emission) at different OH exposure during FIGAERO measurement of flow tube experiment.

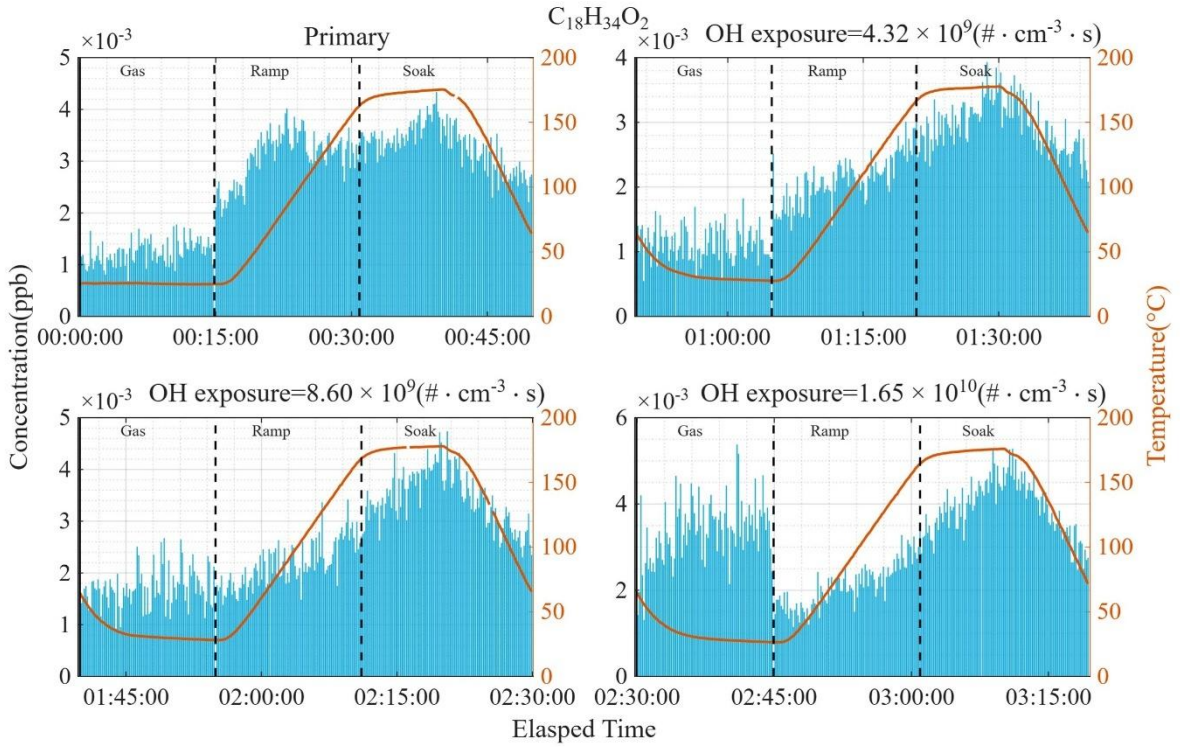

Figure S28 Concentration time series of compound with elemental composition of $C_{18}H_{34}O_2$ (probably Oleic acid, representing long-chain unsaturated acids as semi-volatile primary markers of cooking emission) at different OH exposure during FIGAERO measurement of flow tube experiment.

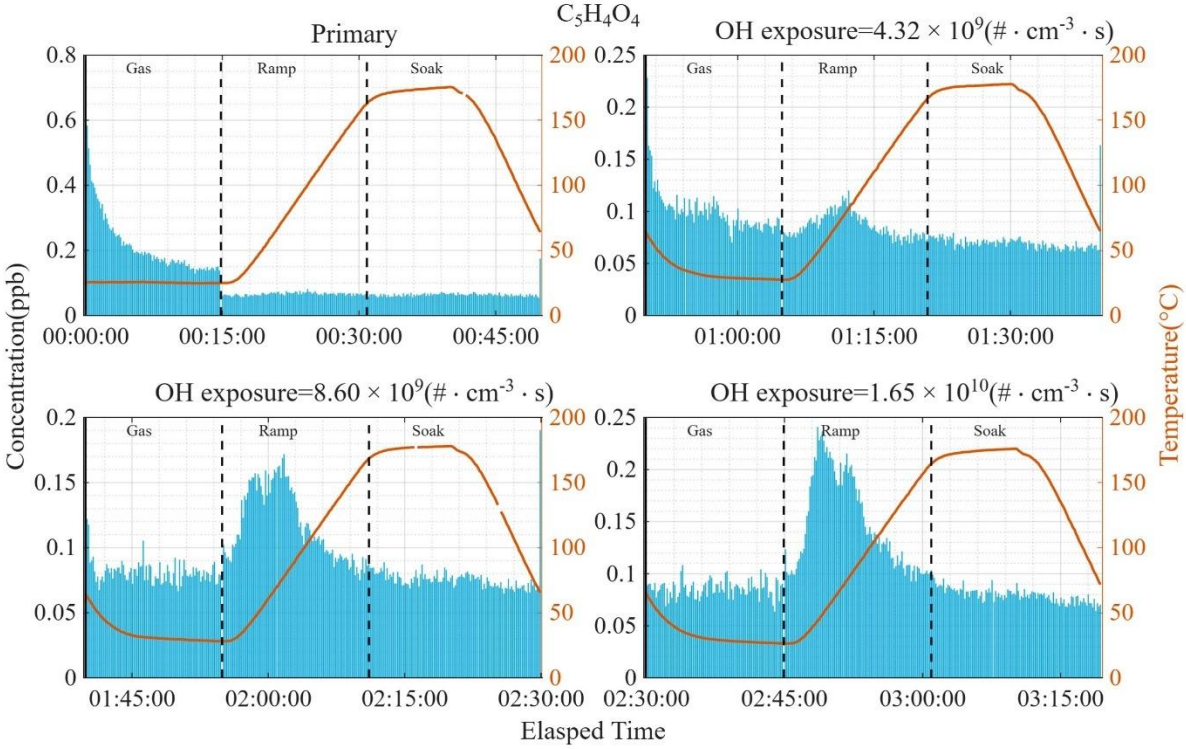

Figure S29 Concentration time series of compound with elemental composition of $C_5H_4O_4$ (possibly aconic acid or hydroxy furoic acid, representing primary emissions from thermal oxidation and decomposition) at different OH exposure during FIGAERO measurement of flow tube experiment.

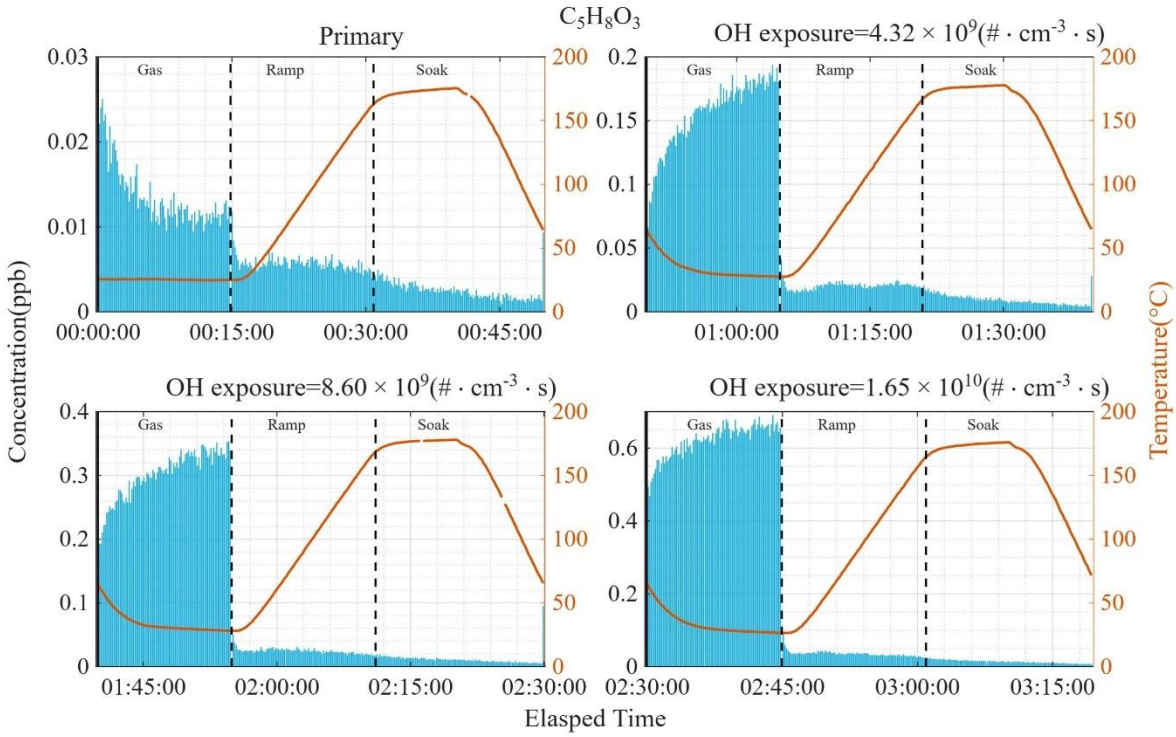

Figure S30 Concentration time series of compound with elemental composition of $C_5H_8O_3$ (possibly oxo-pentatonic acids) at different OH exposure during FIGAERO measurement of flow tube experiment.

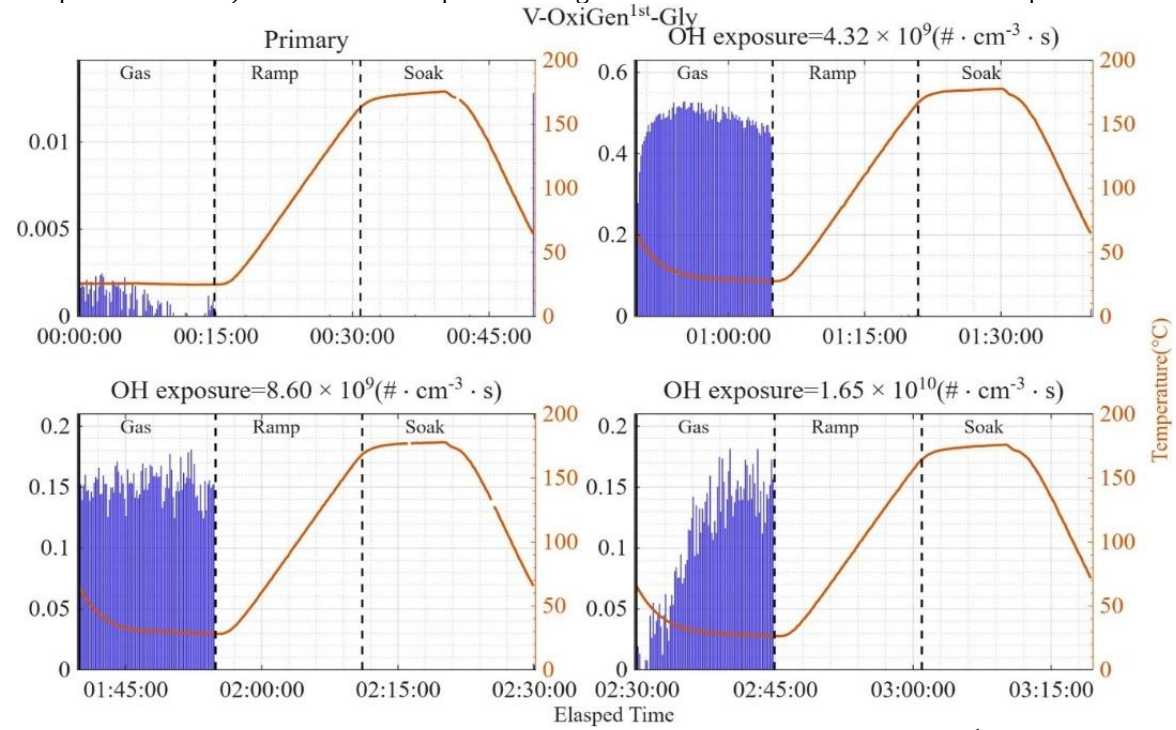

Figure S31 Intensity time series of volatile intermediate oxidative state factor V-OxiGen^{1st}-Gly (presented remarkably only in gas phase, possibly related to oxidation of glycerol-structure compounds) in PMF results at different OH exposure during FIGAERO measurement circles.

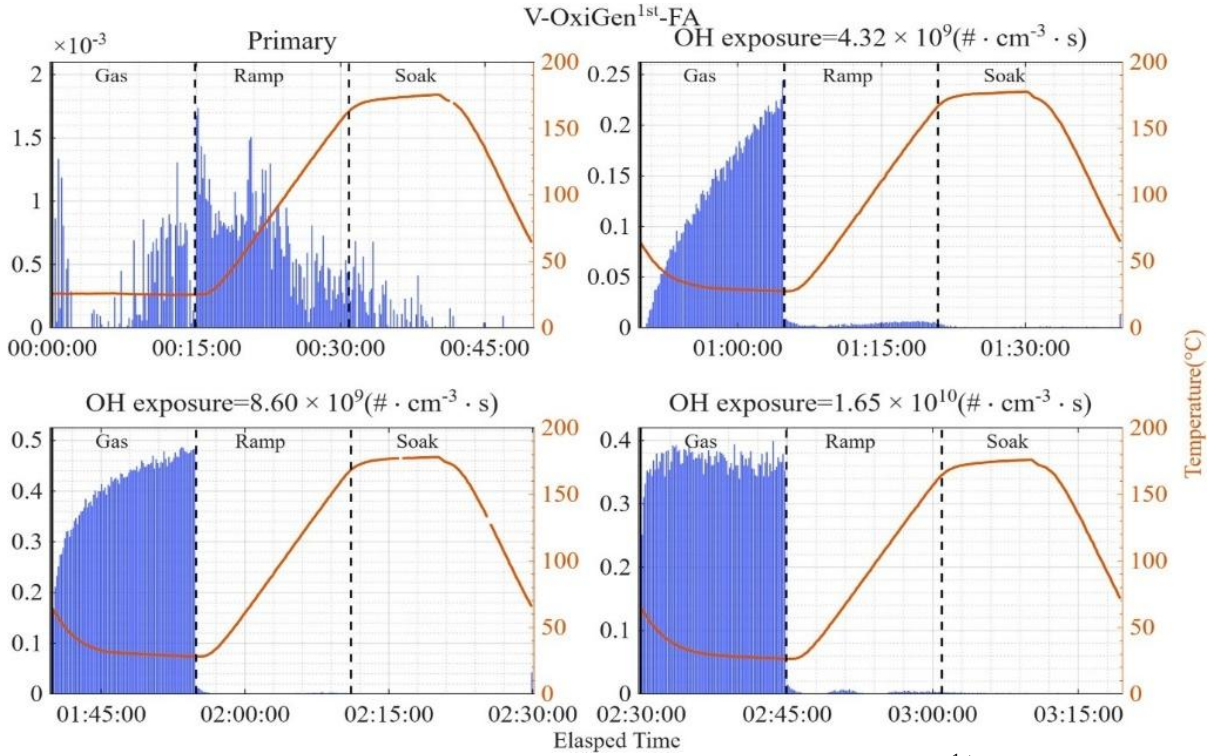

Figure S32 Intensity time series of volatile intermediate oxidative state factor V-OxiGen[1st]-FA (abundant most in gas phase, possibly related to oxidation of long-chain-fatty-acid-structure compounds) in PMF results at different OH exposure during FIGAERO measurement circles.

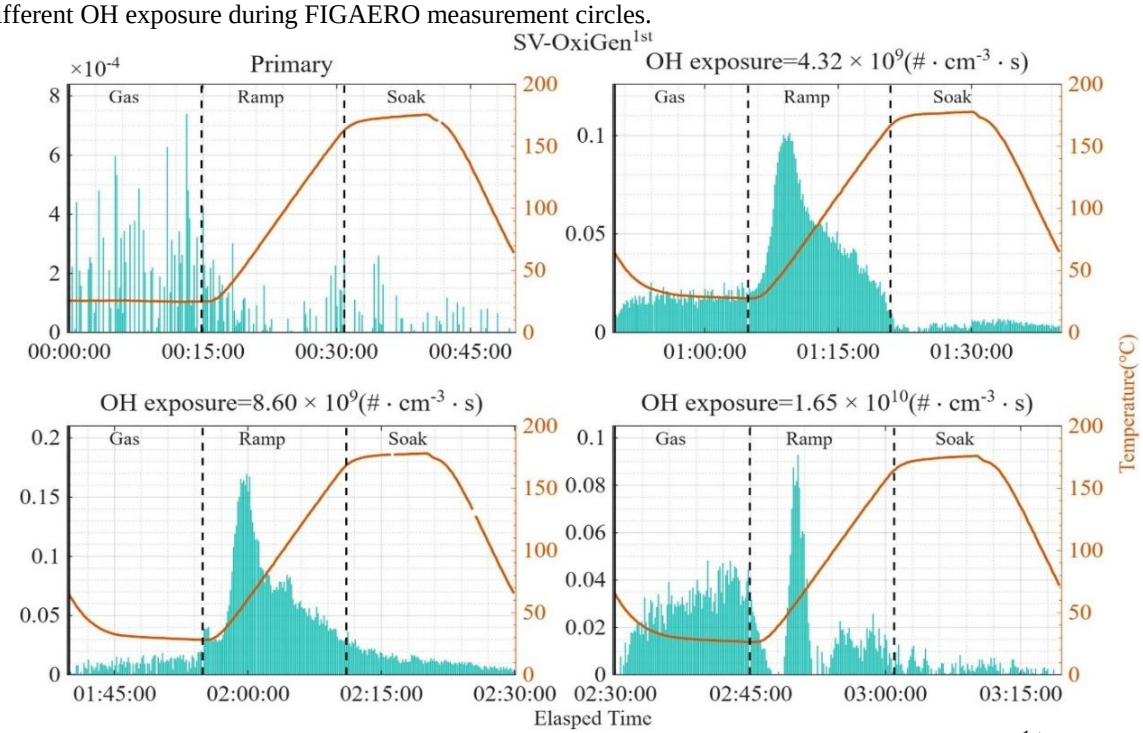

Figure S33 Intensity time series of semi-volatile intermediate oxidative state factor SV-OxiGen[1st] (abundant both in gas phase and aerosol phase) in PMF results at different OH exposure during FIGAERO measurement circles.

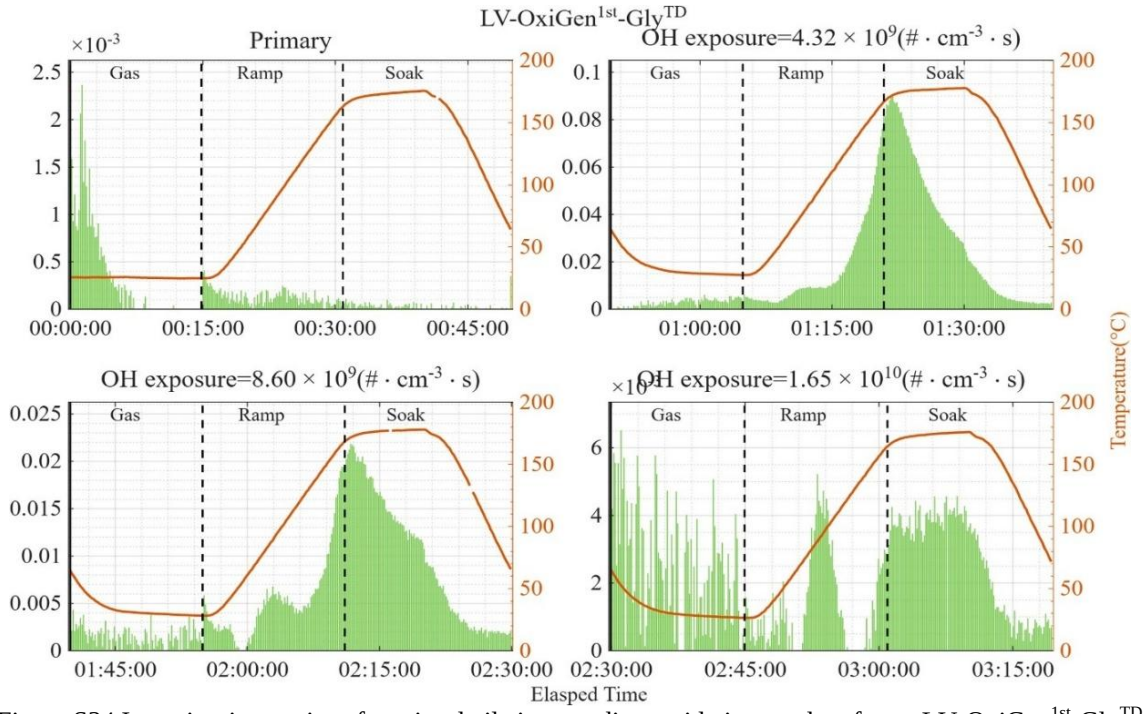

Figure S34 Intensity time series of semi-volatile intermediate oxidation product factor LV-OxiGen[1st]-Gly[TD] (abundant most in aerosol phase) in PMF results at different OH exposure during FIGAERO measurement circles.

Table S10 Average composition and top-20 most abundant species in factor V-OxiGen[1st]-Gly from ME-2 PMF results

Factor Name: V-OxiGen[1st]-Gly			
Average elemental composition: $C_{4.68}H_{7.92}O_{3.81}N_{0.03}S_{0.05}$ MW=126.87 OS_C=0.405			
Molecular composition:			
Molecules	MW(g·mol^{-1})	Relative Intensity	Possible species
$C_2H_4O_4$	92.01096	0.69566	Hydroperoxy acetic acid
$C_3H_4O_4$	104.011	0.291804	Malonic acid
$C_7H_{12}O_4$	160.0736	0.237051	Pimelic acid
$C_3H_4O_3$	88.0155	0.224047	Pyruvic acid
$C_2H_2O_4$	89.99531	0.21201	Oxalic acid
$C_2H_4O_2$	60.02113	0.201705	Acetic acid
$C_7H_{12}O_5$	176.0685	0.18606	Hydroxy pimelic acid
$C_6H_{10}O_3$	130.063	0.171717	Oxo-hexanoic Acid
$C_7H_{14}O_4$	162.0887	0.152692	Dihydroxy heptanoic acid
$C_6H_{10}O_4$	146.0579	0.147952	Adipic acid
$C_6H_{12}O_3$	132.0786	0.141303	Hydroxy hexanoic Acid
$C_3H_4O_2$	72.02113	0.136328	Acrylic acid
$C_4H_4O_3$	100.016	0.128605	Oxo-butenoic acid
$C_3H_6O_4$	106.0266	0.116571	Glyceric acid
$C_6H_{12}O_4$	148.0736	0.09489	Dihydroxy hexanoic Acid
CH_2O_3	61.99985	0.065981	-
$C_4H_6O_5$	134.021	0.063952	Malic acid
$C_5H_8O_3$	116.0468	0.061708	Oxo-pentatonic acid
$C_3H_6S_2$	105.9911	0.060226	-
$C_5H_6O_5$	146.0215	0.056191	Oxo glutaric acid

Table S11 Composition profile and top-20 most abundant species in factor V-OxiGen^{1st}-FA from ME-2 PMF results

Factor Name: V-OxiGen^{1st}-FA			
Average elemental composition: $C_{6.49}H_{10.94}O_{3.96}N_{0.01}S_{0.01}$ MW=152.86 OS_C=-0.281			
Molecular composition:			
Molecules	MW(g·mol^{-1})	Relative Intensity	Possible species
$C_6H_{12}O_3$	132.0786	0.516467	Hydroxy hexanoic Acid
$C_6H_{10}O_3$	130.063	0.400322	Oxo-hexanoic Acid
$C_7H_{12}O_5$	176.0685	0.337381	Hydroxy pimelic acid
$C_4H_4O_3$	100.016	0.28861	Oxo-butenoic acid
$C_6H_{10}O_4$	146.0579	0.232466	Adipic acid
$C_2H_4O_2$	60.02113	0.19557	Acetic acid
$C_3H_4O_4$	104.011	0.191313	Malonic acid
$C_7H_{12}O_4$	160.0736	0.182699	Pimelic acid
$C_3H_4O_3$	88.0155	0.177969	Pyruvic acid
$C_7H_{14}O_5$	178.0841	0.132052	Hydroxy hydroperoxyl heptanoic acid
$C_{10}H_{16}O_3$	184.1099	0.128191	Oxo-decanoic acid
$C_9H_{16}O_4$	188.1049	0.113297	Azelaic acid
$C_6H_{12}O_4$	148.0736	0.109202	Dihydroxy hexanoic Acid
$C_7H_{12}O_6$	192.0634	0.109095	Hydroperoxy pimelic acid
$C_3H_4O_2$	72.02113	0.108079	Acrylic acid
$C_5H_8O_3$	116.0468	0.099506	Oxo-pentatonic acid
$C_5H_6O_5$	146.0215	0.095848	Oxo glutaric acid
$C_7H_{12}O_3$	144.0786	0.074596	Hydroxy heptanoic acid
$C_5H_{10}O_3$	118.0624	0.069336	2-Oxo-Pentanoic acid
$C_{10}H_{16}O_6$	232.0941	0.060075	Decanetrioic acid

Table S12 Composition profile and top-20 most abundant species in factor SV-OxiGen^{1st} from ME-2 PMF results

Factor Name: SV-OxiGen^{1st}			
Average elemental composition: $C_{7.69}H_{13.72}O_{3.88}N_{0.00}S_{0.00}$ MW=168.29 OS_C=-0.662			
Molecular composition:			
Molecules	MW(g·mol^{-1})	Relative Intensity	Possible species
$C_9H_{16}O_4$	188.1049	0.505217	Azelaic acid
$C_9H_{18}O_4$	190.1205	0.44474	Hydroperoxyl nonanoic acid
$C_6H_{12}O_4$	148.0736	0.404834	Hydroperoxyl hexanoic acid
$C_{10}H_{18}O_4$	202.1205	0.394289	Sebacic acid
$C_6H_{12}O_3$	132.0786	0.209654	Hydroxyl hexanoic acid
$C_6H_{10}O_4$	146.0579	0.162467	Adipic acid
$C_{10}H_{16}O_3$	184.1099	0.147793	Oxo-decanoic acid
$C_3H_4O_3$	88.0155	0.137486	Pyruvic acid
$C_7H_{12}O_4$	160.0736	0.13194	Pimelic acid
$C_6H_{10}O_3$	130.063	0.129637	Oxo-hexanoic Acid
$C_9H_{14}O_4$	186.0892	0.121187	Nonendioic acid
$C_9H_{16}O_5$	204.0998	0.100231	Hydroxy azelaic acid
$C_{10}H_{18}O_3$	186.1256	0.089287	Oxodecanoic acid
$C_{10}H_{16}O_4$	200.1049	0.073579	Decendioic acid

$C_9H_{16}O_3$	172.1099	0.066601	Oxo-nonanoic acid
$C_7H_{12}O_5$	176.0685	0.063406	Hydroxy pimelic acid
$C_3H_4O_4$	104.011	0.060367	Malonic acid
$C_4H_4O_3$	100.016	0.054027	Oxo-butenoic acid
$C_7H_{14}O_5$	178.0841	0.049281	Hydroxy hydroperoxyl heptanoic acid
$C_8H_{18}O_4$	178.1205	0.048359	Hydroperoxy Octanediol

Table S13 Composition profile and top-20 most abundant species in factor LV-OxiGen^{1st}-Gly^{TD} from ME-2 PMF results

Factor Name: LV-OxiGen^{1st}-Gly^{TD}			
Average elemental composition: $C_{4.67}H_{7.37}O_{3.50}N_{0.00}S_{0.00}$ MW=119.59 OS_C=0.300			
Molecular composition:			
Molecules	MW(g·mol^{-1})	Relative Intensity	Possible species
$C_3H_4O_3$	88.0155	0.920802	Pyruvic acid
$C_3H_4O_4$	104.011	0.329353	Malonic acid
$C_9H_{16}O_5$	204.0998	0.1666	Hydroxy azelaic acid
$C_6H_{12}O_3$	132.0786	0.062601	Hydroxy hexanoic acid
$C_9H_{16}O_4$	188.1049	0.049186	Azelaic acid
$C_6H_{10}O_4$	146.0579	0.039255	Adipic acid
$C_3H_4O_2$	72.02113	0.034696	Acrylic acid
$C_{10}H_{16}O_3$	184.1099	0.03121	Oxo-decanoic acid
$C_6H_{10}O_3$	130.063	0.028194	Oxo-hexanoic Acid
$C_9H_{18}O_4$	190.1205	0.026098	Hydroperoxyl nonanoic acid
$C_{10}H_{18}O_4$	202.1205	0.024655	Sebacic acid
$C_7H_{12}O_4$	160.0736	0.023498	Pimelic acid
$C_5H_4O_4$	128.011	0.021765	Hydroxy furoic acid
$C_6H_{12}O_4$	148.0736	0.021387	Dihydroxy hexanoic Acid
$C_2H_4O_2$	60.02113	0.016833	Acetic acid
$C_9H_{14}O_4$	186.0892	0.015728	Nonendioic acid
$C_5H_8O_3$	116.0468	0.014809	Oxo-pentanoic acid
$C_4H_4O_3$	100.016	0.013434	Oxo-butenoic acid
$C_9H_{16}O_3$	172.1099	0.013015	Oxo-nonanoic acid
$C_{10}H_{18}O_3$	186.1256	0.011866	Oxo-decanoic acid

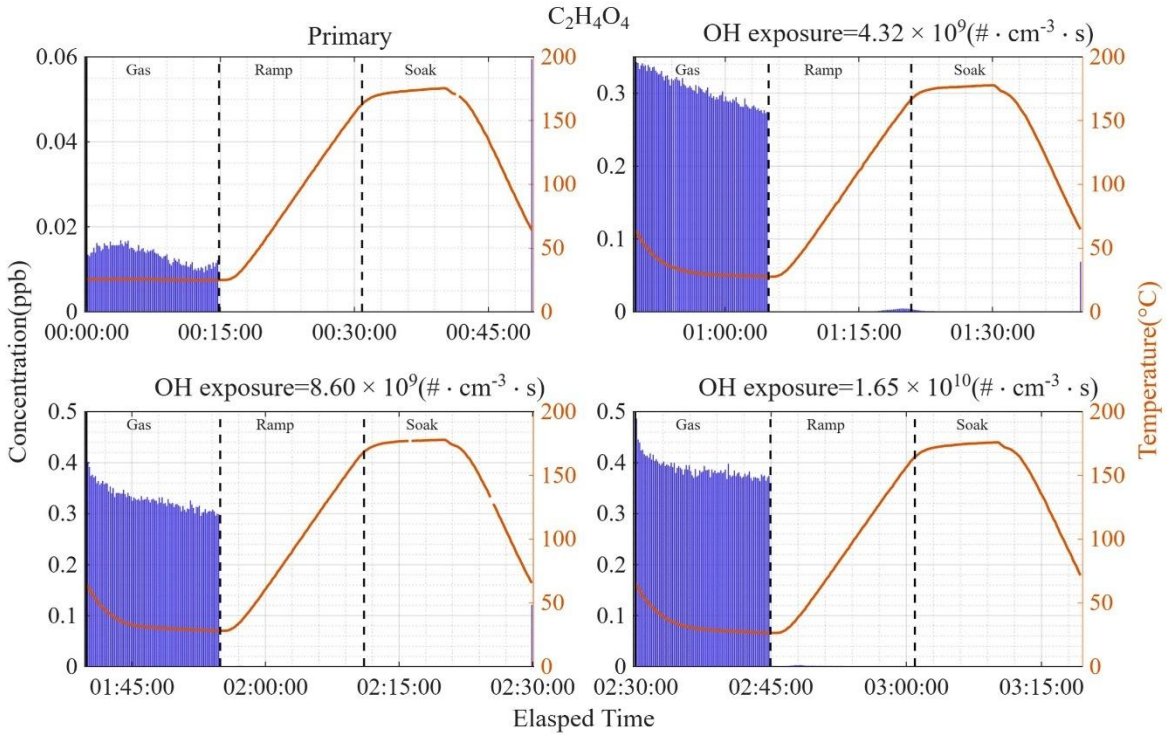

Figure S35 Concentration time series of compound with elemental composition of $C_2H_4O_4$ (possibly hydroperoxyl acetic acid) at different OH exposure during FIGAERO measurement of flow tube experiment.

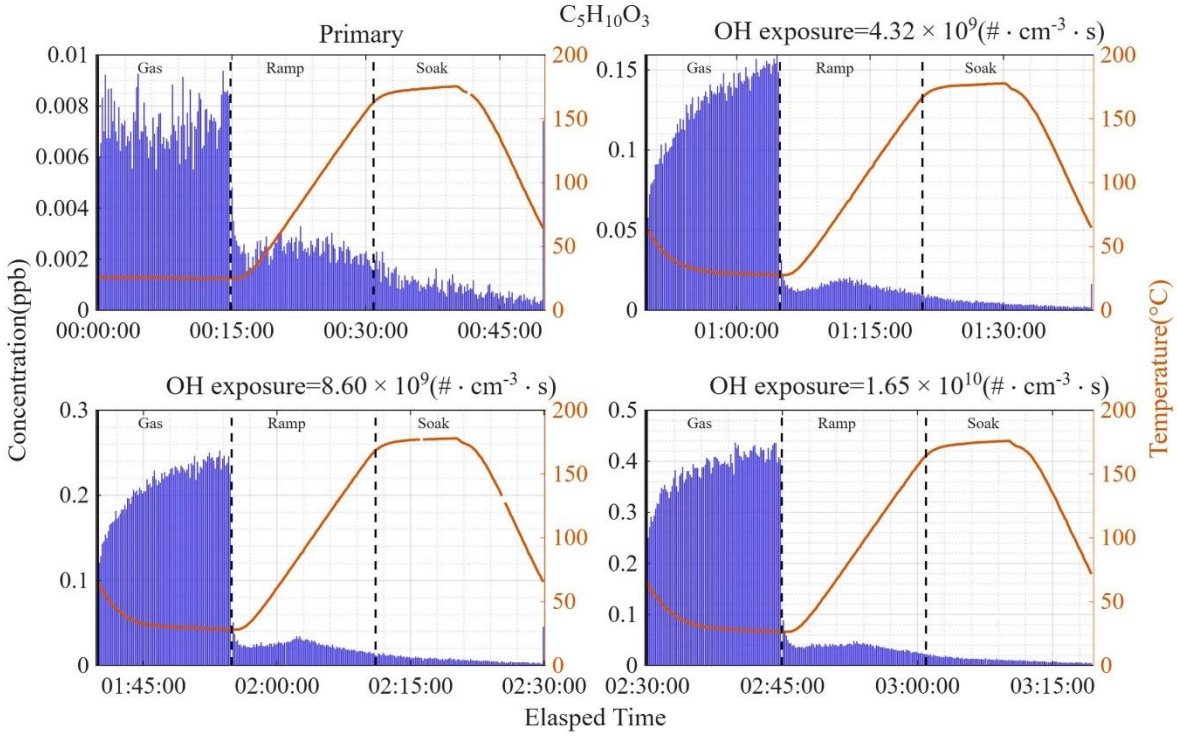

Figure S36 Concentration time series of compound with elemental composition of $C_5H_{10}O_3$ (possibly oxo-pentatonic acids) at different OH exposure during FIGAERO measurement of flow tube experiment.

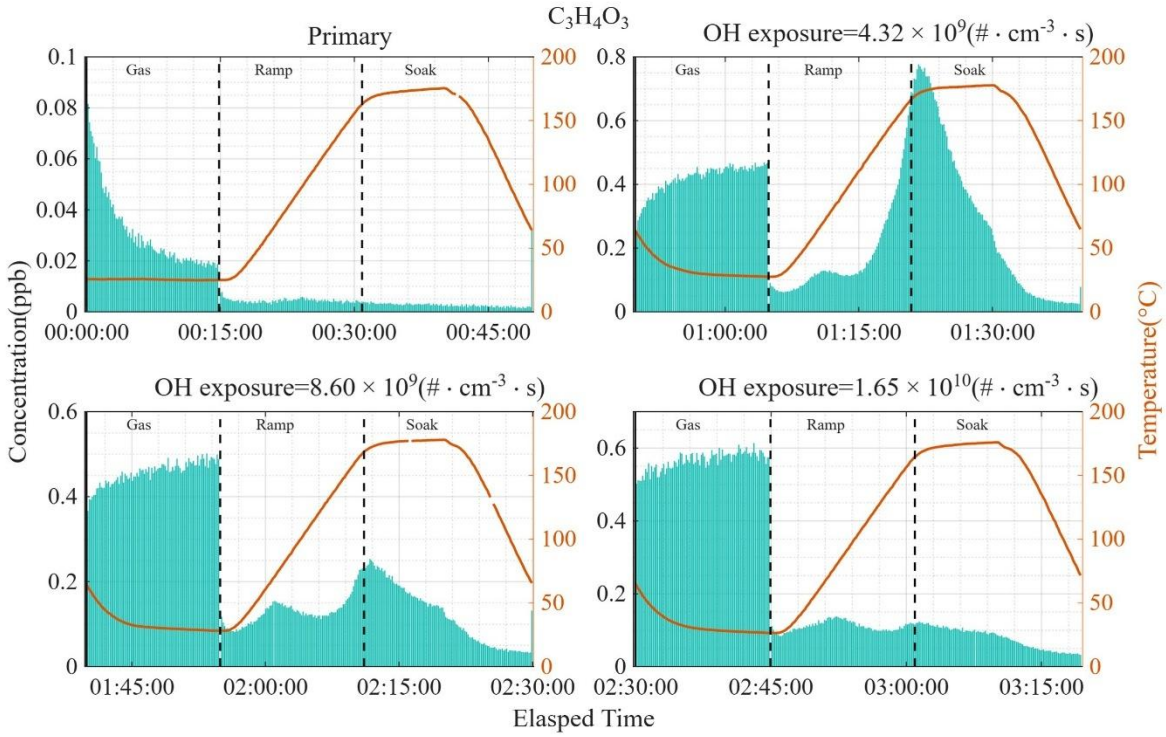

Figure S37 Concentration time series of compound with elemental composition of $C_3H_4O_3$ (probably pyruvic acid) at different OH exposure during FIGAERO measurement of flow tube experiment.

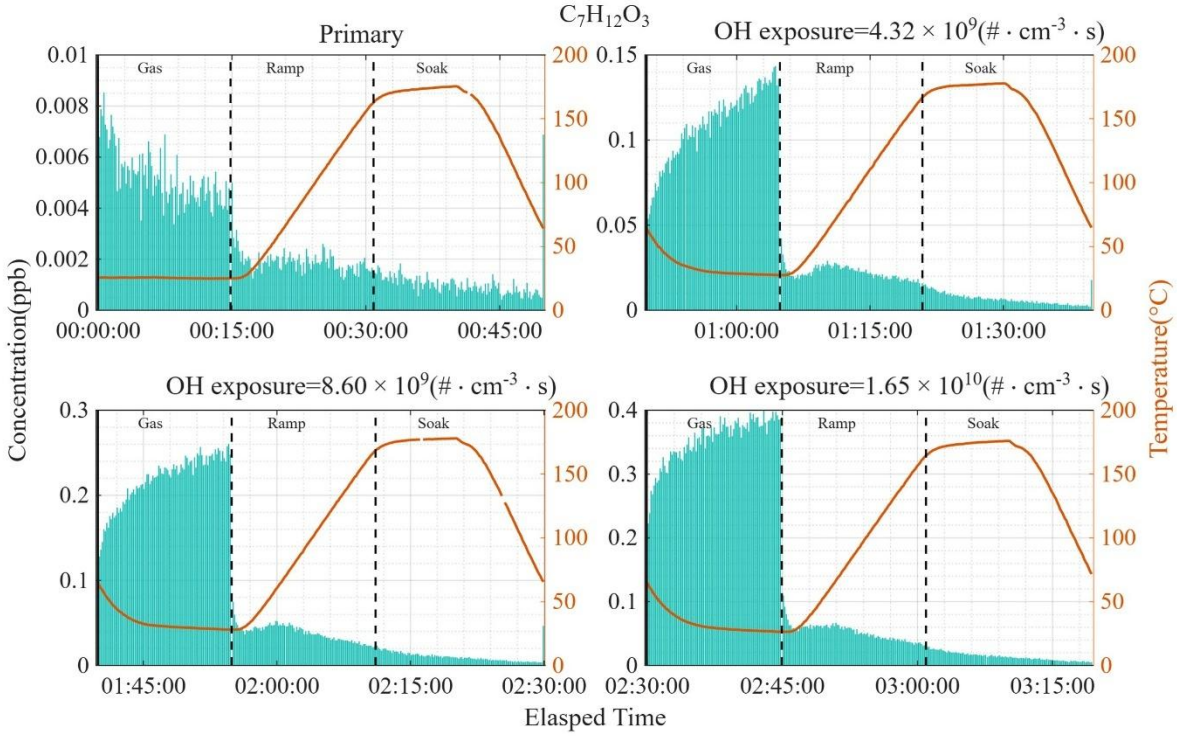

Figure S38 Concentration time series of compound with elemental composition of $C_7H_{12}O_3$ (possibly hydroxy heptanoic acid) at different OH exposure during FIGAERO measurement of flow tube experiment.

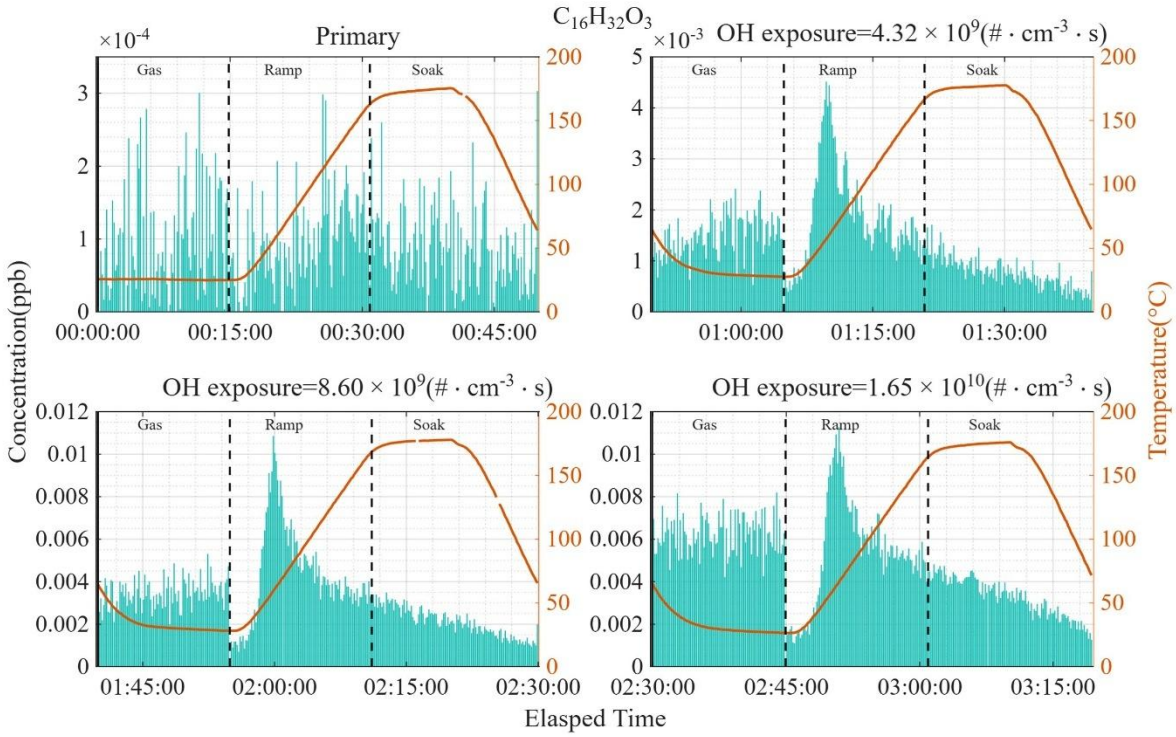

Figure S39 Concentration time series of compound with elemental composition of $C_{16}H_{32}O_3$ (probably hydroxy palmitic acid) at different OH exposure during FIGAERO measurement of flow tube experiment.

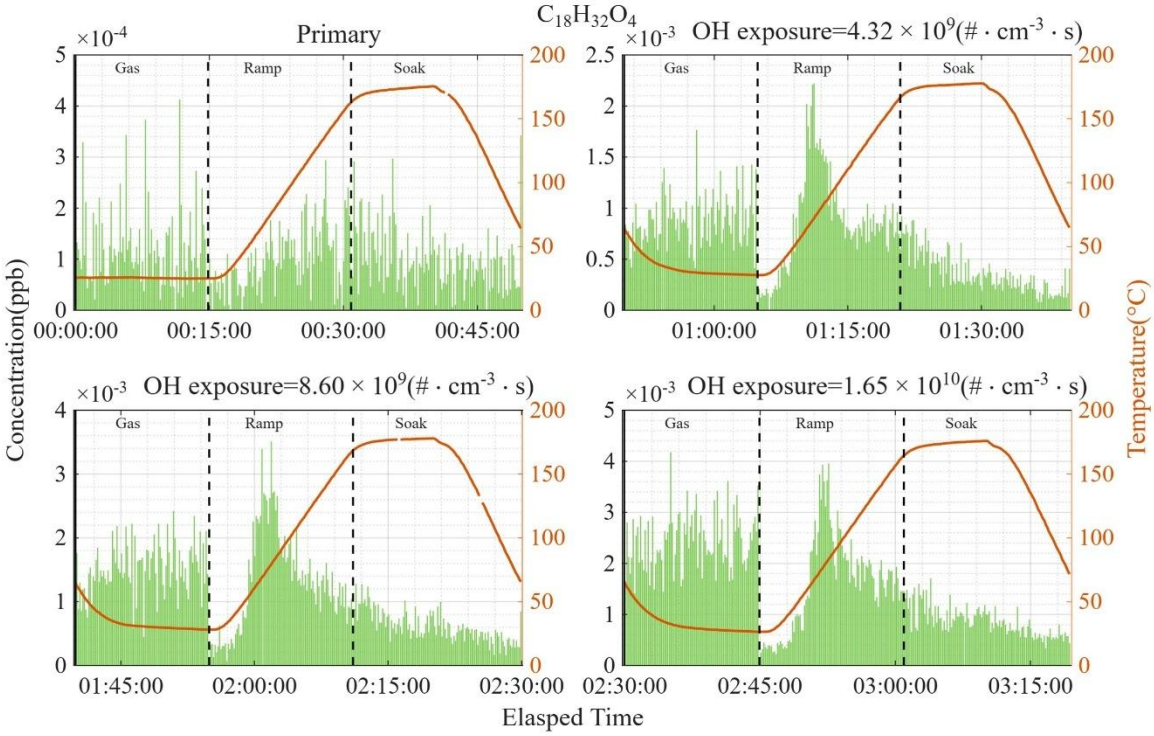

Figure S40 Concentration time series of compound with elemental composition of $C_{18}H_{32}O_4$ at different OH exposure during FIGAERO measurement of flow tube experiment.

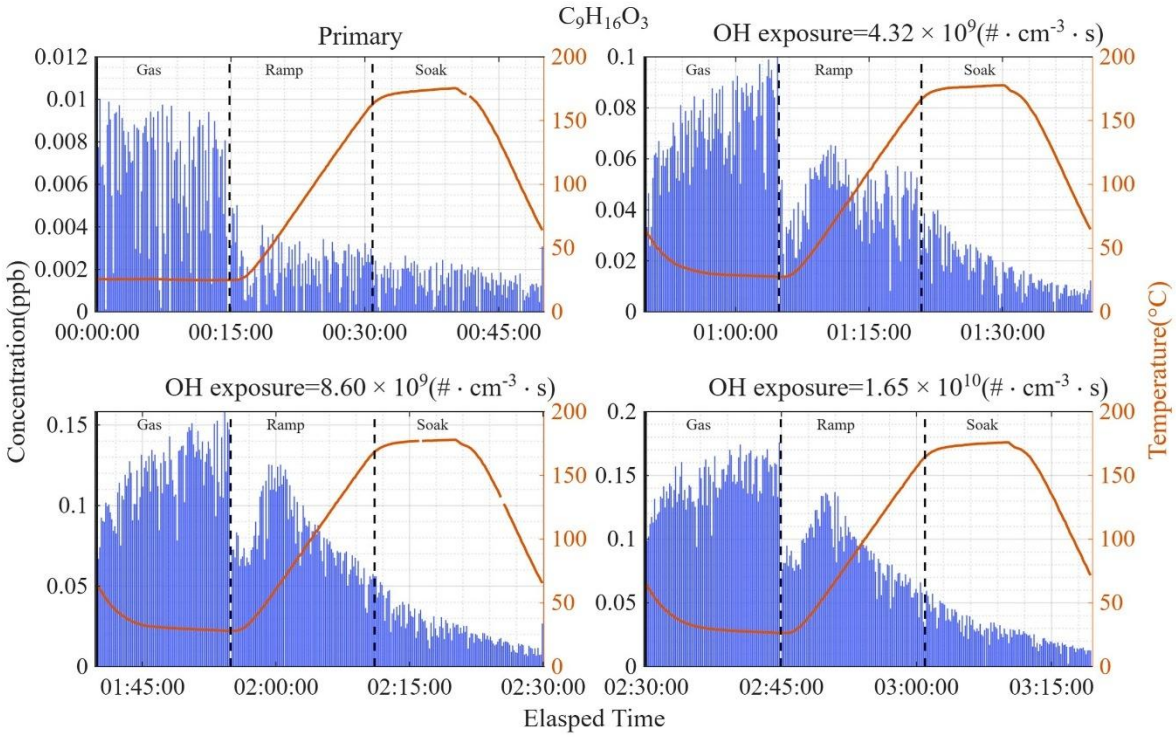

Figure S41 Concentration time series of compound with elemental composition of $C_9H_{16}O_3$ (possibly oxo-nonanoic acids) at different OH exposure during FIGAERO measurement of flow tube experiment.

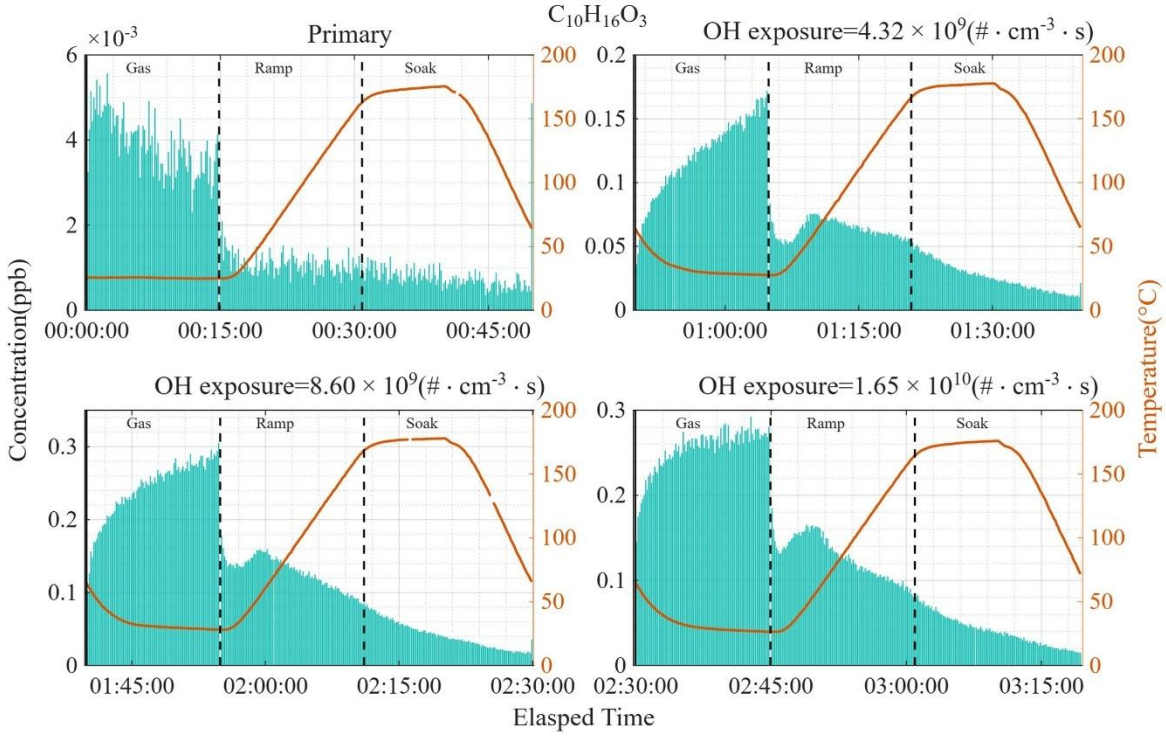

Figure S42 Concentration time series of compound with elemental composition of $C_{10}H_{16}O_3$ (possibly oxo-decenenoic acids) at different OH exposure during FIGAERO measurement of flow tube experiment.

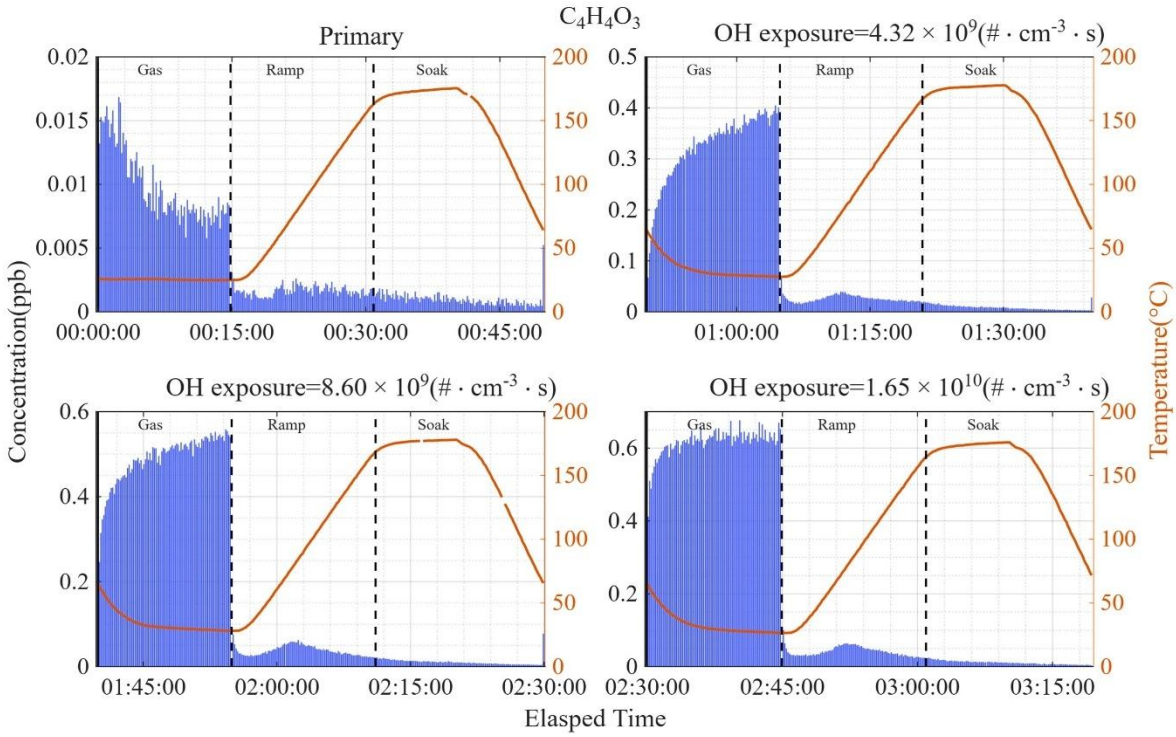

Figure S43 Concentration time series of compound with elemental composition of $C_4H_4O_3$ (possibly oxo-butenoic acids) at different OH exposure during FIGAERO measurement of flow tube experiment.

Table S14 Composition profile and top-20 most abundant species in V-MultiGen-Gly from ME-2 PMF results

Factor Name: V-MultiGen-Gly			
Average elemental composition: $C_{4.84}H_{8.22}O_{3.88}N_{0.03}S_{0.10}$ MW=131.97 OS_C=0.437			
Molecular composition:			
Molecules	MW(g·mol^{-1})	Relative Intensity	Possible species
$C_2H_4O_4$	92.01	0.72	Hydroperoxyl acetic acid
$C_3H_4O_4$	104.01	0.35	Malonic acid
$C_2H_2O_4$	89.99	0.22	Oxalic acid
$C_7H_{12}O_4$	160.07	0.22	Pimelic acid
$C_7H_{14}O_4$	162.09	0.21	Dihydroxy heptanoic acid
$C_7H_{12}O_5$	176.07	0.18	Hydroxy pimelic acid
$C_6H_{10}O_4$	146.06	0.15	Adipic acid
$C_2H_4O_2$	60.02	0.15	Acetic acid
$C_2H_6S_2$	93.99	0.14	-
$C_3H_6O_4$	106.03	0.13	Glyceric acid
$C_3H_4O_2$	72.02	0.11	Acrylic acid
$C_3H_4O_3$	88.01	0.11	Pyruvic acid
$C_3H_6S_2$	105.99	0.10	-
CH_2O_3	62.00	0.091	-
$C_9H_{16}O_4$	188.10	0.089	Azelaic acid
$C_6H_{12}O_4$	148.07	0.086	Dihydroxy hexanoic Acid
$C_{10}H_{18}O_4$	202.12	0.070	Sebacic acid
$C_6H_{10}O_3$	130.06	0.069	Oxo-hexanoic Acid
$C_7H_{12}O_6$	192.06	0.058	Hydroperoxyl pimelic acid
$C_4H_6O_5$	134.02	0.057	Malic acid

Table S15 Composition profile and top-20 most abundant species in Factor V-MultiGen-FA from ME-2 PMF results

Factor Name: V-MultiGen-FA			
Average elemental composition: $C_{6.43}H_{10.62}O_{4.40}N_{0.02}S_{0.06}$ MW=160.40 OS_C=-0.035			
Molecular composition:			
Molecules	MW($g \cdot mol^{-1}$)	Relative Intensity	Possible species
$C_3H_4O_4$	104.01	0.40	Malonic acid
$C_7H_{12}O_5$	176.07	0.37	Hydroxy pimelic acid
$C_6H_{10}O_4$	146.06	0.32	Adipic acid
$C_6H_{10}O_3$	130.06	0.26	Oxo-hexanoic Acid
$C_6H_{12}O_3$	132.08	0.26	Hydroxy hexanoic acid
$C_2H_4O_2$	60.02	0.22	Acetic acid
$C_7H_{12}O_6$	192.06	0.20	Hydroperoxyl pimelic acid
$C_7H_{14}O_4$	162.09	0.18	Hydroperoxyl heptanoic acid
$C_7H_{12}O_4$	160.07	0.18	Pimelic acid
$C_6H_{12}O_4$	148.07	0.17	Dihydroxy hexanoic Acid
$C_5H_8O_3$	116.05	0.15	Oxo-pentanoic acid
$C_7H_{10}O_6$	190.05	0.15	Hydroxy oxo-pimelic acid
$C_3H_6O_4$	106.03	0.14	Glyceric acid
$C_2H_2O_4$	90.00	0.13	Oxalic acid
$C_4H_6O_4$	118.02	0.12	Succinic acid
$C_2H_4O_4$	92.01	0.11	Hydroperoxyl acetic acid
$C_2H_6S_2$	93.99	0.11	-
$C_8H_{14}O_6$	206.08	0.11	Dihydroxy suberic acid
$C_7H_{14}O_5$	178.08	0.097	Hydroxy hydroperoxy pentanoic acid
$C_{10}H_{16}O_6$	232.09	0.095	Decanetrioic acid

Table S16 Composition profile and top-20 most abundant species in Factor SV3 from ME-2 PMF results

Factor Name: SV-Multigen-peroxy			
Average elemental composition: $C_{7.75}H_{13.32}O_{4.49}N_{0.00}S_{0.01}$ MW=178.52 OS_C=-0.362			
Molecular composition:			
Molecules	MW($g \cdot mol^{-1}$)	Relative Intensity	Possible species
$C_3H_4O_4$	104.01	0.47	Malonic acid
$C_9H_{16}O_4$	188.10	0.36	Azelaic acid
$C_{10}H_{18}O_4$	202.12	0.34	Sebacic acid
$C_9H_{18}O_4$	190.12	0.29	Hydroperoxyl nonanoic acid
$C_6H_{12}O_4$	148.07	0.26	Dihydroxy hexanoic acid
$C_7H_{14}O_4$	162.09	0.25	Hydroperoxyl heptanoic acid
$C_9H_{16}O_5$	204.10	0.24	Hydroxy azelaic acid
$C_{10}H_{18}O_5$	218.12	0.21	Hydroxy sebacic acid
$C_7H_{14}O_5$	178.08	0.16	Hydroxy hydroperoxyl pentanoic acid
$C_9H_{18}O_5$	206.12	0.15	Hydroxy hydroperoxyl nonanoic acid
$C_7H_{12}O_5$	176.07	0.13	Hydroxy pimelic acid
$C_6H_{10}O_4$	146.06	0.11	Adipic acid
$C_{10}H_{16}O_6$	232.09	0.10	Decanetrioic acid
$C_7H_{12}O_4$	160.07	0.10	Pimelic acid
$C_9H_{14}O_6$	218.08	0.10	Hydroxy oxo-azelaic acid

$C_9H_{14}O_5$	202.08	0.10	Oxo- azelaic acid
$C_{10}H_{16}O_5$	216.10	0.10	Oxo-sebacic acid
$C_6H_{12}O_5$	164.07	0.091	Hydroxy hydroperoxyl hexanoic acid
$C_4H_6O_5$	134.02	0.083	Malic acid
$C_8H_{16}O_4$	176.10	0.073	Dihydroxy octanoic acid

Table S17 Composition profile and top-20 most abundant species in Factor LV2 from ME-2 PMF results

Factor Name: LV-Multigen-HMW

Average elemental composition:
$C_{6.99}H_{12.16}O_{4.04}N_{0.00}S_{0.00}$
MW=160.77 OSC=-0.317

Molecular composition:

Molecules	MW($g \cdot mol^{-1}$)	Relative Intensity	Possible species
$C_3H_4O_4$	104.01	0.57	Malonic acid
$C_9H_{16}O_4$	188.10	0.40	Azelaic acid
$C_7H_{14}O_4$	162.09	0.35	Hydroperoxyl heptanoic acid
$C_9H_{18}O_4$	190.12	0.29	Hydroperoxyl nonanoic acid
$C_6H_{12}O_4$	148.07	0.28	Dihydroxy hexanoic acid
$C_{10}H_{18}O_4$	202.12	0.23	Sebacic acid
$C_6H_{10}O_4$	146.06	0.19	Adipic acid
$C_7H_{12}O_4$	160.07	0.15	Pimelic acid
$C_3H_4O_3$	88.02	0.14	Pyruvic acid
$C_7H_{12}O_5$	176.07	0.11	Hydroxy pimelic acid
$C_6H_{12}O_3$	132.08	0.11	Hydroxy hexanoic acid
$C_9H_{16}O_5$	204.10	0.10	Hydroxy azelaic acid
$C_9H_{14}O_4$	186.09	0.10	Nonendioic acid
$C_{10}H_{16}O_4$	200.10	0.097	Decendioic acid
$C_8H_{16}O_4$	176.10	0.076	Hydroperoxyl octanoic acid
$C_9H_{14}O_5$	202.08	0.067	Oxo-azelaic acid
$C_2H_2O_4$	90.00	0.060	Oxalic acid
$C_{10}H_{16}O_3$	184.11	0.058	Oxo-decanoic acid
$C_{10}H_{18}O_5$	218.11	0.056	Hydroxy sebacic acid
$C_6H_{10}O_3$	130.06	0.049	Oxo-hexanoic Acid

Table S18 Composition profile and top-20 most abundant species in Factor LV3 from ME-2 PMF results

Factor Name: LV-Multigen-COOH

Average elemental composition:
$C_{7.14}H_{11.95}O_{4.11}N_{0.01}S_{0.01}$
MW=163.77 OS_C=-0.302

Molecular composition:

Molecules	MW($g \cdot mol^{-1}$)	Relative Intensity	Possible species
$C_3H_4O_4$	104.01	0.50	Malonic acid
$C_9H_{16}O_4$	188.10	0.36	Azelaic acid
$C_7H_{14}O_4$	162.09	0.36	Hydroperoxyl heptanoic acid
$C_6H_{10}O_4$	146.06	0.36	Adipic acid
$C_6H_{12}O_3$	132.08	0.34	Hydroxy hexanoic acid
$C_7H_{12}O_4$	160.07	0.25	Pimelic acid
$C_6H_{12}O_4$	148.07	0.18	Dihydroxy hexanoic acid
$C_4H_6O_4$	118.02	0.12	Succinic acid
$C_6H_{10}O_3$	130.06	0.11	Oxo-hexanoic Acid
$C_9H_{14}O_4$	186.09	0.10	Nonendioic acid

$C_3H_6O_4$	106.03	0.10	Glyceric acid
$C_7H_{12}O_5$	176.07	0.10	Hydroxy pimelic acid
$C_{10}H_{16}O_3$	184.11	0.081	Oxo-decanoic acid
$C_{10}H_{16}O_6$	232.09	0.080	Decanetrioic acid
$C_{10}H_{18}O_5$	218.12	0.076	Hydroxy sebacic acid
$C_{10}H_{16}O_4$	200.10	0.075	Decendioic acid
$C_9H_{16}O_5$	204.10	0.070	Hydroxy azelaic acid
$C_4H_4O_3$	100.02	0.070	Oxo-butenoic acid
$C_{10}H_{16}O_5$	216.10	0.064	Oxo-sebacic acid
$C_9H_{14}O_5$	202.08	0.062	Oxo-azelaic acid

Table S19 Composition profile and top-20 most abundant species in Factor LV4 from ME-2 PMF results

Factor Name: LV-MultiGen-peroxy

Average elemental composition:
$C_{6.47}H_{11.47}O_{4.16}N_{0.00}S_{0.00}$
MW=155.90 OS_C=-0.202

Molecular composition:

Molecules	MW($g \cdot mol^{-1}$)	Relative Intensity	Possible species
$C_3H_4O_4$	104.01	0.62	Malonic acid
$C_7H_{14}O_4$	162.09	0.49	Hydroperoxyl heptanoic acid
$C_6H_{12}O_4$	148.07	0.45	Dihydroxy hexanoic acid
$C_9H_{16}O_4$	188.10	0.21	Azelaic acid
$C_9H_{18}O_4$	190.12	0.16	Hydroperoxyl nonanoic acid
$C_7H_{12}O_5$	176.07	0.15	Hydroxy pimelic acid
$C_{10}H_{18}O_4$	202.12	0.11	Sebacic acid
$C_7H_{12}O_4$	160.07	0.11	Pimelic acid
$C_6H_{10}O_4$	146.06	0.11	Adipic acid
$C_9H_{16}O_5$	204.10	0.088	Hydroxy azelaic acid
$C_8H_{16}O_4$	176.10	0.085	Hydroperoxyl octanoic acid
$C_9H_{14}O_4$	186.09	0.070	Nonendioic acid
$C_4H_6O_4$	118.02	0.059	Succinic acid
$C_3H_6O_4$	106.03	0.053	Glyceric acid
$C_8H_{14}O_5$	190.08	0.051	Hydroxy suberic acid
$C_{10}H_{16}O_4$	200.10	0.046	Decendioic acid
$C_9H_{14}O_5$	202.08	0.039	Oxo-azelaic acid
$C_2H_2O_4$	90.00	0.038	Oxalic acid
$C_8H_{14}O_4$	174.09	0.035	Suberic acid
$C_4H_4O_4$	116.01	0.032	Fumaric acid

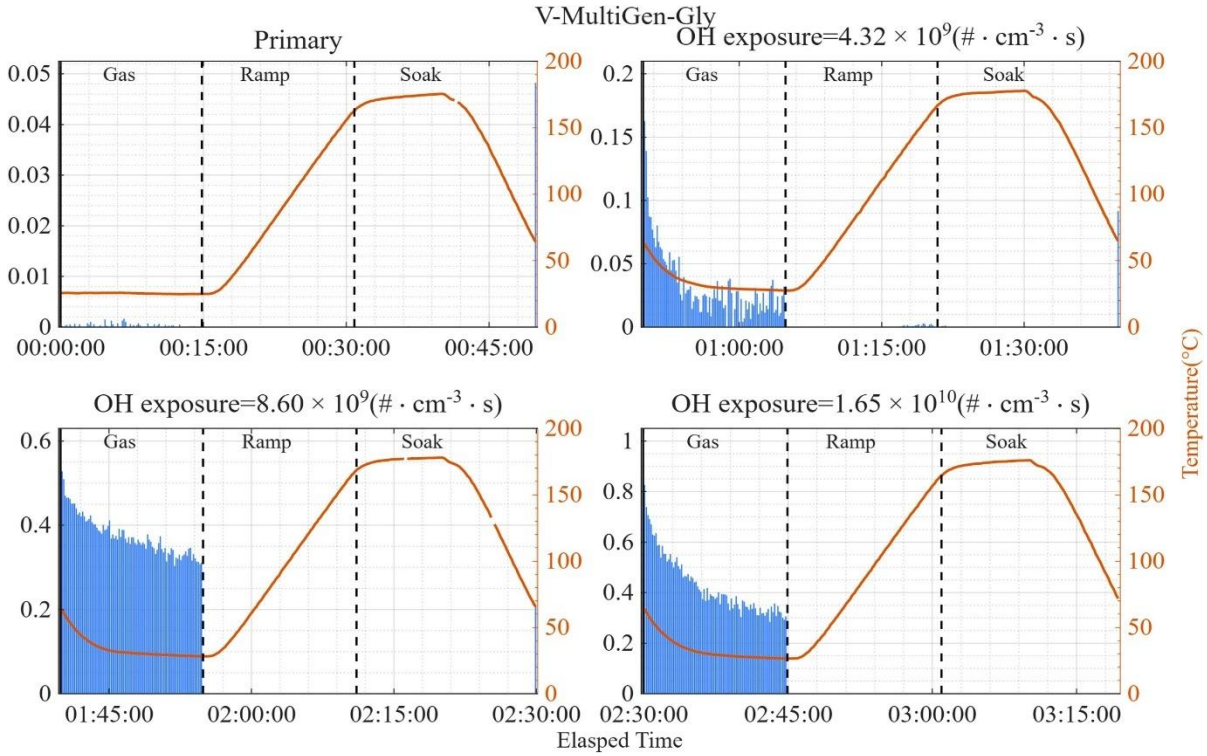

Figure S44 Intensity time series of volatile highly-oxidated product factor V-MultiGen-Gly (presented remarkably only in gas phase, possibly related to oxidation of glycerol-structure-related compounds) in PMF results at different OH exposure during FIGAERO measurement circles.

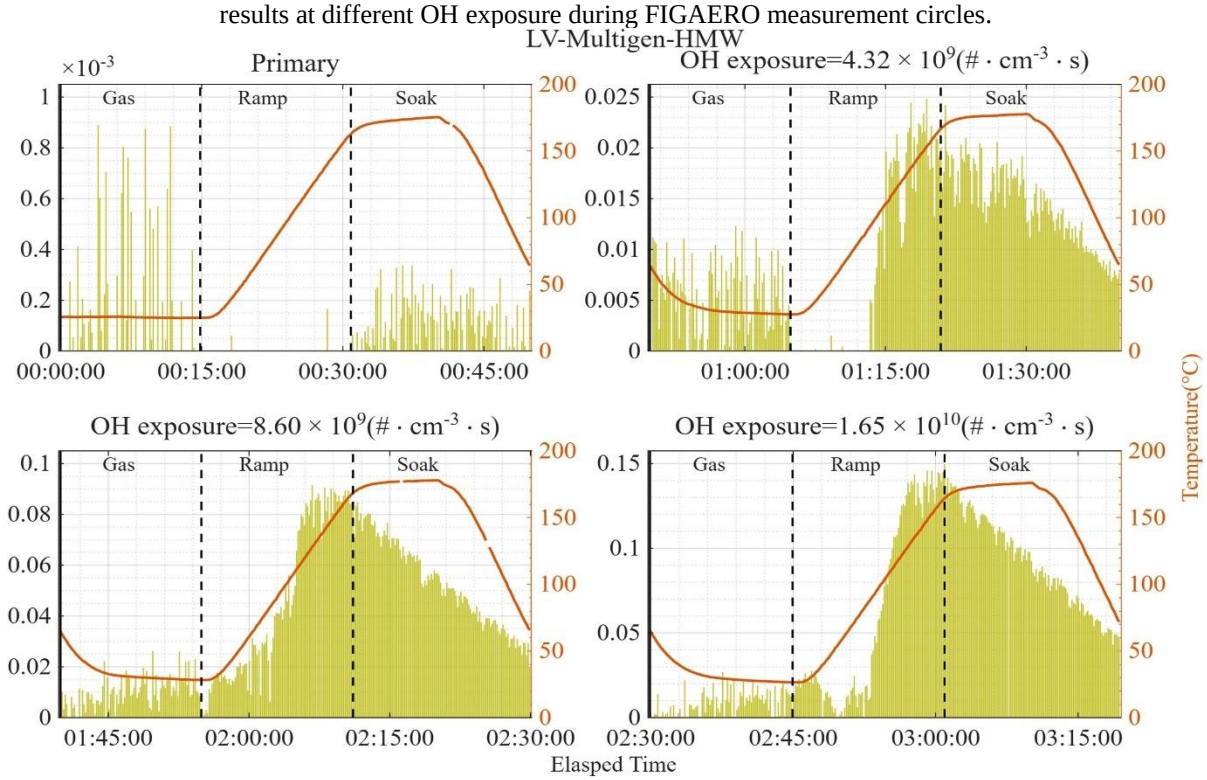

Figure S45 Intensity time series of low-volatile highly-oxidated product factor LV-Multigen-HMW (presented remarkably only in aerosol phase) in PMF results at different OH exposure during FIGAERO measurement circles.

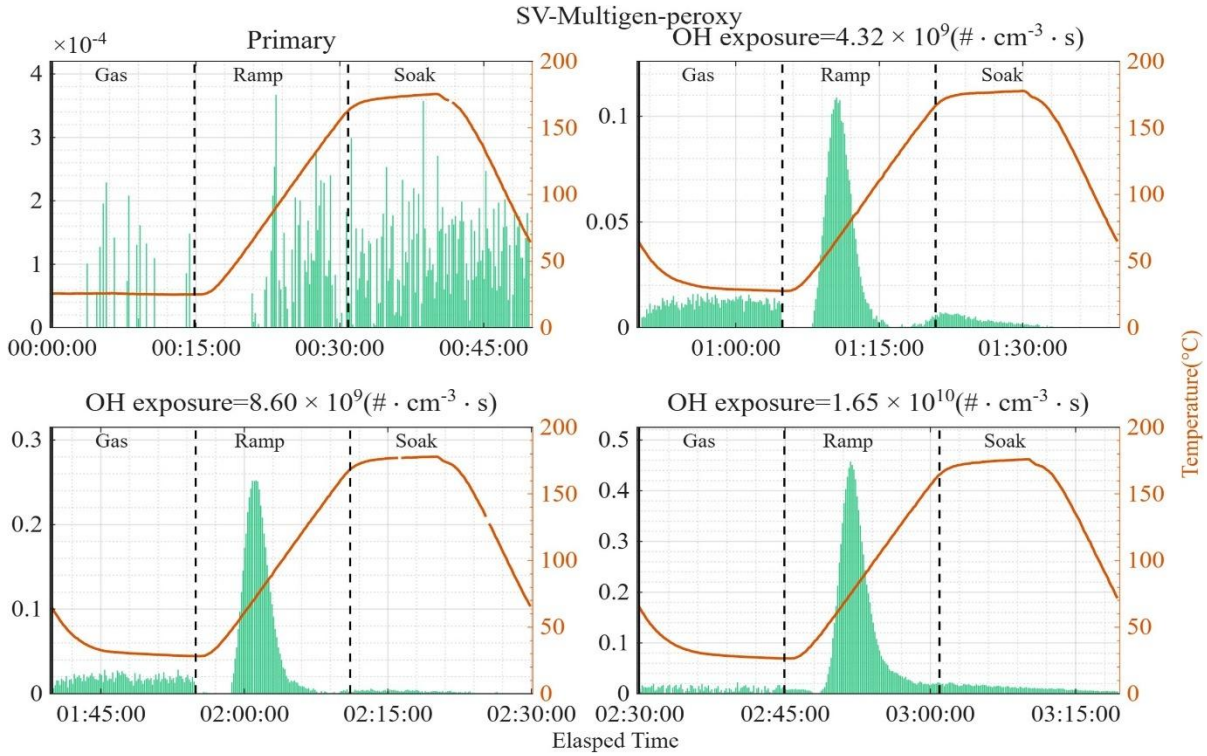

Figure S46 Intensity time series of semi-volatile highly-oxidated product factor SV-Multigen-peroxy (presented dominantly in aerosol phase) in PMF results at different OH exposure during FIGAERO measurement circles.

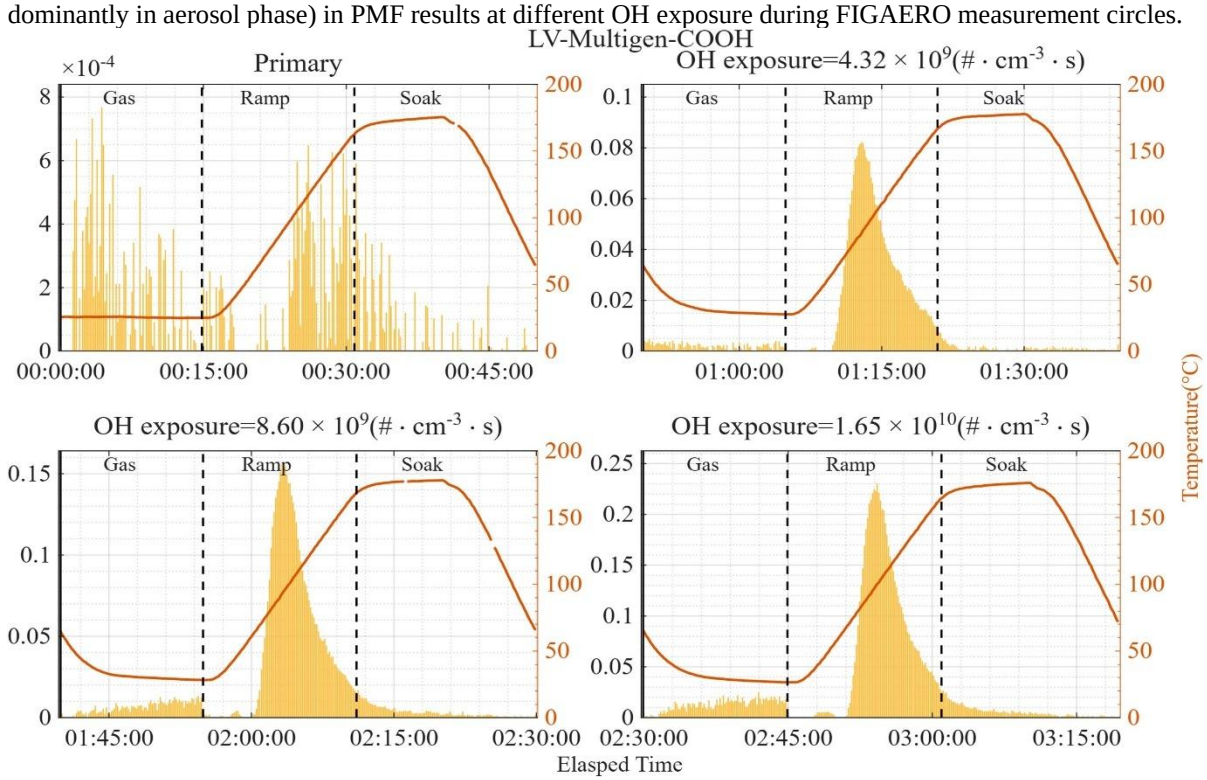

Figure S47 Intensity time series of semi-volatile highly-oxidated product factor LV-Multigen-COOH (presented dominantly in aerosol phase) in PMF results at different OH exposure during FIGAERO measurement circles.

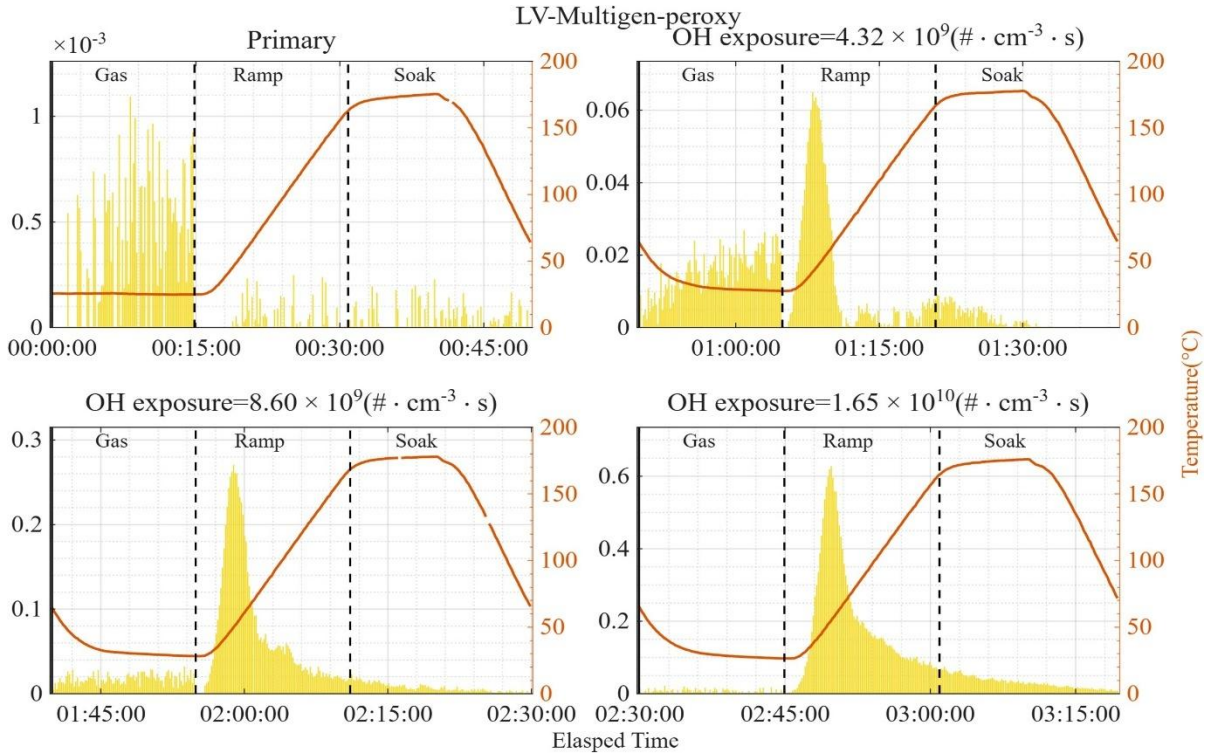

Figure S48 Intensity time series of low-volatile highly-oxidated product factor LV-Multigen-peroxy (presented remarkably only in aerosol phase) in PMF results at different OH exposure during FIGAERO measurement circles.

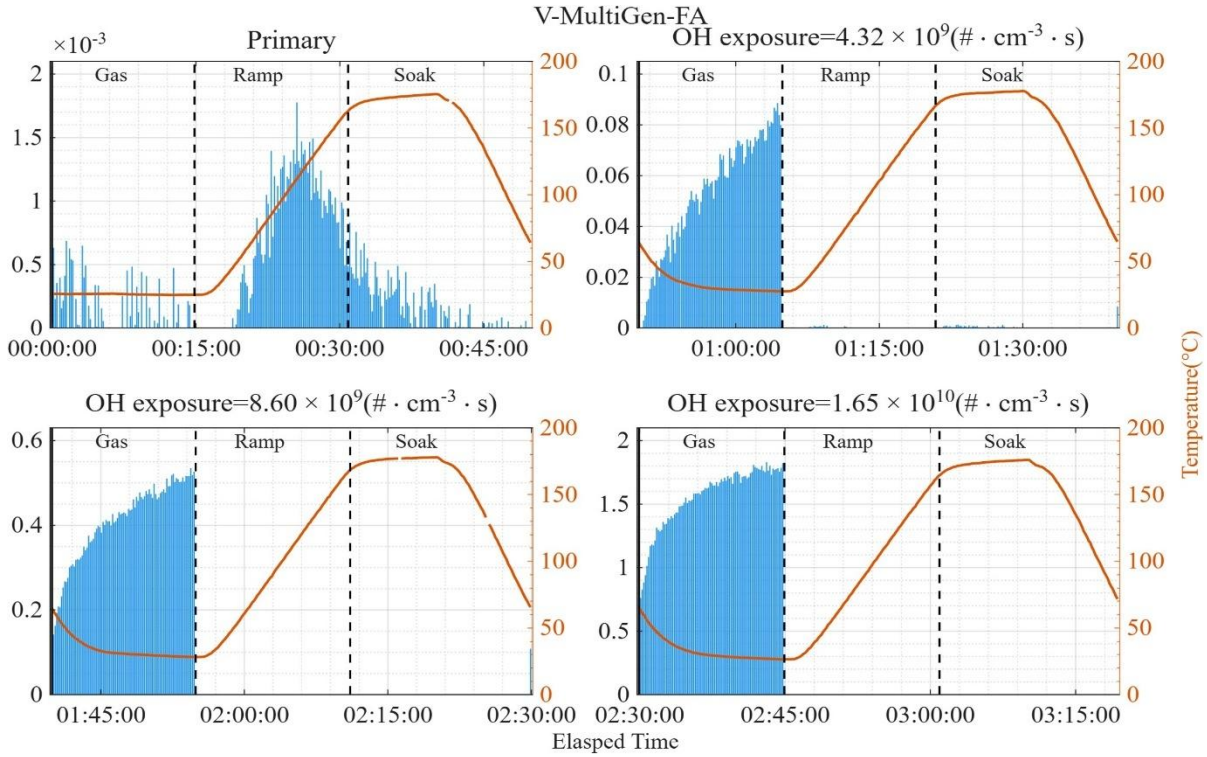

Figure S49 Intensity time series of volatile highly-oxidated product factor V-MultiGen-FA (presented remarkably only in gas phase, possibly related to oxidation of long-chain-fatty-acid-structure-related compounds) in PMF results at different OH exposure during FIGAERO measurement circles.

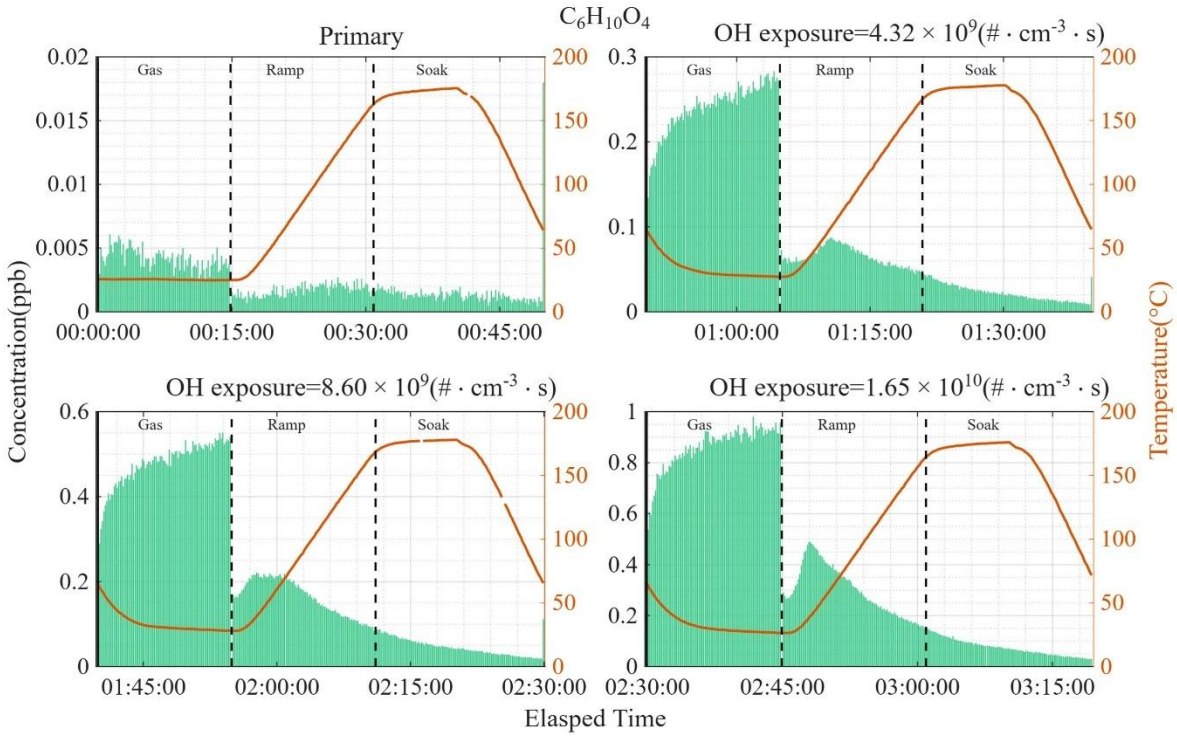

Figure S50 Concentration time series of compound with elemental composition of $C_6H_{10}O_4$ (probably adipic acid) at different OH exposure during FIGAERO measurement of flow tube experiment.

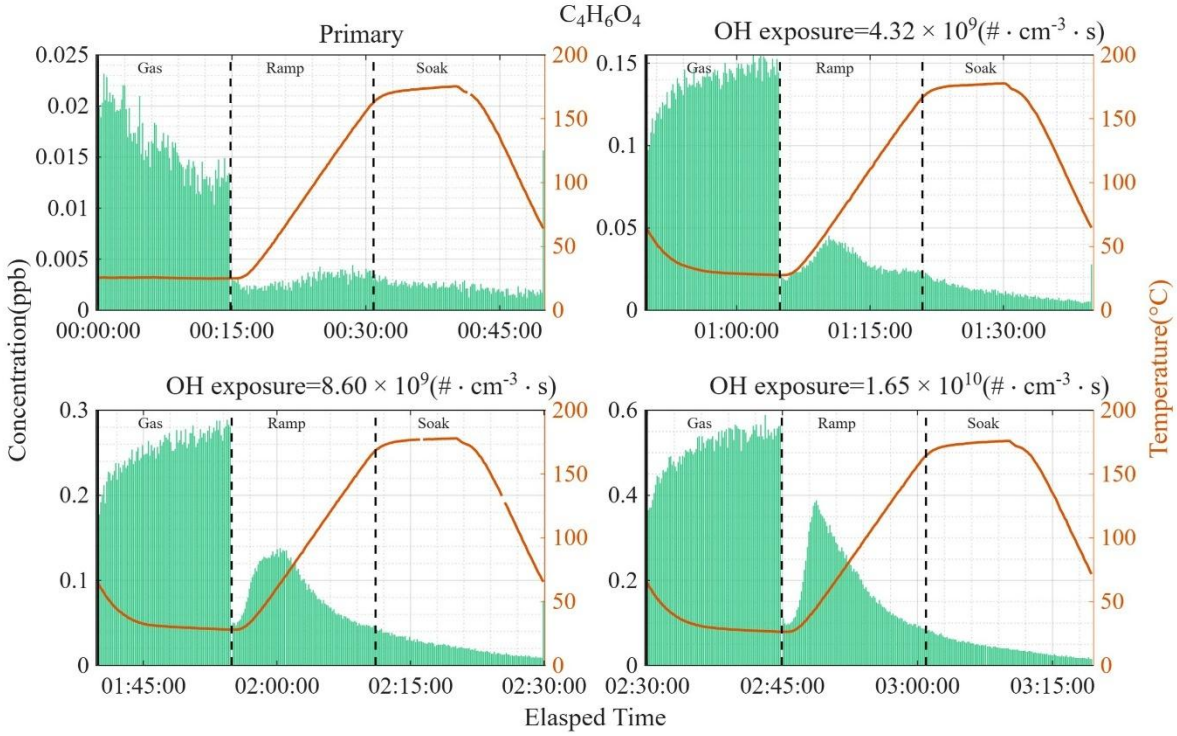

Figure S51 Concentration time series of compound with elemental composition of $C_4H_6O_4$ (probably succinic acid) at different OH exposure during FIGAERO measurement of flow tube experiment.

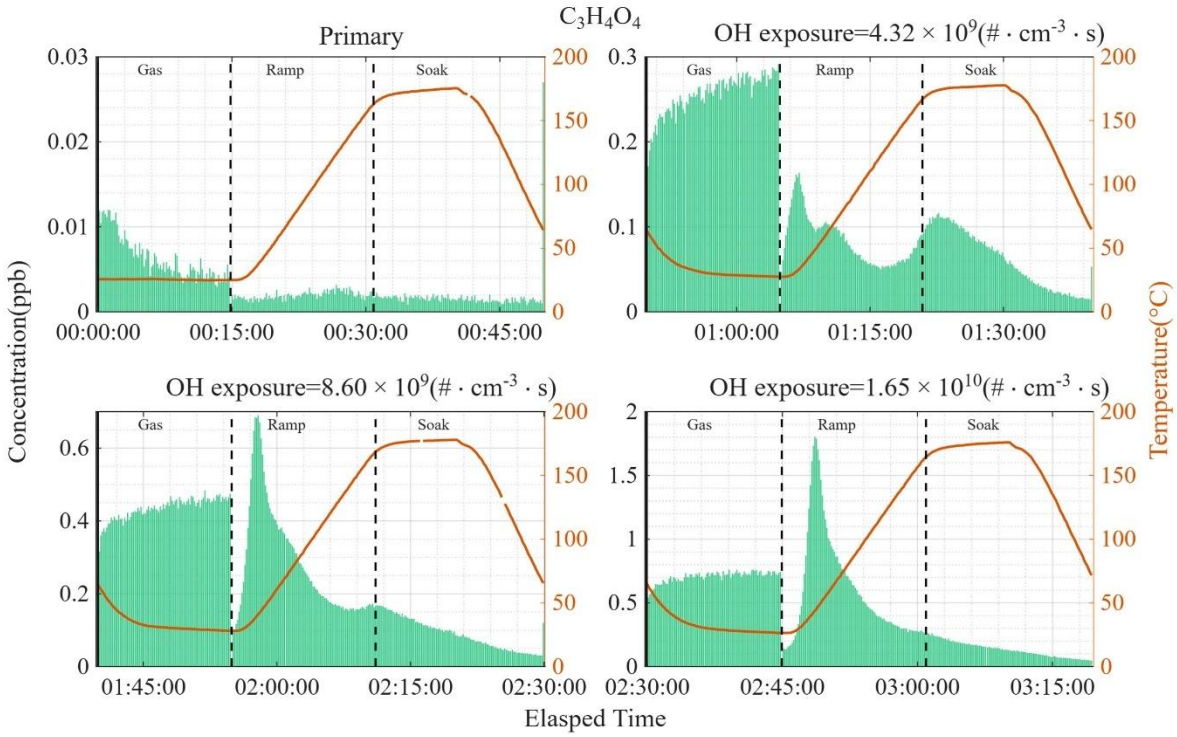

Figure S52 Concentration time series of compound with elemental composition of $C_3H_4O_4$ (probably malonic acid) at different OH exposure during FIGAERO measurement of flow tube experiment.

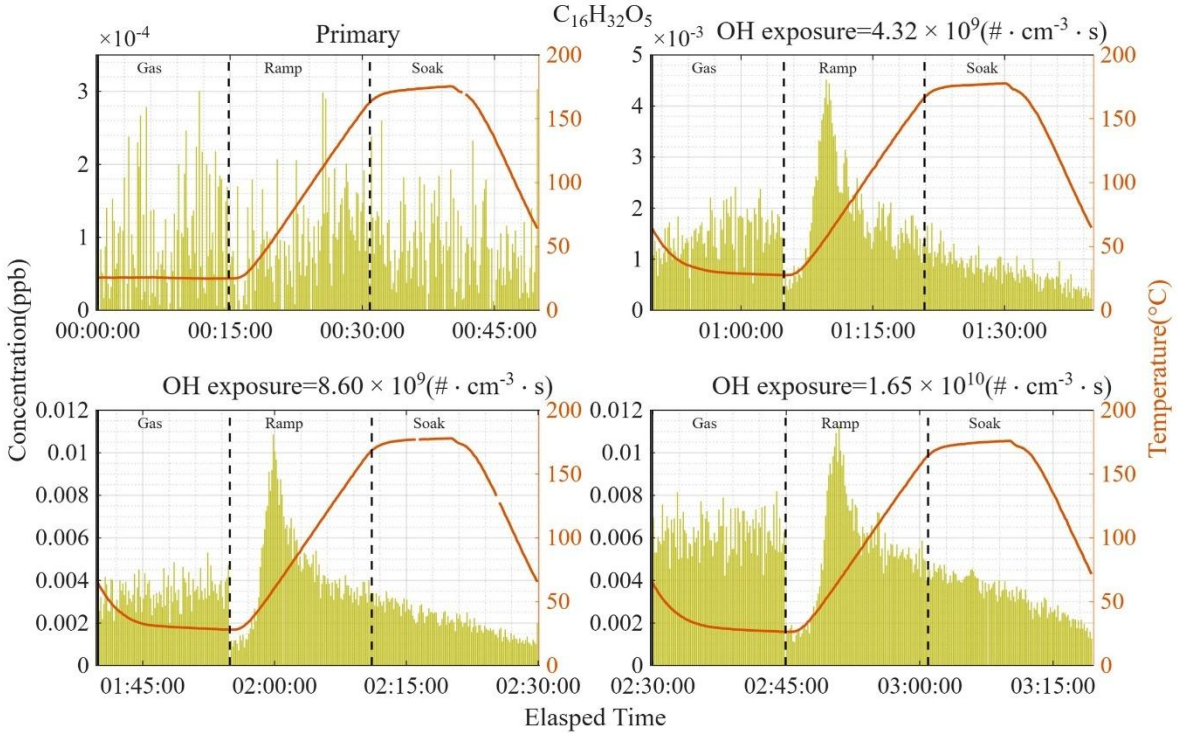

Figure S53 Concentration time series of compound with elemental composition of $C_{16}H_{32}O_5$ at different OH exposure during FIGAERO measurement of flow tube experiment.

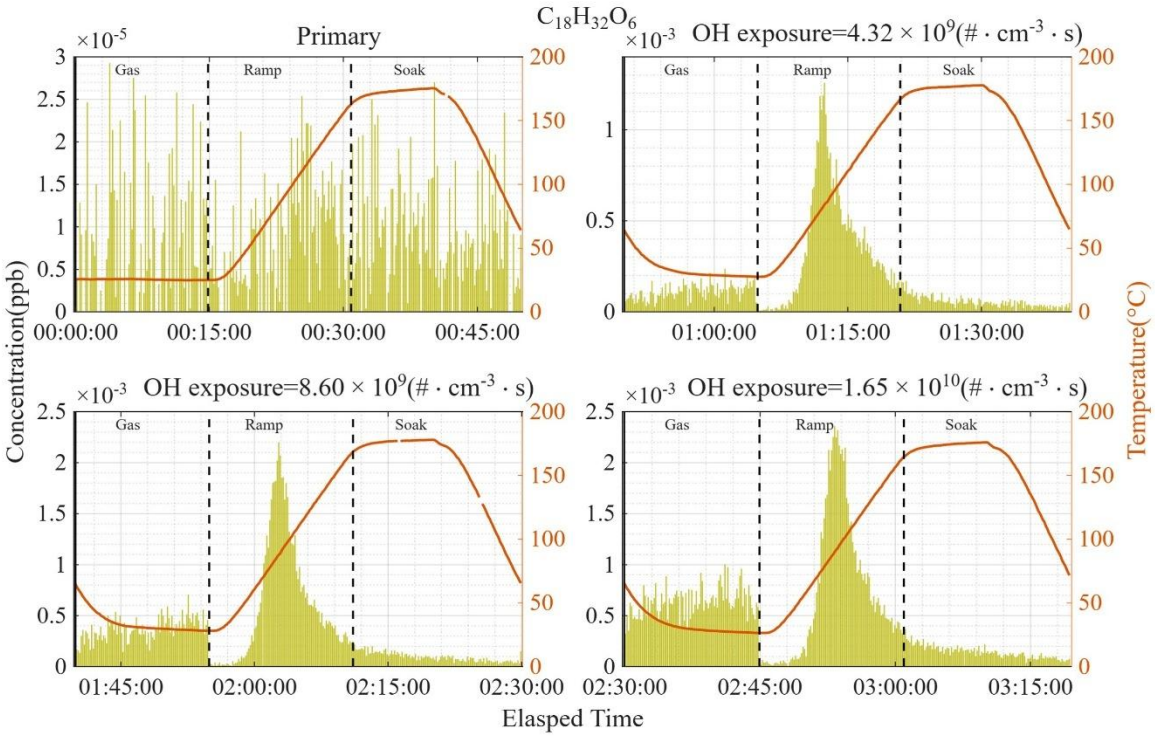

Figure S54 Concentration time series of compound with elemental composition of $C_{18}H_{32}O_6$ at different OH exposure during FIGAERO measurement of flow tube experiment.

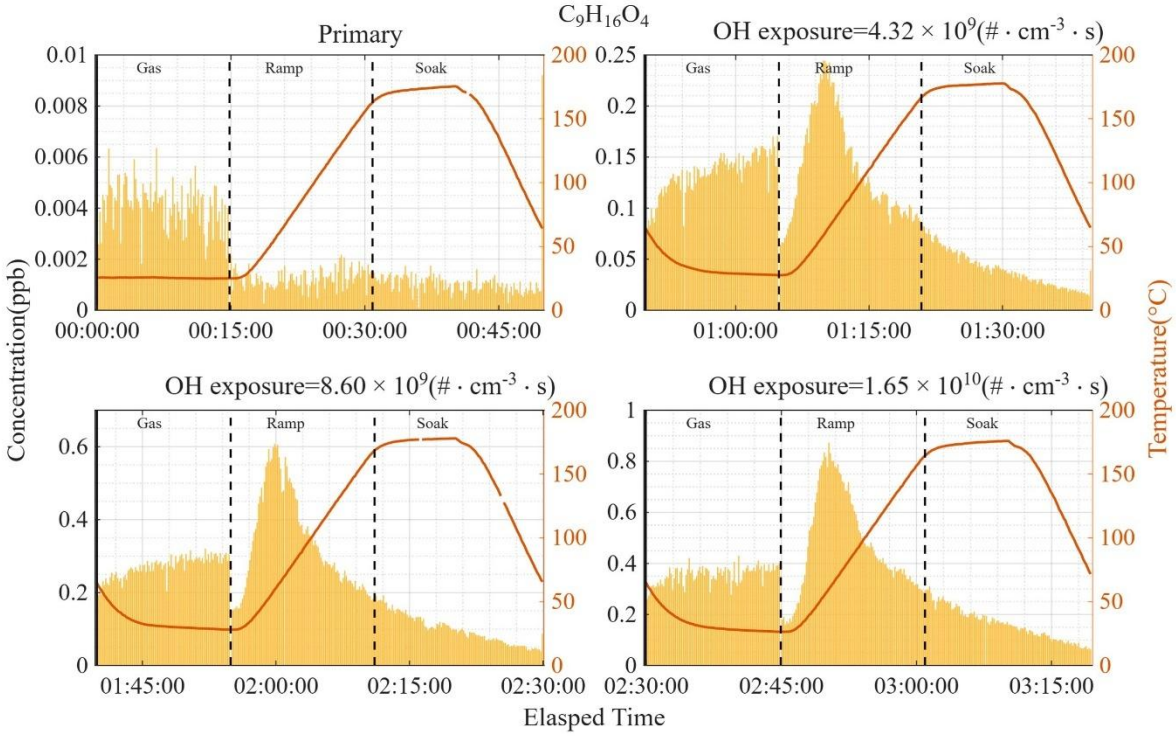

Figure S55 Concentration time series of compound with elemental composition of $C_9H_{16}O_4$ (probably azelaic acid) at different OH exposure during FIGAERO measurement of flow tube experiment.

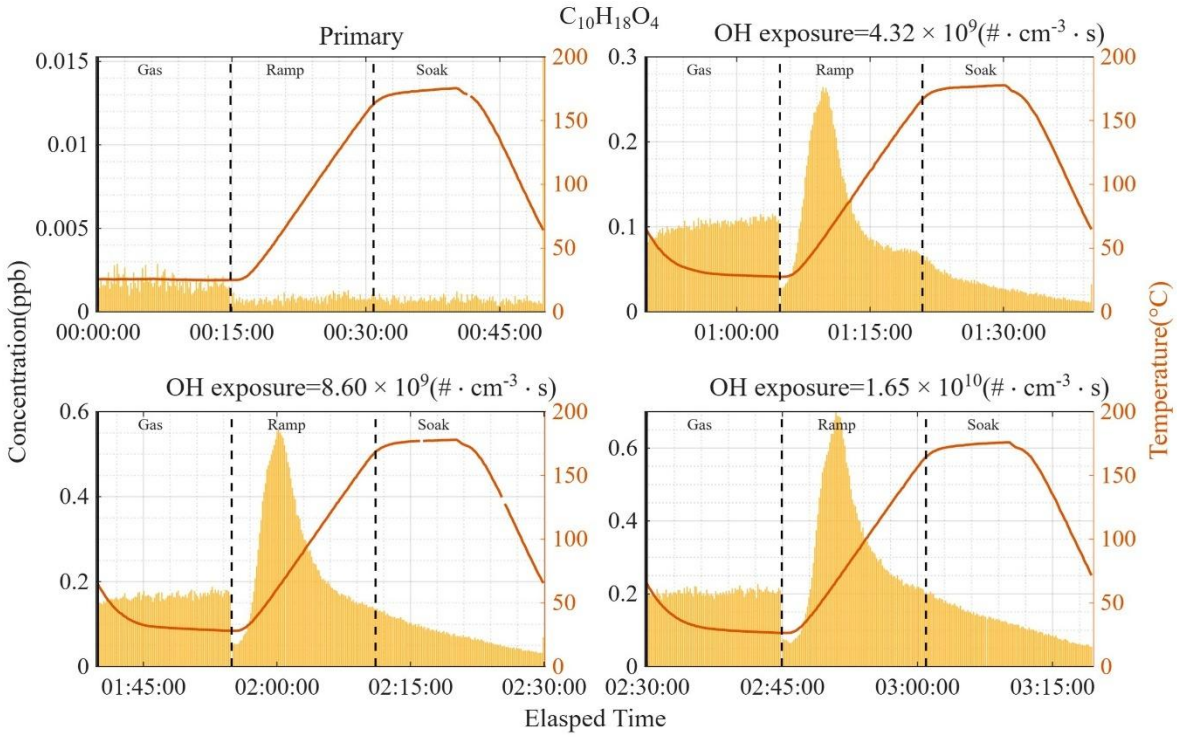

Figure S56 Concentration time series of compound with elemental composition of $C_{10}H_{18}O_4$ (probably sebacic acid) at different OH exposure during FIGAERO measurement of flow tube experiment.

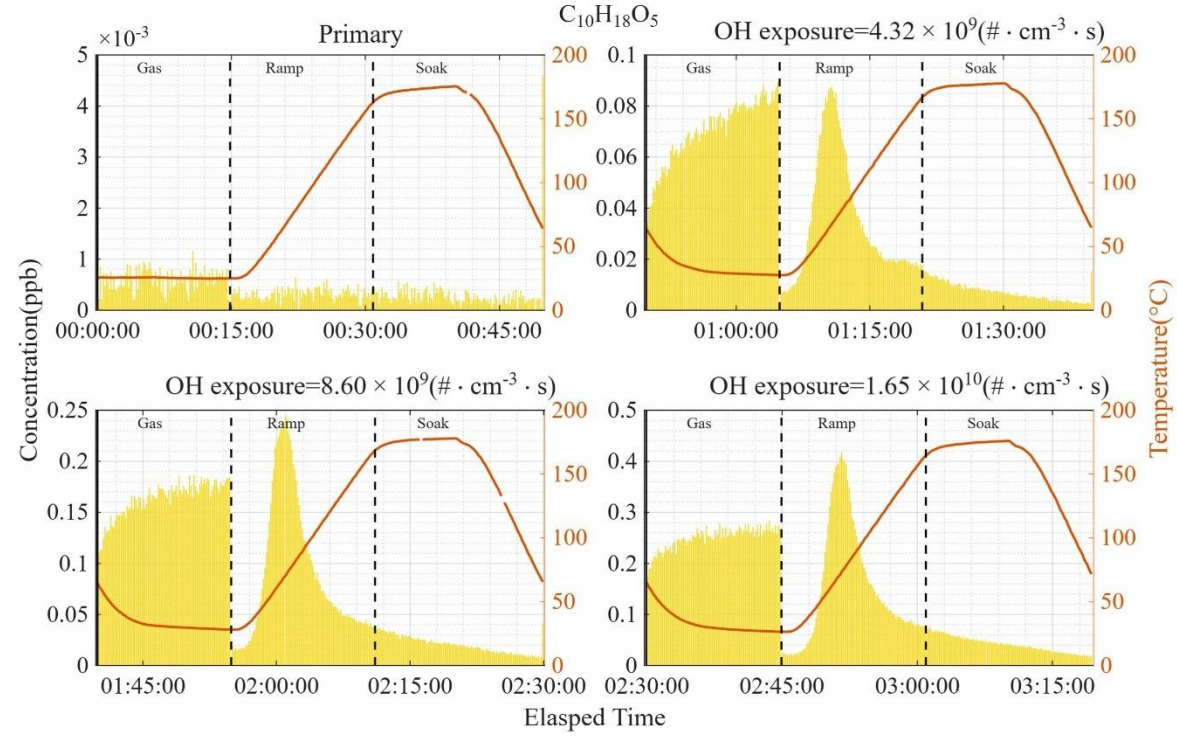

Figure S57 Concentration time series of compound with elemental composition of $C_{10}H_{18}O_5$ (probably hydroxy sebacic acid) at different OH exposure during FIGAERO measurement of flow tube experiment.

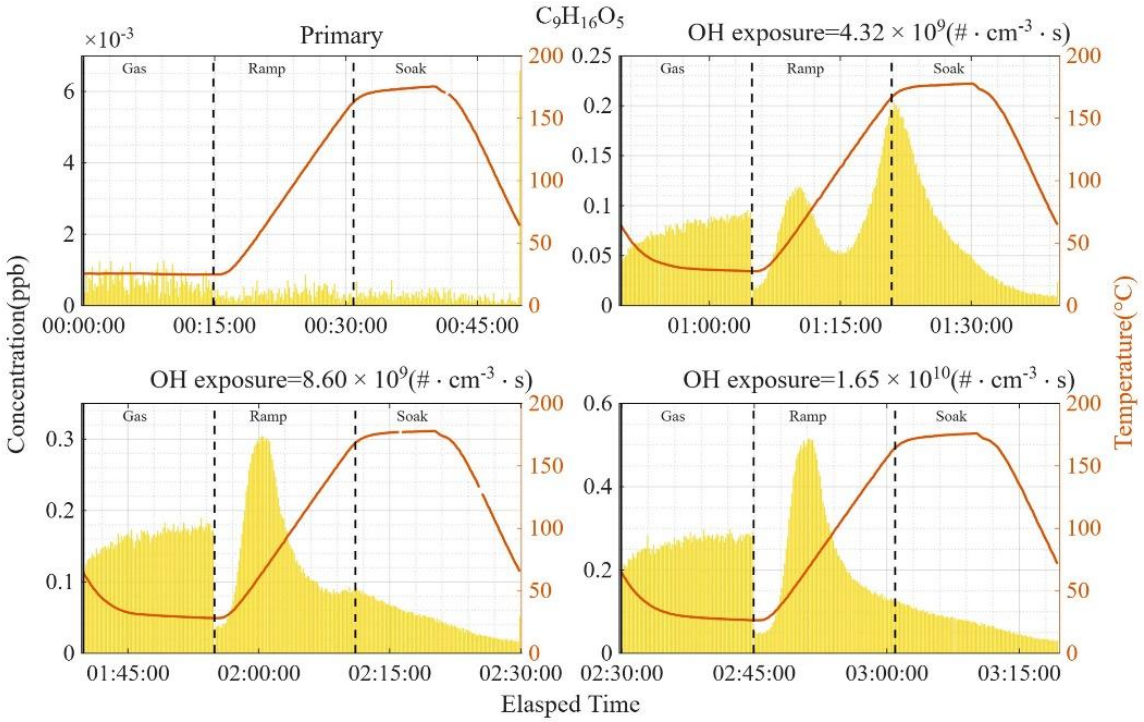

Figure S58 Concentration time series of compound with elemental composition of $C_9H_{16}O_5$ (probably hydroxy azelaic acid) at different OH exposure during FIGAERO measurement of flow tube experiment

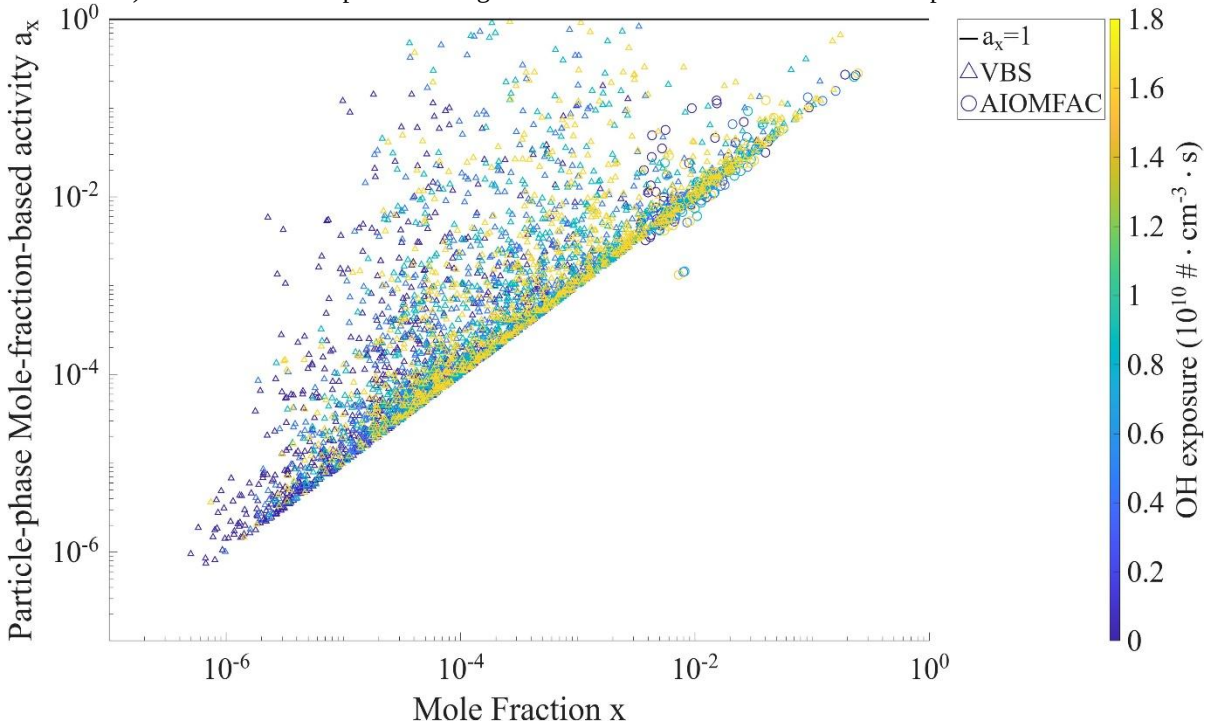

Figure S59 Particle phase activity of top 50 species detected by CIMS utilizing AIOMFAC model and VBS parameterization as OH exposure increases. Black line at the bottom represents a=1 as the boundary of uniform liquid phase and possible liquid-liquid separation.

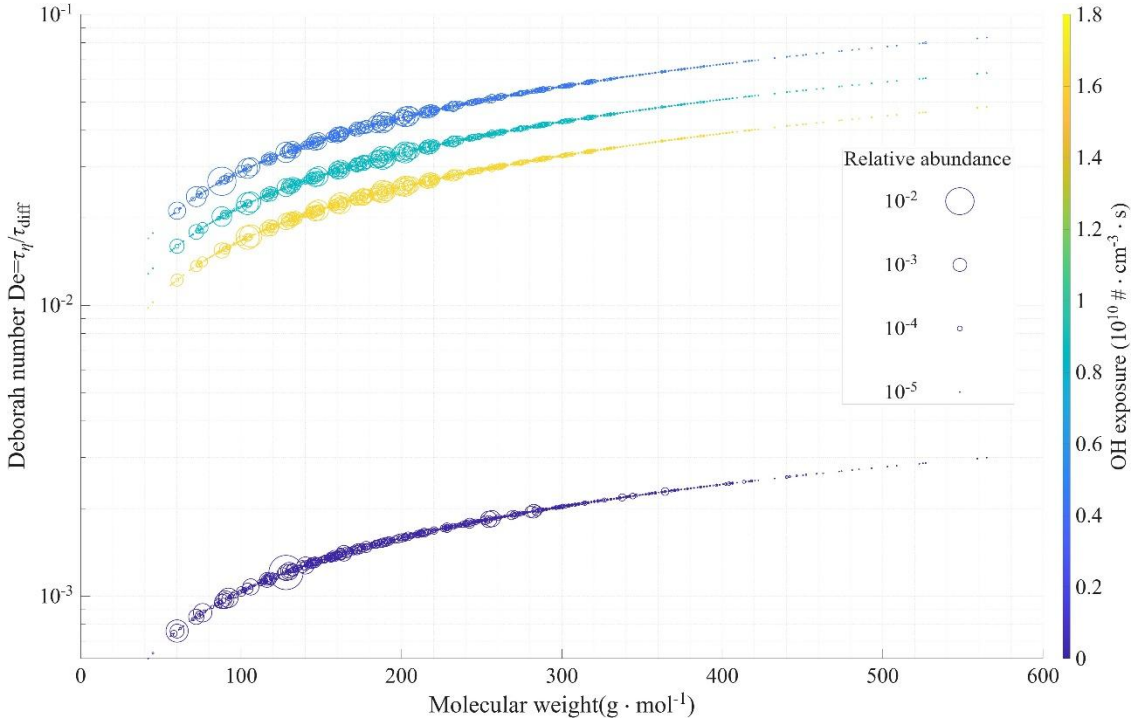

Figure S60 Particle phase Deborah number of detected species with enhancement of oxidation exposure. Marker size represents relative abundance.

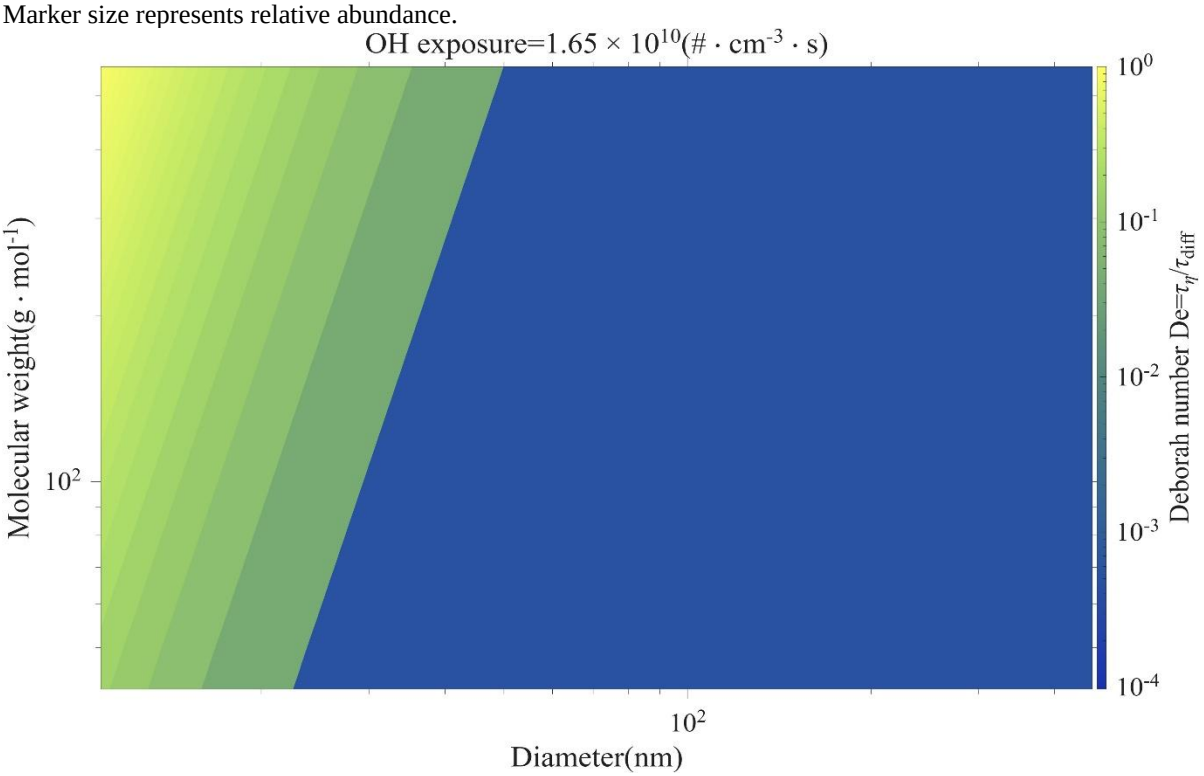

Figure S61 Particle phase Deborah number distribution of detected species and particle diameter in organic aerosols at oxidation exposure 1.65 ·10^{10} # cm^{-3} s.

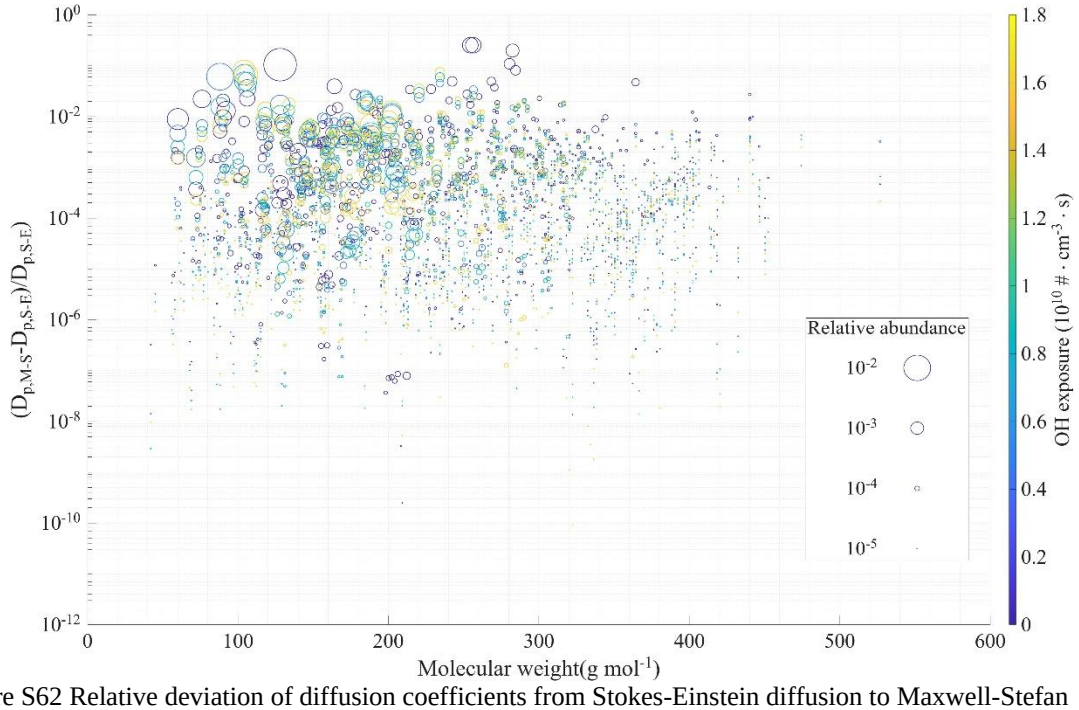

Figure S62 Relative deviation of diffusion coefficients from Stokes-Einstein diffusion to Maxwell-Stefan diffusions.

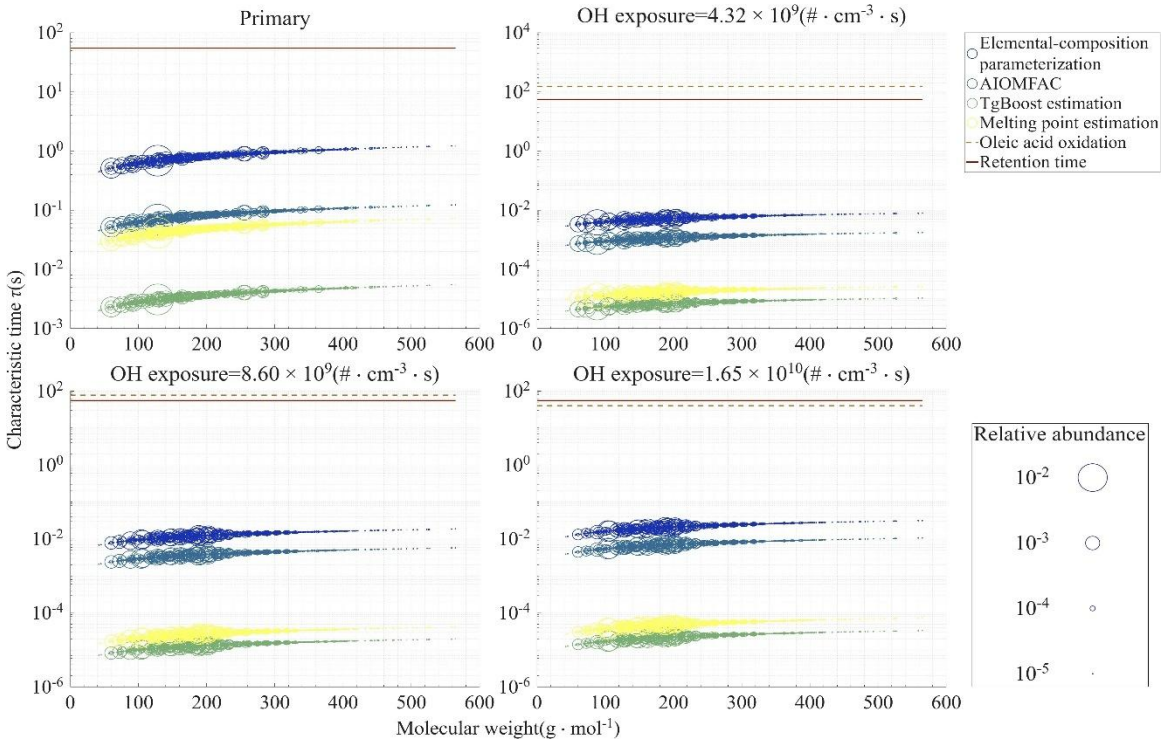

Figure S63 Influence of various viscosity estimation method on particle-phase diffusion time scale of primary and secondary organic aerosols. Blue: 2-D-VBS based parametrization; blue-green: AIOMFAC-VISC; green: tgBoost method; yellow: melting point method.

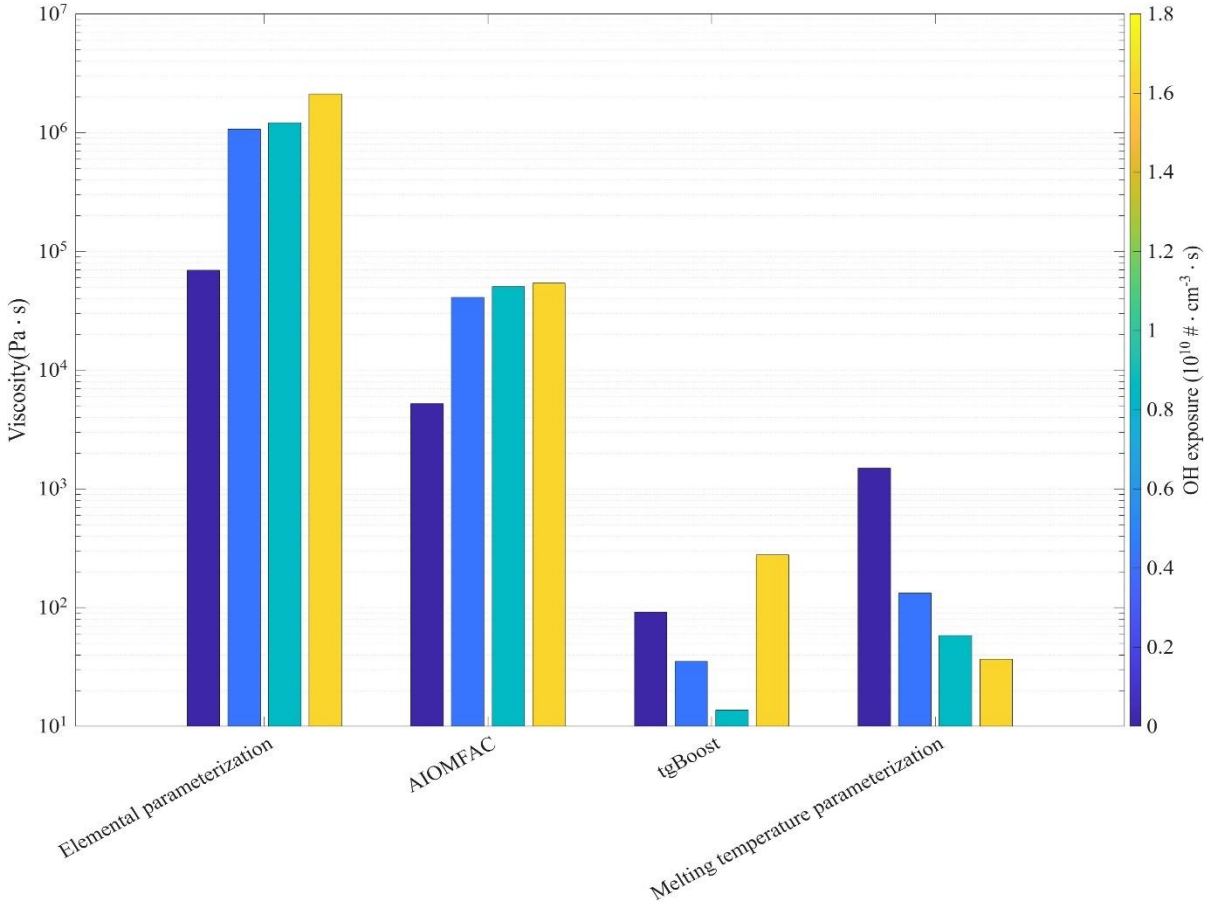

Figure S64 Influence of various viscosity estimation method on particle-phase viscosity time scale of primary and secondary organic aerosols.

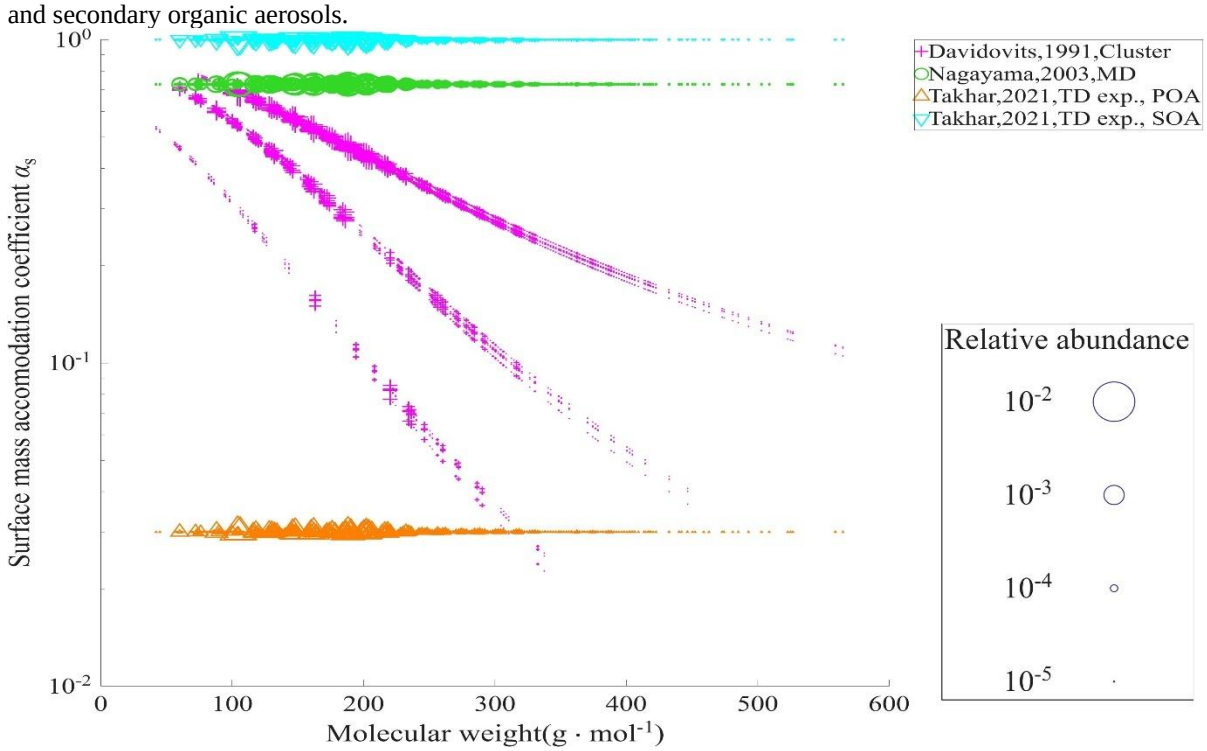

Figure S65 Comparison between parameterization methods(Davidovits et al., 1991; Nagayama and Tsuruta, 2003; Davidovits et al., 2006) and previous experimental results(Takhar et al., 2019; Takhar et al., 2021) of surface mass accommodation coefficient α_s.

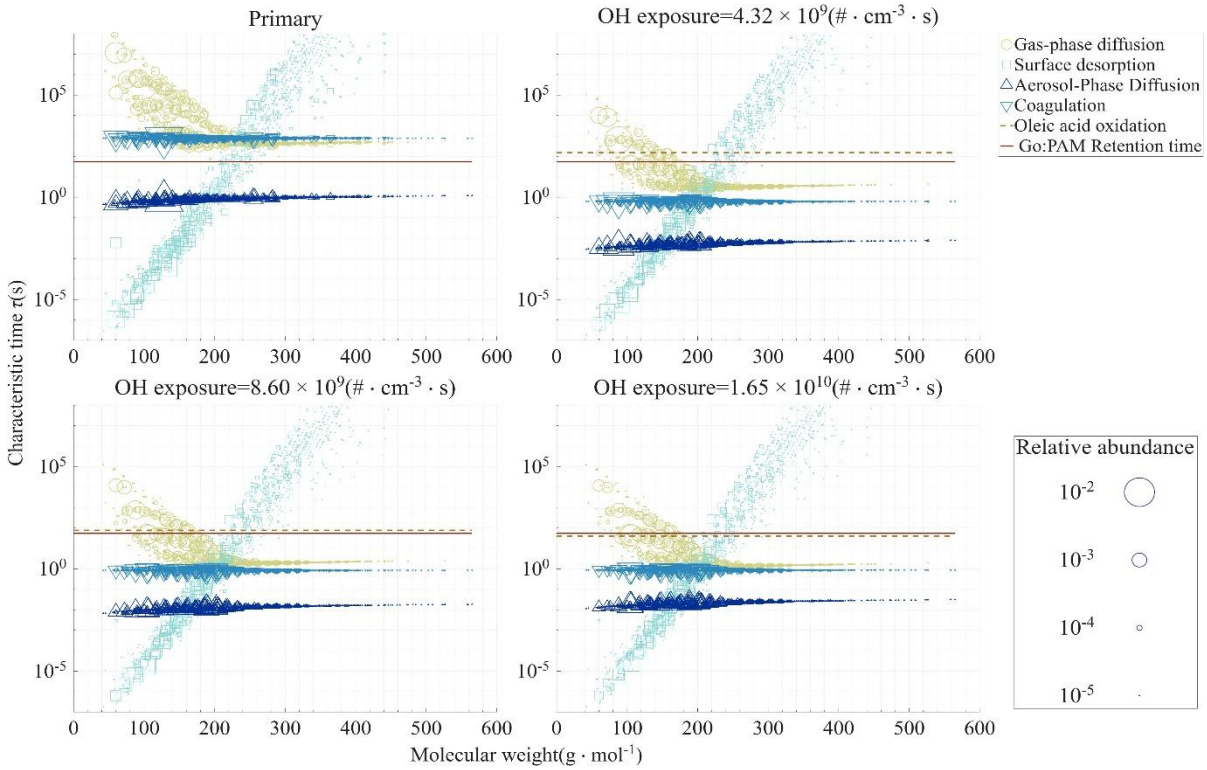

Figure S66 Characteristic time scales of FIGAERO-CIMS-detected species for gas-particle partitioning processes across the investigated OH exposures. Markers and lines are defined as in Figure 4. Surface mass accommodation coefficient are estimated based on **parameterization methods 2** shown in Section S5(Nagayama and Tsuruta, 2003).

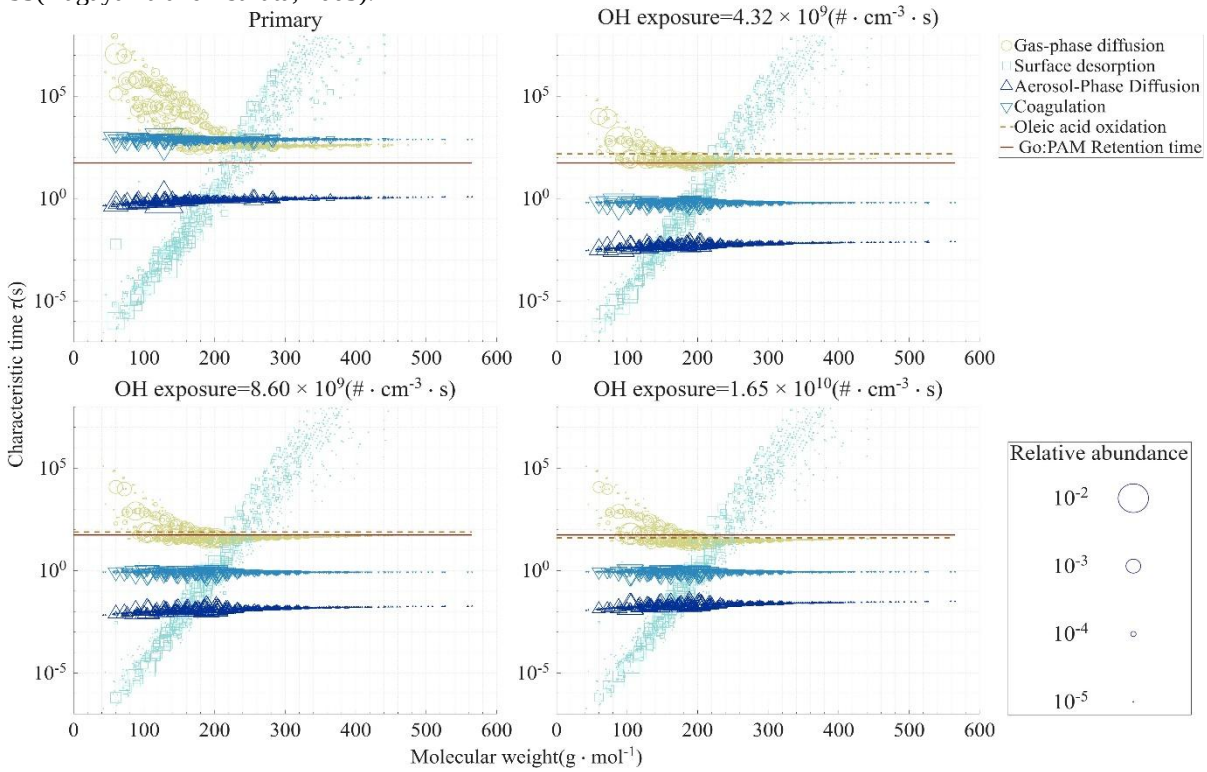

Figure S67 Characteristic time scales of FIGAERO-CIMS-detected species for gas-particle partitioning processes across the investigated OH exposures. Markers and lines are defined as in Figure 4. Surface mass accommodation coefficient α is set to 0.03 for secondary aerosols and 1 for primary aerosols(Takhar et al., 2019; Takhar et al., 2021).

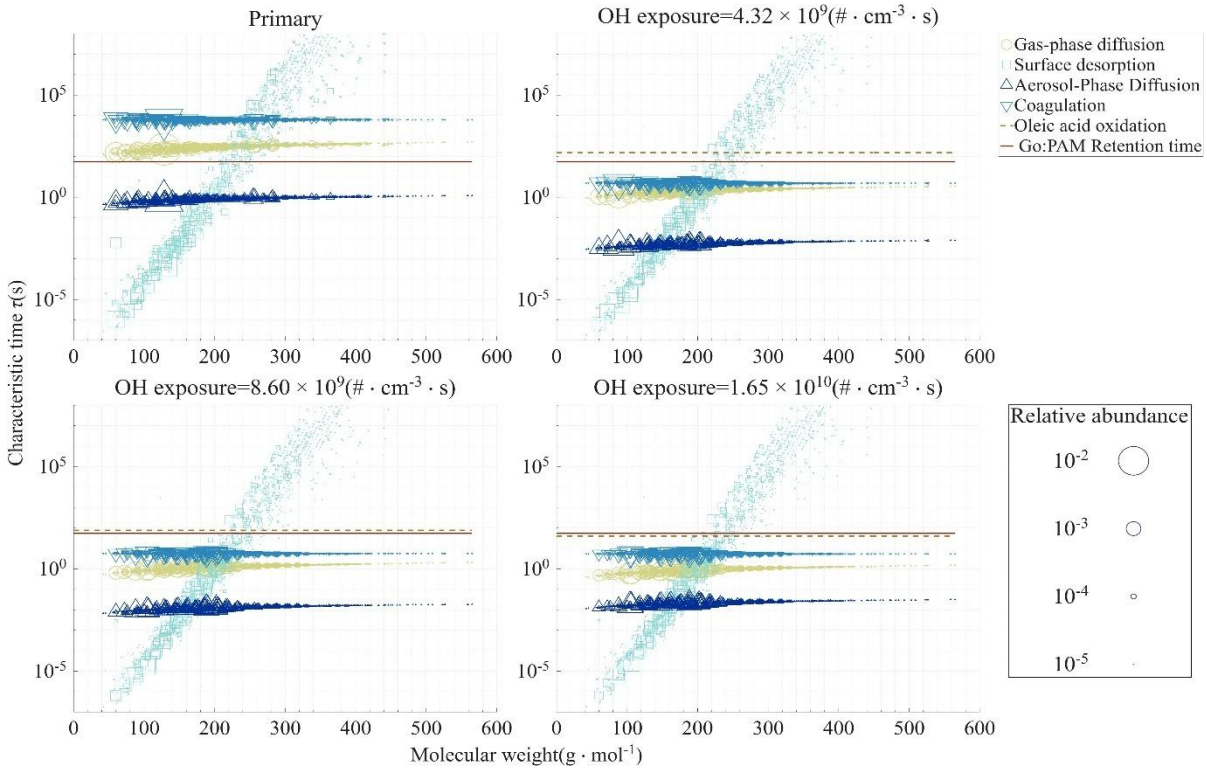

Figure S68 Characteristic time scales of FIGAERO-CIMS-detected species for gas-particle partitioning processes across the investigated OH exposures. Markers and lines are defined as in Figure 4. Surface mass accommodation coefficient α is set 1 and do not use the effective mass accommodation coefficient α_{eff}(Takhar et al., 2019; Takhar et al., 2021).

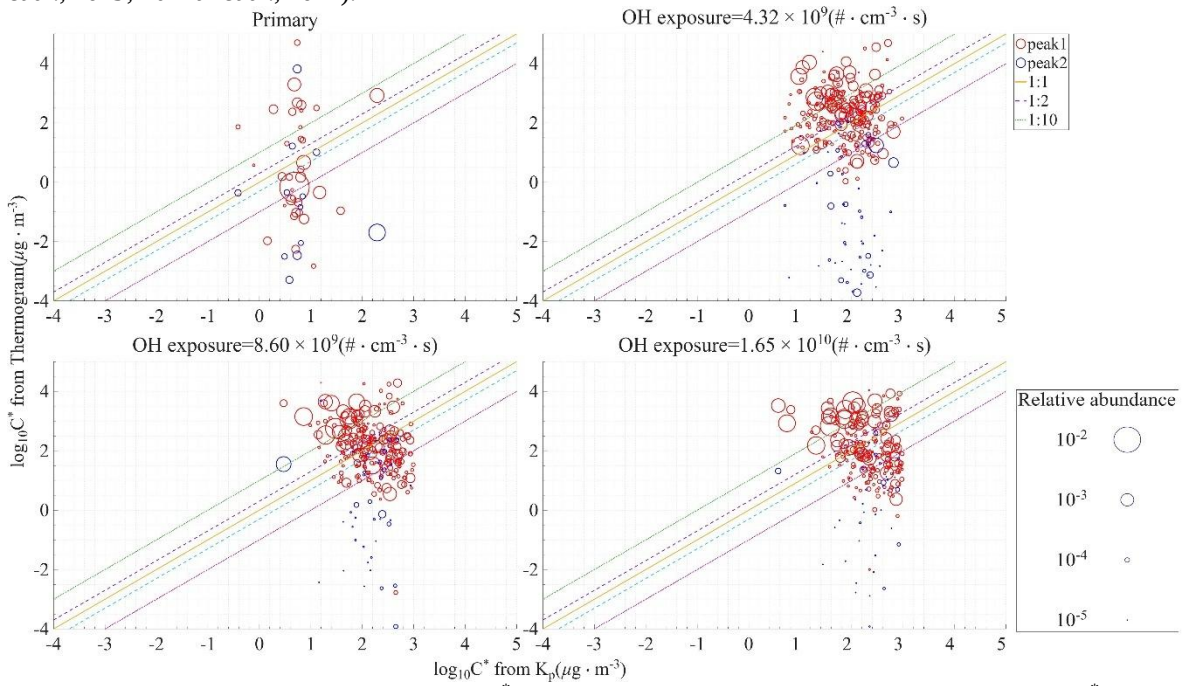

Figure S69 Relation between corresponding C^* value of major peaks(red) and minor peaks(blue) to C^* from gas-phase and aerosol-phase concentration

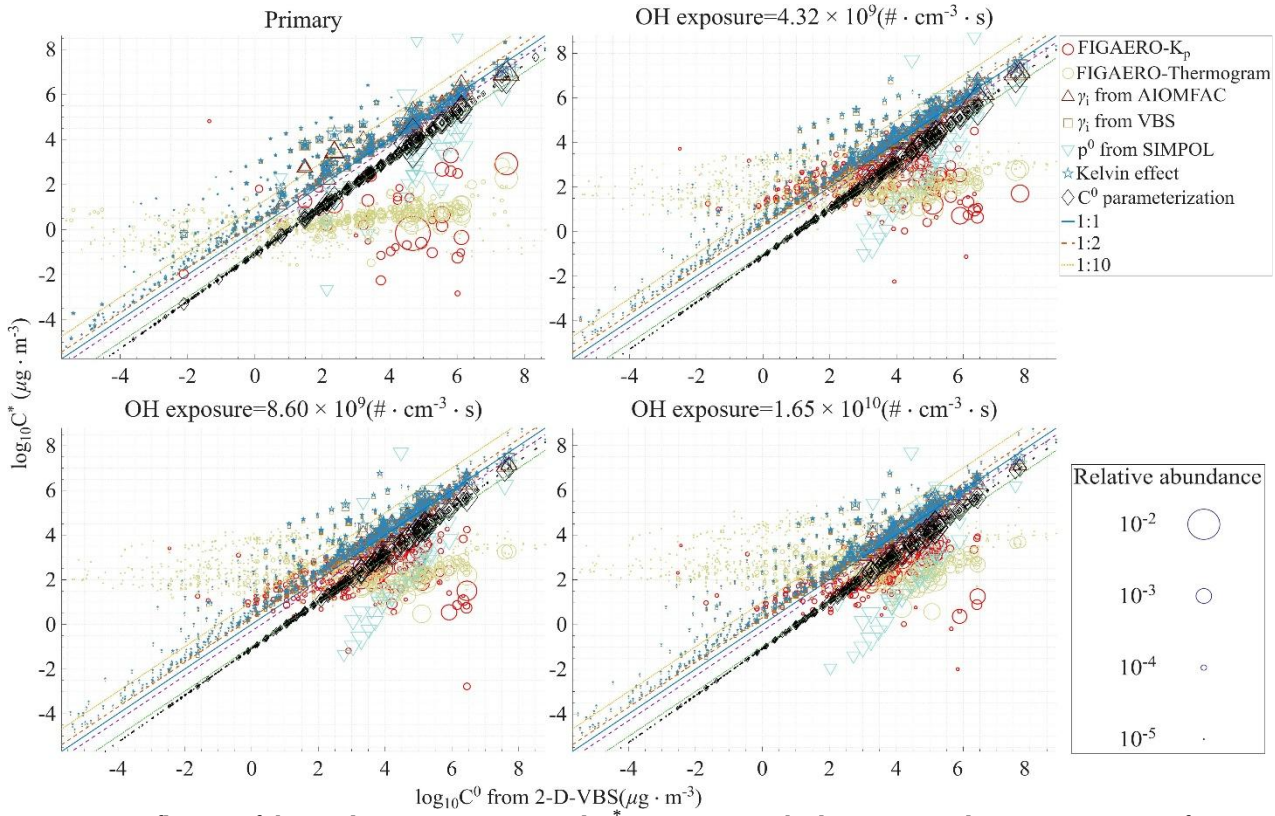

Figure S70 Influence of thermodynamic treatment and C^* estimation methods on saturated concentration C* of FIGAERO-CIMS detected species utilizing various estimation methods with enhancement of OH exposure. Markers show K_p from FIGAERO measurements (red circle), T_{max} from FIGAERO thermograms (yellow circle), activity coefficient from AIOMFAC (triangle), activity coefficient from VBS parameterization (pentagram), saturation vapor pressure from SIMPOL (reverse triangle), Kelvin effect(hexagram), and $C^*$from C^0 parametrization(diamond). Lines shows 1:1,1:2 and 1:10 boundary. Marker size represents relative abundance of species.

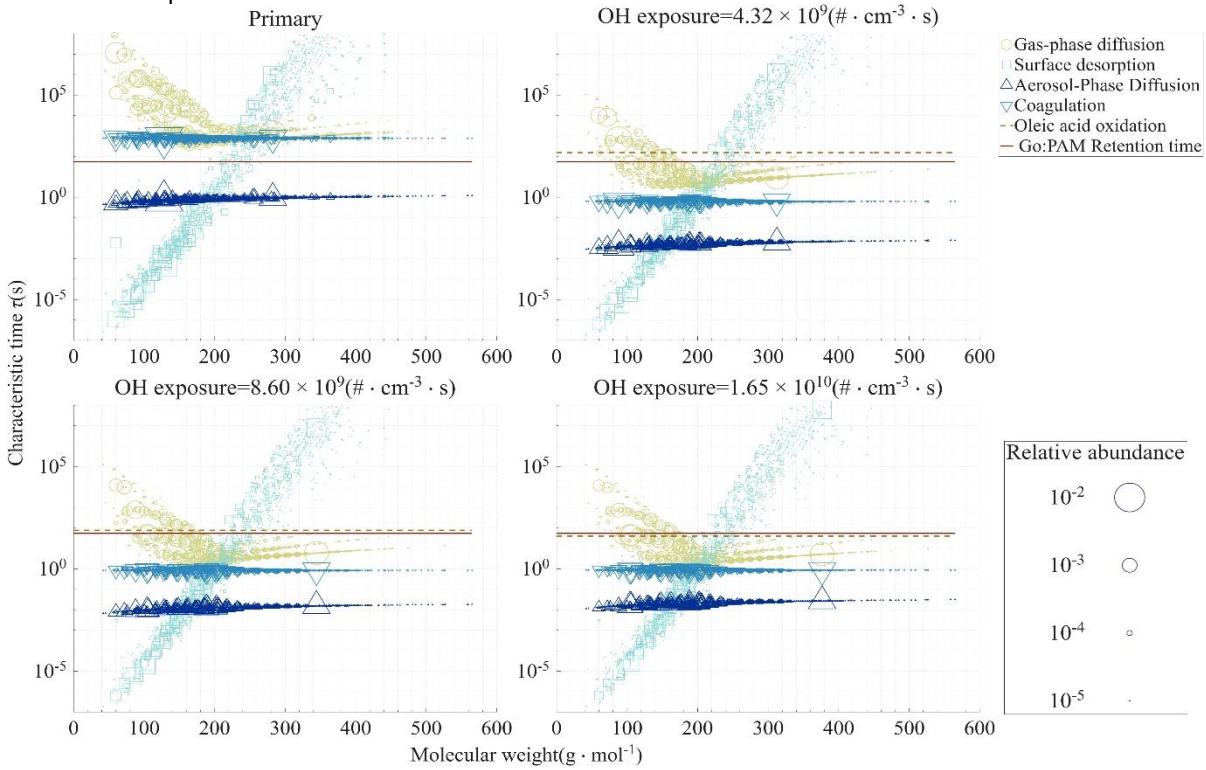

Figure S71 Sensitivity analysis on influence of possible underestimated long-chain fatty acid related species on kinetics of FIGAERO-CIMS-detected species for gas-particle partitioning processes across the investigated OH exposures, with treatment method as adding oleic acid and its oxidation product $C_{18}H_{32}O_{4,6,8}$ to 10% of total

signal intensity of particle phase. Markers and lines are defined as in Figure 4. Surface mass accommodation coefficient α are estimated utilizing parameterization method 1 shown in Section S5.

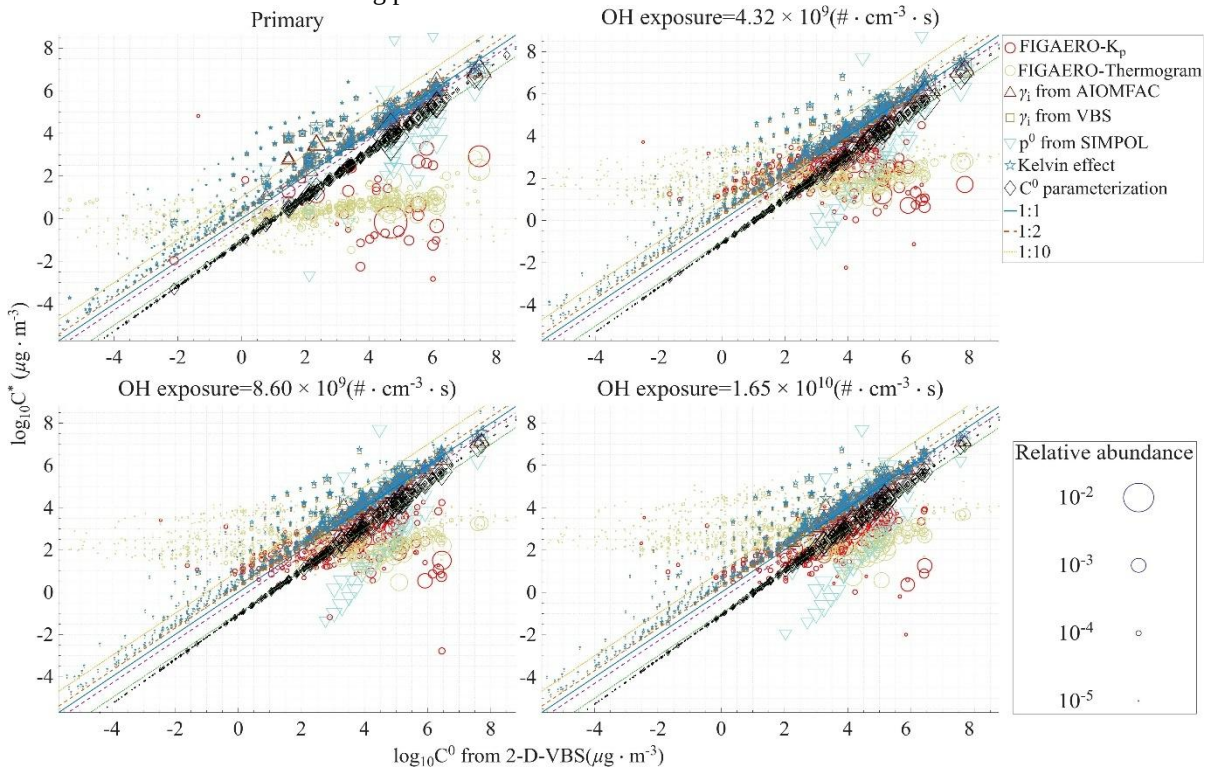

Figure S72 Sensitivity analysis on influence of possible underestimated long-chain fatty acid related species on thermodynamics of FIGAERO-CIMS-detected species for gas-particle partitioning processes across the investigated OH exposures, with treatment method as adding oleic acid and its oxidation product $C_{18}H_{32}O_{4,6,8}$ to 10% of total signal intensity of particle phase. Markers and lines are defined as in Figure 5.

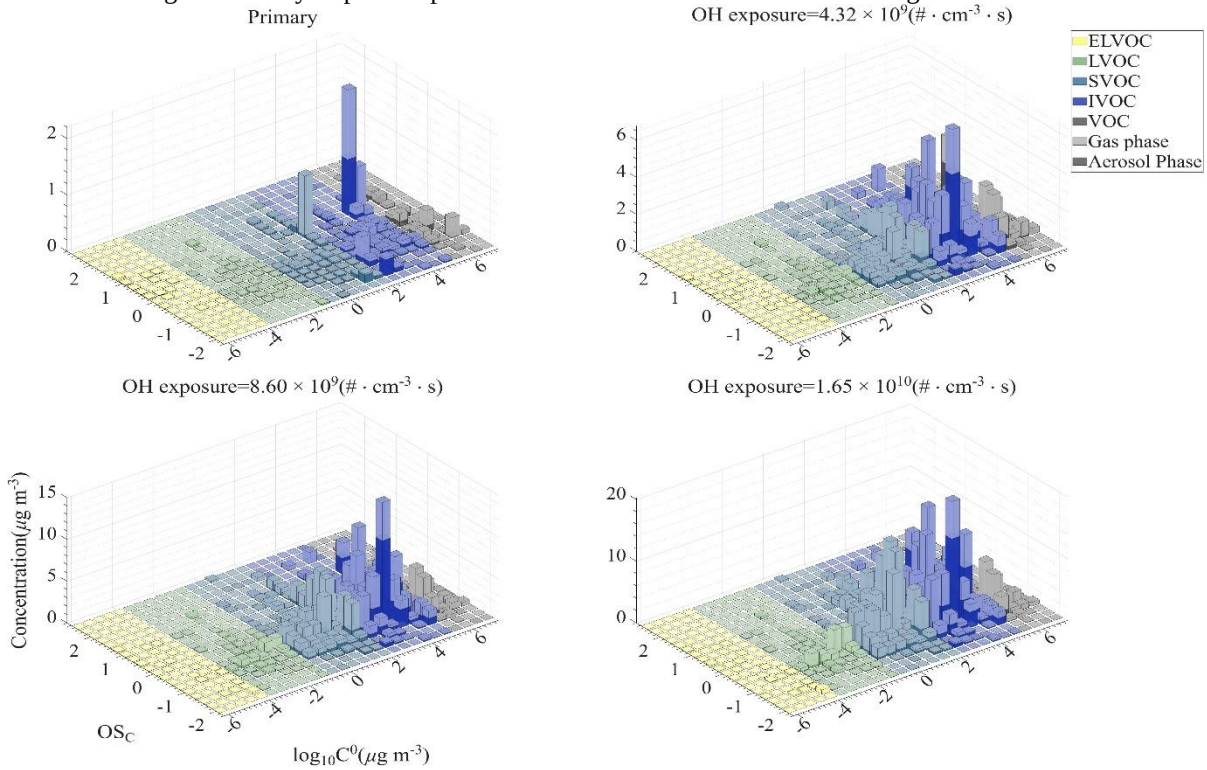

Figure S73 Distribution of gas-phase and aerosol-phase primary and secondary cooking organic species in 2-D VBS space with oxidation. The volatility axis is saturated concentration C^0 determined by 2-D-VBS parameterization recommended by Li et al.(Li et al., 2016).

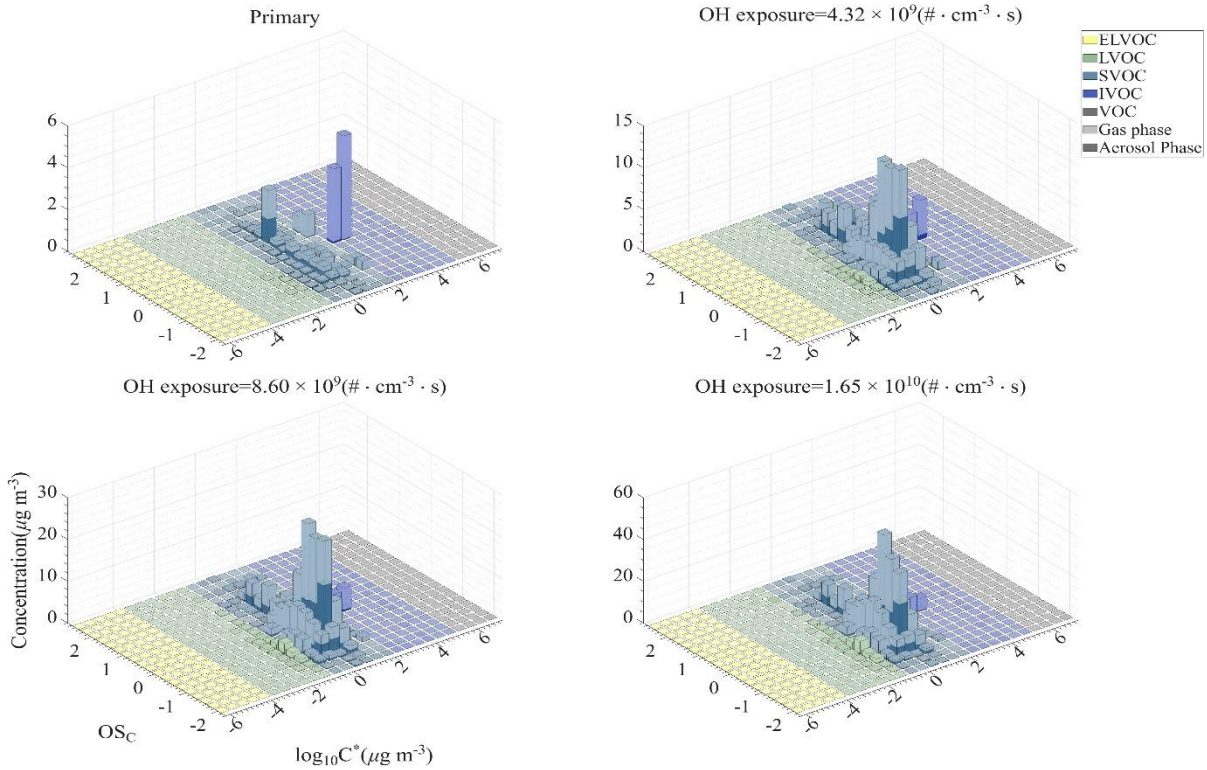

Figure S74 Distribution of gas-phase and aerosol-phase primary and secondary cooking organic species in 2-D VBS space with oxidation. The volatility axis is effective saturated concentration C^* determined from gas-phase and particle-phase concentration measured by FIGAERO-CIMS.

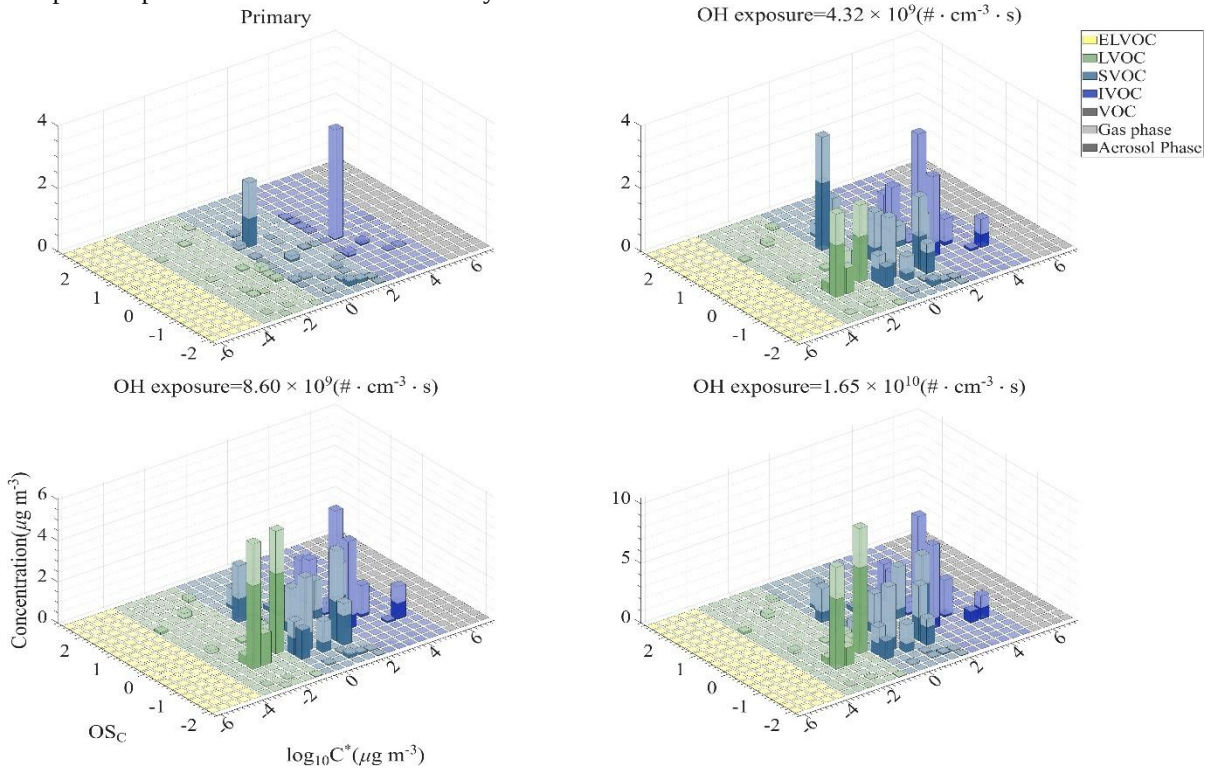

Figure S75 Distribution of gas-phase and aerosol-phase primary and secondary cooking organic species in 2-D VBS space with oxidation. The volatility axis is effective saturated concentration C^* determined from thermograms measured by FIGAERO-CIMS.

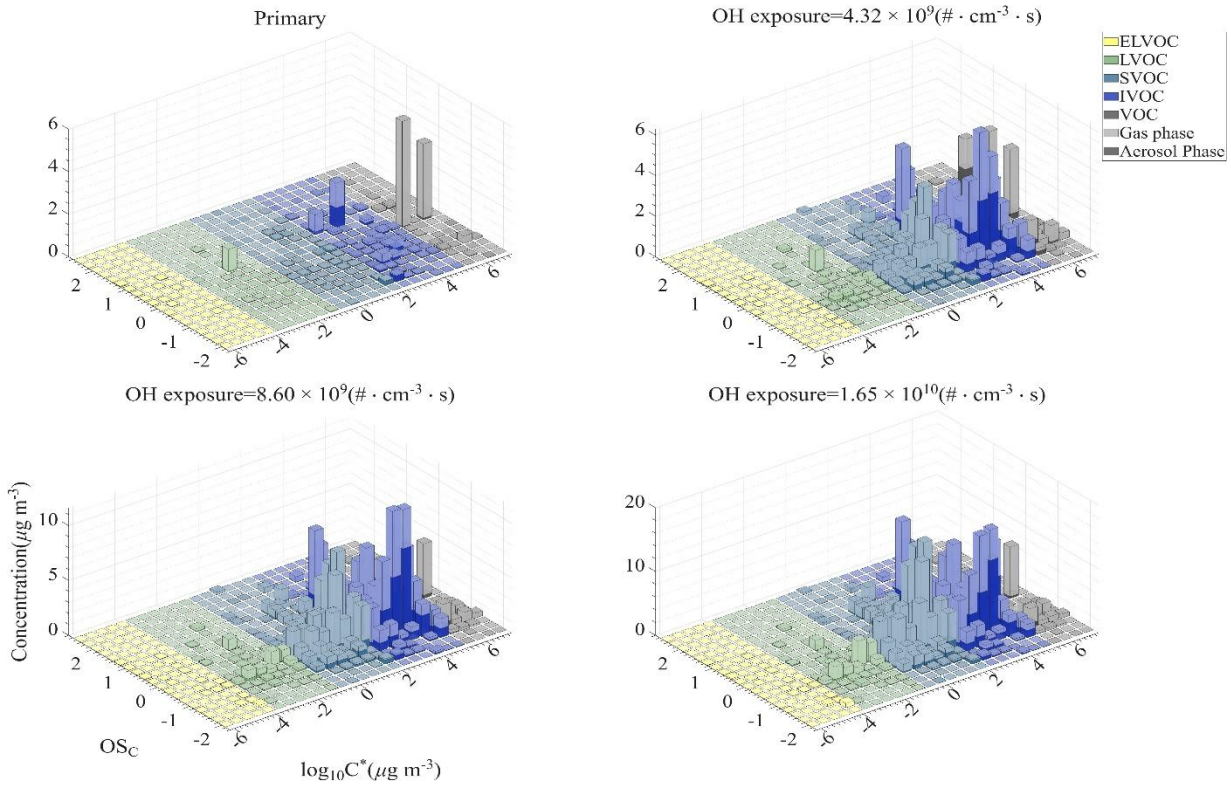

Figure S76 Distribution of gas-phase and aerosol-phase primary and secondary cooking organic species in 2-D VBS space with oxidation. The volatility axis is effective saturated concentration C^* determined from vapor pressure estimation from SIMPOL and activity coefficient from AIOMFAC. Kelvin effect is also considered in C^* calculation.

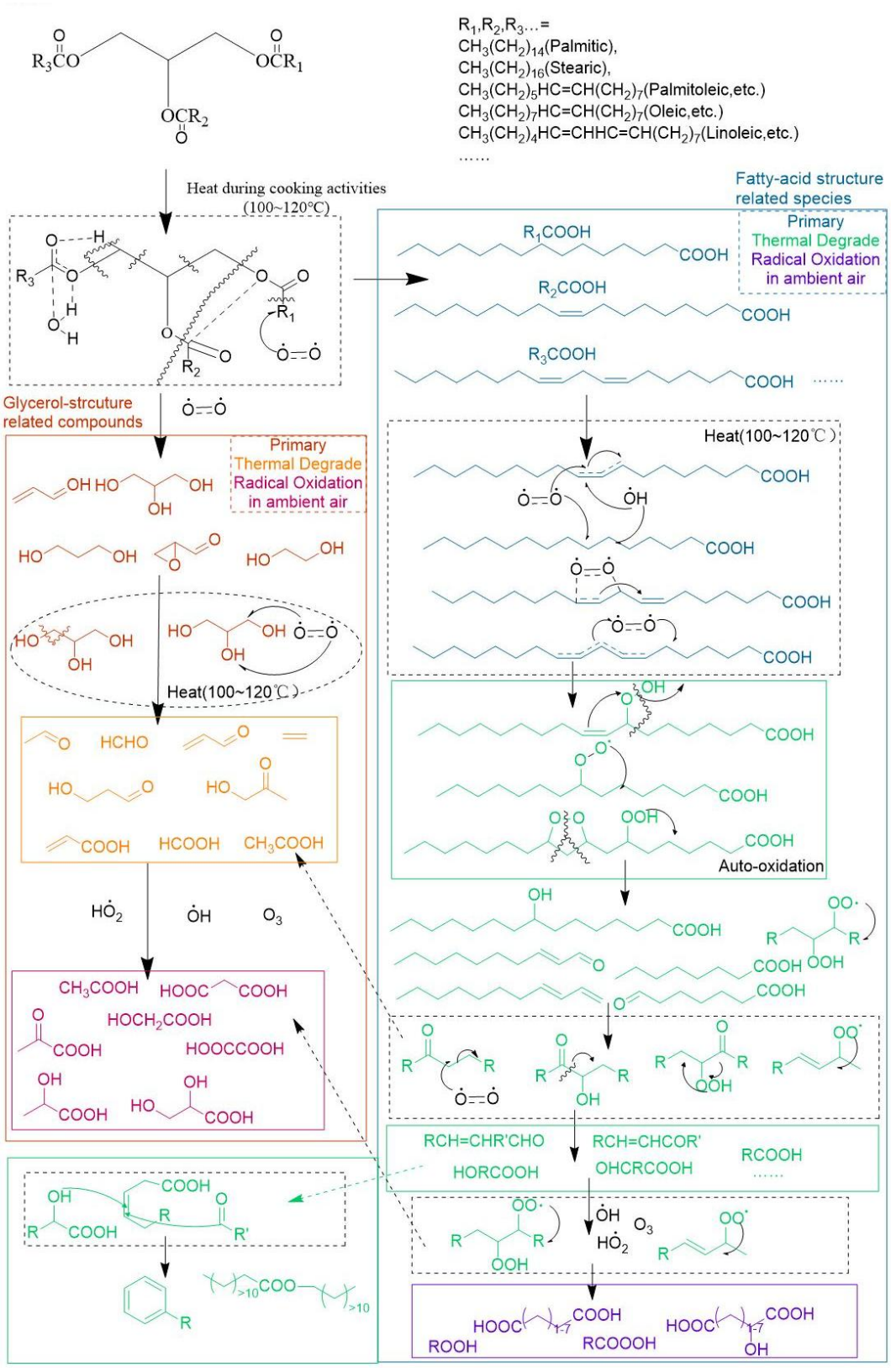

Figure S77 Thermal decomposition and oxidation mechanism of fat during cooking process and in ambient air. Refs.: Thermal decomposition of fat(Kawada et al., 1967; Nawar, 1969; Lóránt, 1977; Patrikios et al., 1994; Nolte et al., 1999; Dobarganes et al., 2000; Martins et al., 2013; Zhou et al., 2022b; Bonetti and Parker, 2019), thermal decomposition and atmospheric oxidation of glycerol-related compounds(Yang et al., 2011; Hemings et al., 2012; Ye et al., 2012; Zhang et al., 2021), thermal decomposition and atmospheric oxidation of long-chain-fatty-acid-related compounds(Nawar, 1969; Peers and Swoboda, 1979; Frankel et al., 1983; Patrikios et al., 1994; Steel et al., 2006; Shin et al., 2012; Martins et al., 2013; Sago et al., 2013; Falade and Oboh, 2015; Aladedunye, 2016; Chen et al., 2017; Bonetti and Parker, 2019; Grebenteuch et al., 2021; Zhou et al., 2022a; Xiao et al., 2023; Yao et al., 2024; Qian et al., 2026) .

References:
Abdullahi, K. L., Delgado-Saborit, J. M., and Harrison, R. M.: Emissions and indoor concentrations of particulate matter and its specific chemical components from cooking: A review, Atmospheric Environment, 71, 260-294, 10.1016/j.atmosenv.2013.01.061, 2013.
Aladedunye, F.: Toxic contaminants of thermo-oxidatively processed edible oils/fats, Lipid Technol., 28, 117-121, 10.1002/lite.201600032, 2016.
Albanie, S.: Euclidean Distance Matrix Trick, 2019.
Angell, C. A.: Relaxation in liquids, polymers and plastic crystals — strong/fragile patterns and problems, J Non-Cryst Solids, 131-133, 13-31, https://doi.org/10.1016/0022-3093(91)90266-9, 1991.
Angell, C. A.: Liquid Fragility and the Glass Transition in Water and Aqueous Solutions, Chemical Reviews, 102, 2627-2650, 10.1021/cr000689q, 2002.
Arthur, D. and Vassilvitskii, S.: k-means++: the advantages of careful seeding, Proceedings of the eighteenth annual ACM-SIAM symposium on Discrete algorithms, New Orleans, Louisiana2007.
Atkinson, R., Baulch, D. L., Cox, R. A., Crowley, J. N., Hampson, R. F., Hynes, R. G., Jenkin, M. E., Rossi, M. J., and Troe, J.: Evaluated kinetic and photochemical data for atmospheric chemistry: Volume I - gas phase reactions of Ox, HOx, NOx and SOx species, Atmos. Chem. Phys., 4, 1461-1738, 10.5194/acp-4-1461-2004, 2004.
Bain, A.: Recent advances in experimental techniques for investigating aerosol surface tension, Aerosol Science and Technology, 10.1080/02786826.2024.2373907, 2024.
Bannan, T. J., Le Breton, M., Priestley, M., Worrall, S. D., Bacak, A., Marsden, N. A., Mehra, A., Hammes, J., Hallquist, M., Alfarra, M. R., Krieger, U. K., Reid, J. P., Jayne, J., Robinson, W., McFiggans, G., Coe, H., Percival, C. J., and Topping, D.: A method for extracting calibrated volatility information from the FIGAERO-HR-ToF-CIMS and its experimental application, Atmospheric Measurement Techniques, 12, 1429-1439, 10.5194/amt-12-1429-2019, 2019.
Becker, S. and Poole, P.: Fractional Stokes-Einstein and Debye-Stokes-Einstein Relations in a Network-Forming Liquid, Physical review letters, 97, 055901, 10.1103/PhysRevLett.97.055901, 2006.
Berkemeier, T., Shiraiwa, M., Pöschl, U., and Koop, T.: Competition between water uptake and ice nucleation by glassy organic aerosol particles, Atmospheric Chemistry and Physics, 14, 12513-12531, 10.5194/acp-14-12513-2014, 2014.
Berry, M. W., Browne, M., Langville, A. N., Pauca, V. P., and Plemmons, R. J.: Algorithms and applications for approximate nonnegative matrix factorization, Computational Statistics & Data Analysis, 52, 155-173, https://doi.org/10.1016/j.csda.2006.11.006, 2007.
Bonetti, R. and Parker, W. O.: Insights into Polymerization of Vegetable Oil: Oligomerization of Oleic Acid, JAOCS J Am Oil Chem Soc, 96, 1181-1184, 10.1002/aocs.12274, 2019.
Bougiatioti, A., Stavroulas, I., Kostenidou, E., Zarmpas, P., Theodosi, C., Kouvarakis, G., Canonaco, F., Prévôt, A. S. H., Nenes, A., Pandis, S. N., and Mihalopoulos, N.: Processing of biomass-burning aerosol in the eastern Mediterranean during summertime, Atmospheric Chemistry and Physics, 14, 4793-4807, 10.5194/acp-14-4793-2014, 2014.
Buchholz, A., Ylisirniö, A., Huang, W., Mohr, C., Canagaratna, M., Worsnop, D. R., Schobesberger, S., and Virtanen, A.: Deconvolution of FIGAERO-CIMS thermal desorption profiles using positive matrix factorisation to identify chemical and physical processes during particle evaporation, Atmospheric Chemistry and Physics, 20, 7693-7716, 10.5194/acp-20-7693-2020, 2020.
Cai, M., Yuan, B., Hu, W., Chenshuo, Y., Huang, S., Yang, S., Chen, W., Peng, Y., Deng, Z., Zhao, J., Chen, D., Sun, J., and Shao, M.: New insight into the formation and aging processes of organic aerosol from positive matrix factorization (PMF) analysis of ambient FIGAERO-CIMS thermograms, Atmospheric Chemistry and Physics, 26, 769-788, 10.5194/acp-26-769-2026, 2026.
Canonaco, F., Crippa, M., Slowik, J. G., Baltensperger, U., and Prévôt, A. S. H.: SoFi, an IGOR-based interface for the efficient use of the generalized multilinear engine (ME-2) for the source apportionment: ME-2 application to aerosol mass spectrometer data, Atmospheric Measurement Techniques, 6, 3649-3661, 10.5194/amt-6-3649-2013, 2013.
Carter, W. P. L., Jiang, J., Wang, Z., and Barsanti, K. C.: The SAPRC atmospheric chemical mechanism generation system (MechGen), Geosci. Model Dev., 18, 8461-8483, 10.5194/gmd-18-8461-2025, 2025.
Caudillo, L., Surdu, M., Lopez, B., Wang, M., Thoma, M., Bräkling, S., Buchholz, A., Simon, M., Wagner, A. C., Müller, T., Granzin, M., Heinritzi, M., Amorim, A., Bell, D. M., Brasseur, Z., Dada,

L., Duplissy, J., Finkenzeller, H., He, X.-C., Lamkaddam, H., Mahfouz, N. G. A., Makhmutov, V., Manninen, H. E., Marie, G., Marten, R., Mauldin, R. L., Mentler, B., Onnela, A., Petäjä, T., Pfeifer, J., Philippov, M., Piedehierro, A. A., Rörup, B., Scholz, W., Shen, J., Stolzenburg, D., Tauber, C., Tian, P., Tomé, A., Umo, N. S., Wang, D. S., Wang, Y., Weber, S. K., Welti, A., Zauner-Wieczorek, M., Baltensperger, U., Flagan, R. C., Hansel, A., Kirkby, J., Kulmala, M., Lehtipalo, K., Worsnop, D. R., Haddad, I. E., Donahue, N. M., Vogel, A. L., Kürten, A., and Curtius, J.: An intercomparison study of four different techniques for measuring the chemical composition of nanoparticles, Atmospheric Chemistry and Physics, 23, 6613-6631, 10.5194/acp-23-6613-2023, 2023.
Chen, H., Cao, P., Li, B., Sun, D., Wang, Y., Li, J., and Liu, Y.: Effect of water content on thermal oxidation of oleic acid investigated by combination of EPR spectroscopy and SPME-GC-MS/MS, Food Chem., 221, 1434-1441, 10.1016/j.foodchem.2016.11.008, 2017.
Chen, W., Hu, W., Tao, Z., Cai, Y., Cai, M., Zhu, M., Ye, Y., Zhou, H., Jiang, H., Li, J., Song, W., Zhou, J., Huang, S., Yuan, B., Shao, M., Feng, Q., Li, Y., Isaacman-VanWertz, G., Stark, H., Day, D. A., Campuzano-Jost, P., Jimenez, J. L., and Wang, X.: Quantitative Characterization of the Volatility Distribution of Organic Aerosols in a Polluted Urban Area: Intercomparison Between Thermodenuder and Molecular Measurements, Journal of Geophysical Research: Atmospheres, 129, 10.1029/2023jd040284, 2024.
Compernolle, S., Ceulemans, K., and Müller, J. F.: EVAPORATION: a new vapour pressure estimation methodfor organic molecules including non-additivity and intramolecular interactions, Atmospheric Chemistry and Physics, 11, 9431-9450, 10.5194/acp-11-9431-2011, 2011.
Davidovits, P., Kolb, C. E., Williams, L. R., Jayne, J. T., and Worsnop, D. R.: Mass Accommodation and Chemical Reactions at Gas−Liquid Interfaces, Chemical Reviews, 106, 1323-1354, 10.1021/cr040366k, 2006.
Davidovits, P., Jayne, J. T., Duan, S. X., Worsnop, D. R., Zahniser, M. S., and Kolb, C. E.: Uptake of gas molecules by liquids: a model, The Journal of Physical Chemistry, 95, 6337-6340, 10.1021/j100169a048, 1991.
DeRieux, W.-S. W., Li, Y., Lin, P., Laskin, J., Laskin, A., Bertram, A. K., Nizkorodov, S. A., and Shiraiwa, M.: Predicting the glass transition temperature and viscosity of secondary organic material using molecular composition, Atmospheric Chemistry and Physics, 18, 6331-6351, 10.5194/acp-18-6331-2018, 2018.
Dobarganes, M. C., Velasco, J., and Dieffenbacher, A.: Determination of polar compounds, polymerized and oxidized triacylglycerols, and diacylglycerols in oils and fats: Results of collaborative studies and the standardized method (Technical report), Pure and Applied Chemistry, 72, 1563-1575, 10.1351/pac200072081563, 2000.
Donahue, N. M., Epstein, S. A., Pandis, S. N., and Robinson, A. L.: A two-dimensional volatility basis set: 1. organic-aerosol mixing thermodynamics, Atmospheric Chemistry and Physics, 11, 3303-3318, 10.5194/acp-11-3303-2011, 2011.
Donahue, N. M., Kroll, J. H., Pandis, S. N., and Robinson, A. L.: A two-dimensional volatility basis set – Part 2: Diagnostics of organic-aerosol evolution, Atmospheric Chemistry and Physics, 12, 615-634, 10.5194/acp-12-615-2012, 2012.
Donahue, N. M., Robinson, A. L., Stanier, C. O., and Pandis, S. N.: Coupled Partitioning, Dilution, and Chemical Aging of Semivolatile Organics, Environmental Science & Technology, 40, 2635-2643, 10.1021/es052297c, 2006.
EPA., U.: Estimation Programs Interface Suite™ for Microsoft® Windows, v 4.11, United States Environmental Protection Agency [code], 2012.
Epstein, S. A., Riipinen, I., and Donahue, N. M.: A Semiempirical Correlation between Enthalpy of Vaporization and Saturation Concentration for Organic Aerosol, Environmental Science & Technology, 44, 743-748, 10.1021/es902497z, 2010.
Evoy, E., MacLean, A. M., Rovelli, G., Li, Y., Tsimpidi, A. P., Karydis, V. A., Kamal, S., Lelieveld, J., Shiraiwa, M., Reid, J. P., and Bertram, A. K.: Predictions of diffusion rates of large organic molecules in secondary organic aerosols using the Stokes-Einstein and fractional Stokes-Einstein relations, Atmospheric Chemistry and Physics, 19, 10073-10085, 10.5194/acp-19-10073-2019, 2019.
Falade, A. O. and Oboh, G.: Thermal oxidation induces lipid peroxidation and changes in the physicochemical properties and β-carotene content of arachis oil, Int. J. Food Sci., 2015, 10.1155/2015/806524, 2015.
Ferreira, J. A., Grassi, M., Gudino, E., and de Oliveira, P.: A new look to non-Fickian diffusion,

Applied Mathematical Modelling, 39, 194-204, 10.1016/j.apm.2014.05.030, 2015.
Fleming, P. J. and Fleming, K. G.: HullRad: Fast Calculations of Folded and Disordered Protein and Nucleic Acid Hydrodynamic Properties, Biophysical Journal, 114, 856-869, 10.1016/j.bpj.2018.01.002, 2018.
Frankel, E. N., Neff, W. E., and Selke, E.: Analysis of autoxidized fats by gas chromatography-mass spectrometry: VIII. Volatile thermal decomposition products of hydroperoxy cyclic peroxides, Lipids, 18, 353-357, 10.1007/BF02537231, 1983.
Fuchs, N. A. and Sutugin, A. G.: HIGH-DISPERSED AEROSOLS, in: Topics in Current Aerosol Research, edited by: Hidy, G. M., and Brock, J. R., Pergamon, 1, https://doi.org/10.1016/B978-0-08-016674-2.50006-6, 1971.
Fuller, E. N., Schettler, P. D., and Giddings, J. C.: NEW METHOD FOR PREDICTION OF BINARY GAS-PHASE DIFFUSION COEFFICIENTS, Industrial & Engineering Chemistry, 58, 18-27, 10.1021/ie50677a007, 1966.
Galeazzo, T. and Shiraiwa, M.: Predicting glass transition temperature and melting point of organic compounds via machine learning and molecular embeddings, Environmental Science: Atmospheres, 2, 362-374, 10.1039/d1ea00090j, 2022.
Gordon, M. and Taylor, J. S.: Ideal copolymers and the second-order transitions of synthetic rubbers. i. non-crystalline copolymers, Journal of Applied Chemistry, 2, 493-500, https://doi.org/10.1002/jctb.5010020901, 1952.
Grebenteuch, S., Kroh, L. W., Drusch, S., and Rohn, S.: Formation of secondary and tertiary volatile compounds resulting from the lipid oxidation of rapeseed oil, Foods, 10, 10.3390/foods10102417, 2021.
Hemings, E. B., Cavallotti, C., Cuoci, A., Faravelli, T., and Ranzi, E.: A Detailed Kinetic Study of Pyrolysis and Oxidation of Glycerol (Propane-1,2,3-triol), Combust Sci Technol, 184, 1164-1178, 10.1080/00102202.2012.664006, 2012.
Hou, S., Liu, W., and Kuwata, M.: Fresh Cooking Organic Aerosol Particles Exist as Liquid in Most Urban Temperature Range, Journal of Geophysical Research: Atmospheres, 130, 10.1029/2025JD043825, 2025.
Ingram, S., Rovelli, G., Song, Y. C., Topping, D., Dutcher, C. S., Liu, S., Nandy, L., Shiraiwa, M., and Reid, J. P.: Accurate Prediction of Organic Aerosol Evaporation Using Kinetic Multilayer Modeling and the Stokes-Einstein Equation, Journal of Physical Chemistry A, 125, 3444-3456, 10.1021/acs.jpca.1c00986, 2021.
Iyer, S., Lopez-Hilfiker, F., Lee, B. H., Thornton, J. A., and Kurten, T.: Modeling the Detection of Organic and Inorganic Compounds Using Iodide-Based Chemical Ionization, J Phys Chem A, 120, 576-587, 10.1021/acs.jpca.5b09837, 2016.
Jensen, A. R., Koss, A. R., Hales, R. B., and de Gouw, J. A.: Measurements of volatile organic compounds in ambient air by gas-chromatography and real-time Vocus PTR-TOF-MS: calibrations, instrument background corrections, and introducing a PTR Data Toolkit, Atmos. Meas. Tech., 16, 5261-5285, 10.5194/amt-16-5261-2023, 2023.
Joo, T., Rivera-Rios, J. C., Takeuchi, M., Alvarado, M. J., and Ng, N. L.: Secondary Organic Aerosol Formation from Reaction of 3-Methylfuran with Nitrate Radicals, ACS Earth and Space Chemistry, 3, 922-934, 10.1021/acsearthspacechem.9b00068, 2019.
Julin, J., Winkler, P. M., Donahue, N. M., Wagner, P. E., and Riipinen, I.: Near-Unity Mass Accommodation Coefficient of Organic Molecules of Varying Structure, Environmental Science & Technology, 48, 12083-12089, 10.1021/es501816h, 2014.
Kawada, T., Krishnamurthy, R. G., Mookherjee, B. D., and Chang, S. S.: Chemical reactions involved in the deep fat frying of foods. II. Identification of acidic volatile decomposition products of corn oil, Journal of the American Oil Chemists' Society, 44, 131-135, 10.1007/BF02558172, 1967.
Knopf, D. A. and Ammann, M.: Technical note: Adsorption and desorption equilibria from statistical thermodynamics and rates from transition state theory, Atmospheric Chemistry and Physics, 21, 15725-15753, 10.5194/acp-21-15725-2021, 2021.
Knopf, D. A., Ammann, M., Berkemeier, T., Pöschl, U., and Shiraiwa, M.: Desorption lifetimes and activation energies influencing gas–surface interactions and multiphase chemical kinetics, Atmospheric Chemistry and Physics, 24, 3445-3528, 10.5194/acp-24-3445-2024, 2024.
Kolb, C. E., Cox, R. A., Abbatt, J. P. D., Ammann, M., Davis, E. J., Donaldson, D. J., Garrett, B. C., George, C., Griffiths, P. T., Hanson, D. R., Kulmala, M., McFiggans, G., Pöschl, U., Riipinen, I.,

Rossi, M. J., Rudich, Y., Wagner, P. E., Winkler, P. M., Worsnop, D. R., and O' Dowd, C. D.: An overview of current issues in the uptake of atmospheric trace gases by aerosols and clouds, Atmos. Chem. Phys., 10, 10561-10605, 10.5194/acp-10-10561-2010, 2010.
Krechmer, J., Lopez-Hilfiker, F., Koss, A., Hutterli, M., Stoermer, C., Deming, B., Kimmel, J., Warneke, C., Holzinger, R., Jayne, J., Worsnop, D., Fuhrer, K., Gonin, M., and de Gouw, J.: Evaluation of a New Reagent-Ion Source and Focusing Ion-Molecule Reactor for Use in Proton-Transfer-Reaction Mass Spectrometry, Anal Chem, 90, 12011-12018, 10.1021/acs.analchem.8b02641, 2018.
Li, X. and Bourg, I. C.: Phase State, Surface Tension, Water Activity, and Accommodation Coefficient of Water-Organic Clusters Near the Critical Size for Atmospheric New Particle Formation, Environ. Sci. Technol., 57, 13092-13103, 10.1021/acs.est.2c09627, 2023.
Li, Y., Pöschl, U., and Shiraiwa, M.: Molecular corridors and parameterizations of volatility in the chemical evolution of organic aerosols, Atmospheric Chemistry and Physics, 16, 3327-3344, 10.5194/acp-16-3327-2016, 2016.
Li, Y., Day, D. A., Stark, H., Jimenez, J. L., and Shiraiwa, M.: Predictions of the glass transition temperature and viscosity of organic aerosols from volatility distributions, Atmos. Chem. Phys., 20, 8103-8122, 10.5194/acp-20-8103-2020, 2020.
Lilek, J. and Zuend, A.: A predictive viscosity model for aqueous electrolytes and mixed organic–inorganic aerosol phases, Atmos. Chem. Phys., 22, 3203-3233, 10.5194/acp-22-3203-2022, 2022.
Liu, W., He, L., Li, Y., Li, P., Chen, S., Chen, J., Liu, Y., and Kuwata, M.: Prolonged Atmospheric Chemical Lifetime of Unsaturated Fatty Acids From Cooking Sources Observed in Beijing During Wintertime, Journal of Geophysical Research: Atmospheres, 130, 10.1029/2025JD044172, 2025a.
Liu, X., Day, D. A., Krechmer, J. E., Brown, W., Peng, Z., Ziemann, P. J., and Jimenez, J. L.: Direct measurements of semi-volatile organic compound dynamics show near-unity mass accommodation coefficients for diverse aerosols, Commun Chem, 2, 10.1038/s42004-019-0200-x, 2019.
Liu, Y., Ge, D., Nie, W., Huang, D. D., Yan, C., Li, Y., Wang, J., Liu, C., Zha, Q., and Wang, J.: A Novel Analytical Framework for Simultaneous Background Correction and Chemical Characterization in Aerosol Molecular Composition Online Mass Spectrometry, Analytical Chemistry, 97, 14473-14482, 10.1021/acs.analchem.5c01723, 2025b.
Lopez-Hilfiker, F. D., Iyer, S., Mohr, C., Lee, B. H., D'Ambro, E. L., Kurtén, T., and Thornton, J. A.: Constraining the sensitivity of iodide adduct chemical ionization mass spectrometry to multifunctional organic molecules using the collision limit and thermodynamic stability of iodide ion adducts, Atmospheric Measurement Techniques, 9, 1505-1512, 10.5194/amt-9-1505-2016, 2016.
Lopez-Hilfiker, F. D., Mohr, C., Ehn, M., Rubach, F., Kleist, E., Wildt, J., Mentel, T. F., Lutz, A., Hallquist, M., Worsnop, D., and Thornton, J. A.: A novel method for online analysis of gas and particle composition: description and evaluation of a Filter Inlet for Gases and AEROsols (FIGAERO), Atmospheric Measurement Techniques, 7, 983-1001, 10.5194/amt-7-983-2014, 2014.
Lórántt, B.: Kinetische Untersuchungen über die thermische Zersetzung von Fetten, Food / Nahrung, 21, 491-496, https://doi.org/10.1002/food.19770210605, 1977.
MacLean, A. M., Smith, N. R., Li, Y., Huang, Y., Hettiyadura, A. P. S., Crescenzo, G. V., Shiraiwa, M., Laskin, A., Nizkorodov, S. A., and Bertram, A. K.: Humidity-Dependent Viscosity of Secondary Organic Aerosol from Ozonolysis of β-Caryophyllene: Measurements, Predictions, and Implications, ACS Earth and Space Chemistry, 5, 305-318, 10.1021/acsearthspacechem.0c00296, 2021.
Marshall, F. H., Miles, R. E. H., Song, Y. C., Ohm, P. B., Power, R. M., Reid, J. P., and Dutcher, C. S.: Diffusion and reactivity in ultraviscous aerosol and the correlation with particle viscosity, Chem Sci, 7, 1298-1308, 10.1039/c5sc03223g, 2016.
Martins, G. B. C., Mello, V. M., and Suarez, P. A. Z.: Thermal processes in fats and oils, Rev. Virtual Quim., 5, 16-25, 10.5935/1984-6835.20130003, 2013.
Masoud, C. G., Li, Y., Wang, D. S., Katz, E. F., DeCarlo, P. F., Farmer, D. K., Vance, M. E., Shiraiwa, M., and Hildebrandt Ruiz, L.: Molecular composition and gas-particle partitioning of indoor cooking aerosol: Insights from a FIGAERO-CIMS and kinetic aerosol modeling, Aerosol Science and Technology, 56, 1156-1173, 10.1080/02786826.2022.2133593, 2022.
May, A. A., Saleh, R., Hennigan, C. J., Donahue, N. M., and Robinson, A. L.: Volatility of organic molecular markers used for source apportionment analysis: measurements and implications for atmospheric lifetime, Environ Sci Technol, 46, 12435-12444, 10.1021/es302276t, 2012.
McDonald, J. D., Zielinska, B., Fujita, E. M., Sagebiel, J. C., Chow, J. C., and Watson, J. G.:

Emissions from charbroiling and grilling of chicken and beef, J Air Waste Manag Assoc, 53, 185-194, 10.1080/10473289.2003.10466141, 2003.
Miyamoto, S. and Shimono, K.: Molecular Modeling to Estimate the Diffusion Coefficients of Drugs and Other Small Molecules, Molecules, 25, 10.3390/molecules25225340, 2020.
Mutneja, A. and Karmakar, S.: Length-scale dependence of Stokes-Einstein breakdown in active glass-forming liquids, Physical Review E, 111, 10.1103/PhysRevE.111.035409, 2025.
Nagayama, G. and Tsuruta, T.: A general expression for the condensation coefficient based on transition state theory and molecular dynamics simulation, The Journal of Chemical Physics, 118, 1392-1399, 10.1063/1.1528192, 2003.
Nah, T., Xu, L., Osborne-Benthaus, K. A., White, S. M., France, S., and Ng, N. L.: Mixing order of sulfate aerosols and isoprene epoxydiols affects secondary organic aerosol formation in chamber experiments, Atmospheric Environment, 217, 116953, https://doi.org/10.1016/j.atmosenv.2019.116953, 2019.
Nawar, W. W.: Thermal degradation of lipids, J Agr Food Chem, 17, 18-21, 10.1021/jf60161a012, 1969.
Nguyen, K., Schervish, M., Lakey, P. S. J., Smith, J. N., and Shiraiwa, M.: Impact of particle phase state on the competition between condensation and coagulation, Environmental Science: Atmospheres, 6, 152-165, 10.1039/d5ea00069f, 2026.
Nolte, C. G., Schauer, J. J., Cass, G. R., and Simoneit, B. R. T.: Highly Polar Organic Compounds Present in Meat Smoke, Environmental Science & Technology, 33, 3313-3316, 10.1021/es990122v, 1999.
Odum, J. R., Yu, J., and Kamens, R. M.: Modeling the Mass Transfer of Semivolatile Organics in Combustion Aerosols, Environmental Science & Technology, 28, 2278-2285, 10.1021/es00062a011, 1994.
Odum, J. R., Hoffmann, T., Bowman, F., Collins, D., Flagan, R. C., and Seinfeld, J. H.: Gas/Particle Partitioning and Secondary Organic Aerosol Yields, Environmental Science & Technology, 30, 2580-2585, 10.1021/es950943+, 1996.
Ono, R., Nakagawa, Y., Tokumitsu, Y., Matsumoto, H., and Oda, T.: Effect of humidity on the production of ozone and other radicals by low-pressure mercury lamps, Journal of Photochemistry and Photobiology A: Chemistry, 274, 13-19, 10.1016/j.jphotochem.2013.09.012, 2014.
Paatero, P.: The Multilinear Engine: A Table-Driven, Least Squares Program for Solving Multilinear Problems, including the n-Way Parallel Factor Analysis Model, Journal of Computational and Graphical Statistics, 8, 854-888, 10.2307/1390831, 1999.
Pankow, J. F.: An absorption model of gas/particle partitioning of organic compounds in the atmosphere, Atmospheric Environment, 28, 185-188, https://doi.org/10.1016/1352-2310(94)90093-0, 1994.
Pankow, J. F. and Asher, W. E.: SIMPOL.1: a simple group contribution method for predicting vapor pressures and enthalpies of vaporization of multifunctional organic compounds, Atmos. Chem. Phys., 8, 2773-2796, 10.5194/acp-8-2773-2008, 2008.
Pastore, R., Kikutsuji, T., Rusciano, F., Matubayasi, N., Kim, K., and Greco, F.: Breakdown of the Stokes-Einstein relation in supercooled liquids: A cage-jump perspective, Journal of Chemical Physics, 155, 10.1063/5.0059622, 2021.
Patrikios, I. S., Britton, O., Bing, D. K., and Russell, C. S.: Heating unsaturated fatty acids in air produces hemagglutinins, Biochim. Biophys. Acta Lipids Lipid Metab., 1212, 225-234, 10.1016/0005-2760(94)90257-7, 1994.
Peers, K. E. and Swoboda, P. A. T.: Octanoate: An assay for oxidative deterioration in oils and fats, J. Sci. Food Agric., 30, 876-880, 10.1002/jsfa.2740300908, 1979.
Peng, Z. and Jimenez, J. L.: Radical chemistry in oxidation flow reactors for atmospheric chemistry research, Chem Soc Rev, 49, 2570-2616, 10.1039/c9cs00766k, 2020.
Peng, Z., Day, D. A., Ortega, A. M., Palm, B. B., Hu, W., Stark, H., Li, R., Tsigaridis, K., Brune, W. H., and Jimenez, J. L.: Non-OH chemistry in oxidation flow reactors for the study of atmospheric chemistry systematically examined by modeling, Atmos. Chem. Phys., 16, 4283-4305, 10.5194/acp-16-4283-2016, 2016.
Prager, S., Haynes, M. S., and Moghaddam, M.: Wireless Subnanosecond RF Synchronization for Distributed Ultrawideband Software-Defined Radar Networks, IEEE Transactions on Microwave Theory and Techniques, 68, 4787-4804, 10.1109/TMTT.2020.3014876, 2020.

Preston, T. C.: Non-Fickian diffusion in viscous aerosol particles, Canadian Journal of Chemistry, 100, 168-174, 10.1139/cjc-2021-0187, 2022.
Price, D. J., Kacarab, M., Cocker, D. R., Purvis-Roberts, K. L., and Silva, P. J.: Effects of temperature on the formation of secondary organic aerosol from amine precursors, Aerosol Science and Technology, 50, 1216-1226, 10.1080/02786826.2016.1236182, 2016.
Pun, B. K., Griffin, R. J., Seigneur, C., and Seinfeld, J. H.: Secondary organic aerosol 2. Thermodynamic model for gas/particle partitioning of molecular constituents, Journal of Geophysical Research: Atmospheres, 107, AAC 4-1-AAC 4-15, 10.1029/2001jd000542, 2002.
Qian, B., Zhu, X., Su, C., Li, H., Wu, Q., Liu, C., Pan, Y., and Han, B.: Mechanism of Water-Enhanced Volatile Aldehyde Release in Oil Fumes from Thermal Oxidation of Oleic Acid: Insights from Synchrotron Radiation Photoionization and Gas Chromatography–Mass Spectrometry, Molecules, 31, 10.3390/molecules31040594, 2026.
Reid, R. C., Prausnitz, J. M., and Poling, B. E.: The properties of gases and liquids, None, McGraw Hill Book Co.,New York, NY; None, United States1987.
Ren, S., Yao, L., Wang, Y., Yang, G., Liu, Y., Li, Y., Lu, Y., Wang, L., and Wang, L.: Volatility parameterization of ambient organic aerosols at a rural site of the North China Plain, Atmos. Chem. Phys., 22, 9283-9297, 10.5194/acp-22-9283-2022, 2022.
Reyes-Villegas, E., Bannan, T., Le Breton, M., Mehra, A., Priestley, M., Percival, C., Coe, H., and Allan, J. D.: Online Chemical Characterization of Food-Cooking Organic Aerosols: Implications for Source Apportionment, Environ Sci Technol, 52, 5308-5318, 10.1021/acs.est.7b06278, 2018.
Rogge, W. F., Hildemann, L. M., Mazurek, M. A., Cass, G. R., and Simoneit, B. R. T.: Sources of fine organic aerosol. 1. Charbroilers and meat cooking operations, Environmental Science & Technology, 25, 1112-1125, 10.1021/es00018a015, 1991.
Sago, T., Ishii, H., Hagihara, H., Takada, N., and Suda, H.: Analysis of chemiluminescence spectra in oxidative degradation of oleic acid, Chemical Physics Letters, 565, 138-142, 10.1016/j.cplett.2013.02.035, 2013.
Saleh, R., Donahue, N. M., and Robinson, A. L.: Time scales for gas-particle partitioning equilibration of secondary organic aerosol formed from alpha-pinene ozonolysis, Environ Sci Technol, 47, 5588-5594, 10.1021/es400078d, 2013.
Schmedding, R., Franssen, M., and Zuend, A.: A Machine Learning Approach for Predicting the Pure-Component Surface Tension of Atmospherically Relevant Organic Compounds, ACS ES&T air, 2, 808-823, 10.1021/acsestair.4c00291, 2025.
Seinfeld, J. H., Pandis, S.N.: Atmospheric Chemistry and Physics - From Air Pollution to Climate Change 3rd, John Wiley & Sons, INC., Hoboken, New Jersey2016.
Sekimoto, K., Li, S.-M., Yuan, B., Koss, A., Coggon, M., Warneke, C., and de Gouw, J.: Calculation of the sensitivity of proton-transfer-reaction mass spectrometry (PTR-MS) for organic trace gases using molecular properties, International Journal of Mass Spectrometry, 421, 71-94, https://doi.org/10.1016/j.ijms.2017.04.006, 2017.
Shin, H. Y., Ryu, J. H., Park, S. Y., and Bae, S. Y.: Thermal stability of fatty acids in subcritical water, J Anal Appl Pyrolysis, 98, 250-253, 10.1016/j.jaap.2012.08.003, 2012.
Shiraiwa, M. and Pöschl, U.: Mass accommodation and gas–particle partitioning in secondary organic aerosols: dependence on diffusivity, volatility, particle-phase reactions, and penetration depth, Atmospheric Chemistry and Physics, 21, 1565-1580, 10.5194/acp-21-1565-2021, 2021.
Shiraiwa, M., Ammann, M., Koop, T., and Pöschl, U.: Gas uptake and chemical aging of semisolid organic aerosol particles, Proceedings of the National Academy of Sciences, 108, 11003, 10.1073/pnas.1103045108, 2011.
Shiraiwa, M., Li, Y., Tsimpidi, A. P., Karydis, V. A., Berkemeier, T., Pandis, S. N., Lelieveld, J., Koop, T., and Poschl, U.: Global distribution of particle phase state in atmospheric secondary organic aerosols, Nat Commun, 8, 15002, 10.1038/ncomms15002, 2017.
Sitzmann, M., Zakharov, A. V., Pàmies, L. G., and Nicklaus, M. C.: NCI/CADD chemical structure Web services, Abstracts of Papers of the American Chemical Society, 245, 2013.
Song, K., Guo, S., Gong, Y. Z., Lv, D. Q., Zhang, Y., Wan, Z. C., Li, T. Y., Zhu, W. F., Wang, H., Yu, Y., Tan, R., Shen, R. Z., Lu, S. H., Li, S. D., Chen, Y. F., and Hu, M.: Impact of cooking style and oil on semi-volatile and intermediate volatility organic compound emissions from Chinese domestic cooking, Atmospheric Chemistry and Physics, 22, 9827-9841, 10.5194/acp-22-9827-2022, 2022.

Stark, H., Yatavelli, R. L. N., Thompson, S. L., Kang, H., Krechmer, J. E., Kimmel, J. R., Palm, B. B., Hu, W., Hayes, P. L., Day, D. A., Campuzano-Jost, P., Canagaratna, M. R., Jayne, J. T., Worsnop, D. R., and Jimenez, J. L.: Impact of Thermal Decomposition on Thermal Desorption Instruments: Advantage of Thermogram Analysis for Quantifying Volatility Distributions of Organic Species, Environ Sci Technol, 51, 8491-8500, 10.1021/acs.est.7b00160, 2017.
Steel, C. J., Dobarganes, M. C., and Barrera-Arellano, D.: Formation of polymerization compounds during thermal oxidation of cottonseed oil, partially hydrogenated cottonseed oil and their blends, Grasas Aceites, 57, 284-291, 10.3989/gya.2006.v57.i3.50, 2006.
Sun, Y., Luo, H., Li, Y., Zhou, W., Xu, W., Fu, P., and Zhao, D.: Atmospheric organic aerosols: online molecular characterization and environmental impacts, npj Climate and Atmospheric Science, 8, 10.1038/s41612-025-01199-2, 2025.
Takhar, M., Li, Y., and Chan, A. W. H.: Characterization of secondary organic aerosol from heated-cooking-oil emissions: evolution in composition and volatility, Atmospheric Chemistry and Physics, 21, 5137-5149, 10.5194/acp-21-5137-2021, 2021.
Takhar, M., Stroud, C. A., and Chan, A. W. H.: Volatility Distribution and Evaporation Rates of Organic Aerosol from Cooking Oils and their Evolution upon Heterogeneous Oxidation, ACS Earth and Space Chemistry, 3, 1717-1728, 10.1021/acsearthspacechem.9b00110, 2019.
Tang, M. J., Shiraiwa, M., Pöschl, U., Cox, R. A., and Kalberer, M.: Compilation and evaluation of gas phase diffusion coefficients of reactive trace gases in the atmosphere: Volume 2. Diffusivities of organic compounds, pressure-normalised mean free paths, and average Knudsen numbers for gas uptake calculations, Atmospheric Chemistry and Physics, 15, 5585-5598, 10.5194/acp-15-5585-2015, 2015.
Tikkanen, I. P., Buchholz, A., Ylisirniö, A., Schobesberger, S., Virtanen, A., and Yli-Juuti, T.: Comparing secondary organic aerosol (SOA) volatility distributions derived from isothermal SOA particle evaporation data and FIGAERO-CIMS measurements, Atmospheric Chemistry and Physics, 20, 10441-10458, 10.5194/acp-20-10441-2020, 2020.
Vaden, T. D., Imre, D., Beranek, J., Shrivastava, M., and Zelenyuk, A.: Evaporation kinetics and phase of laboratory and ambient secondary organic aerosol, Proc Natl Acad Sci U S A, 108, 2190-2195, 10.1073/pnas.1013391108, 2011.
Wang, M., Chen, D., Xiao, M., Ye, Q., Stolzenburg, D., Hofbauer, V., Ye, P., Vogel, A. L., Mauldin, R. L., 3rd, Amorim, A., Baccarini, A., Baumgartner, B., Brilke, S., Dada, L., Dias, A., Duplissy, J., Finkenzeller, H., Garmash, O., He, X. C., Hoyle, C. R., Kim, C., Kvashnin, A., Lehtipalo, K., Fischer, L., Molteni, U., Petaja, T., Pospisilova, V., Quelever, L. L. J., Rissanen, M., Simon, M., Tauber, C., Tome, A., Wagner, A. C., Weitz, L., Volkamer, R., Winkler, P. M., Kirkby, J., Worsnop, D. R., Kulmala, M., Baltensperger, U., Dommen, J., El-Haddad, I., and Donahue, N. M.: Photo-oxidation of Aromatic Hydrocarbons Produces Low-Volatility Organic Compounds, Environ Sci Technol, 54, 7911-7921, 10.1021/acs.est.0c02100, 2020.
Wang, X., Chen, N., Zhu, B., and Yu, H.: Influencing factors of the gas-particle distribution of oxygenated organic molecules in the urban atmosphere and deviation from equilibrium partitioning: A random forest model study, Atmospheric Chemistry and Physics, 25, 9601-9615, 10.5194/acp-25-9601-2025, 2025.
Xiao, L., Wang, S., Wang, Y., Wang, B., Ji, C., Lin, X., Liang, H., Zhang, S., Xu, X., and Dong, L.: Density functional theory studies on the oleic acid thermal oxidation into volatile compounds, Food Chem. X, 19, 10.1016/j.fochx.2023.100737, 2023.
Xu, N., Hu, M., Li, X., Song, K., Qiu, Y., Sun, H. X., Wang, Y., Zeng, L., Li, M., Wang, H., Hu, S., Zong, T., Bai, Y., Zhang, Z., Li, S., Shuai, S., Chen, Y., and Guo, S.: Resolving Ultraviolet–Visible Spectra for Complex Dissolved Mixtures of Multitudinous Organic Matters in Aerosols, Analytical Chemistry, 96, 1834-1842, 10.1021/acs.analchem.3c02700, 2024.
Yang, X., Kiefer, J. H., and Tranter, R. S.: Thermal dissociation of ethylene glycol vinyl ether, Physical Chemistry Chemical Physics, 13, 21288-21300, 10.1039/C1CP21073D, 2011.
Yao, Y., Qiang, Z., Zhang, M., Lin, J., and Li, C.: Thermal oxidation mechanism of palmitic aicd, Food Research International, 186, 114372, https://doi.org/10.1016/j.foodres.2024.114372, 2024.
Ye, L., Zhang, F., Zhang, L., and Qi, F.: Theoretical studies on the unimolecular decomposition of propanediols and glycerol, Journal of Physical Chemistry A, 116, 4457-4465, 10.1021/jp301424k, 2012.
Ye, Q., Wang, M., Hofbauer, V., Stolzenburg, D., Chen, D., Schervish, M., Vogel, A., Mauldin, R. L.,

Baalbaki, R., Brilke, S., Dada, L., Dias, A., Duplissy, J., El Haddad, I., Finkenzeller, H., Fischer, L., He, X., Kim, C., Kürten, A., Lamkaddam, H., Lee, C. P., Lehtipalo, K., Leiminger, M., Manninen, H. E., Marten, R., Mentler, B., Partoll, E., Petäjä, T., Rissanen, M., Schobesberger, S., Schuchmann, S., Simon, M., Tham, Y. J., Vazquez-Pufleau, M., Wagner, A. C., Wang, Y., Wu, Y., Xiao, M., Baltensperger, U., Curtius, J., Flagan, R., Kirkby, J., Kulmala, M., Volkamer, R., Winkler, P. M., Worsnop, D., and Donahue, N. M.: Molecular Composition and Volatility of Nucleated Particles from α-Pinene Oxidation between −50 °C and +25 °C, Environmental Science & Technology, 53, 12357-12365, 10.1021/acs.est.9b03265, 2019.
Ylisirniö, A., Barreira, L. M. F., Pullinen, I., Buchholz, A., Jayne, J., Krechmer, J. E., Worsnop, D. R., Virtanen, A., and Schobesberger, S.: On the calibration of FIGAERO-ToF-CIMS: importance and impact of calibrant delivery for the particle-phase calibration, Atmospheric Measurement Techniques, 14, 355-367, 10.5194/amt-14-355-2021, 2021.
Ylisirniö, A., Hyttinen, N., Li, Z., Alton, M. W., Nissinen, A., Pullinen, I., Miettinen, P., Yli-Juuti, T., and Schobesberger, S.: The saturation vapor pressures of higher-order polyethylene glycols and achieving a wide calibration range for volatility measurements by FIGAERO-CIMS, Atmospheric Measurement Techniques, 18, 6449-6464, 10.5194/amt-18-6449-2025, 2025.
Yu, Y., Guo, S., Wang, H., Shen, R., Zhu, W., Tan, R., Song, K., Zhang, Z., Li, S., Chen, Y., and Hu, M.: Importance of Semivolatile/Intermediate-Volatility Organic Compounds to Secondary Organic Aerosol Formation from Chinese Domestic Cooking Emissions, Environmental Science & Technology Letters, 9, 507-512, 10.1021/acs.estlett.2c00207, 2022.
Zhang, D., Cao, Y., Zhang, P., Liang, J., Xue, K., Xia, Y., and Qi, Z.: Investigation of the thermal decomposition mechanism of glycerol: The combination of a theoretical study based on the Minnesota functional and experimental support, Physical Chemistry Chemical Physics, 23, 20466-20477, 10.1039/d1cp01526e, 2021.
Zhang, X., Li, C., Xue, S., Yang, X., Wang, Y., Li, Y., Cai, R., Yao, L., and Wang, L.: Volatility Parametrization of Atmospheric Organic Compounds Based on Molecular Formula, Am. Chem. Soc. Environ. Sci. Technol. Air., 3, 291-301, 10.1021/acsestair.5c00167, 2026.
Zhang, Z., Zhu, W., Hu, M., Wang, H., Chen, Z., Shen, R., Yu, Y., Tan, R., and Guo, S.: Secondary Organic Aerosol from Typical Chinese Domestic Cooking Emissions, Environmental Science & Technology Letters, 8, 24-31, 10.1021/acs.estlett.0c00754, 2020.
Zhou, Z., Lakey, P. S. J., von Domaros, M., Wise, N., Tobias, D. J., Shiraiwa, M., and Abbatt, J. P. D.: Multiphase Ozonolysis of Oleic Acid-Based Lipids: Quantitation of Major Products and Kinetic Multilayer Modeling, Environ. Sci. Technol., 56, 7716-7728, 10.1021/acs.est.2c01163, 2022a.
Zhou, Z., Li, Y. L., Zhao, F., Xin, R., Huang, X. H., Zhang, Y. Y., Zhou, D., and Qin, L.: Unraveling the Thermal Oxidation Products and Peroxidation Mechanisms of Different Chemical Structures of Lipids: An Example of Molecules Containing Oleic Acid, J Agr Food Chem, 70, 16410-16423, 10.1021/acs.jafc.2c06221, 2022b.
Zhu, W., Guo, S., Zhang, Z., Wang, H., Yu, Y., Chen, Z., Shen, R., Tan, R., Song, K., Liu, K., Tang, R., Liu, Y., Lou, S., Li, Y., Zhang, W., Zhang, Z., Shuai, S., Xu, H., Li, S., Chen, Y., Hu, M., Canonaco, F., and Prévôt, A. S. H.: Mass spectral characterization of secondary organic aerosol from urban cooking and vehicular sources, Atmospheric Chemistry and Physics, 21, 15065-15079, 10.5194/acp-21-15065-2021, 2021.
Zuend, A. and Seinfeld, J. H.: Modeling the gas-particle partitioning of secondary organic aerosol: the importance of liquid-liquid phase separation, Atmospheric Chemistry and Physics, 12, 3857-3882, 10.5194/acp-12-3857-2012, 2012.
Zwanzig, R. and Harrison, A. K.: Modifications of the Stokes–Einstein formula, The Journal of Chemical Physics, 83, 5861-5862, 10.1063/1.449616, 1985.